Department of Physics and Astronomy

University of Heidelberg

Master thesis

in Physics

submitted by

Jonathan Brandt

born in Hanau

2020

Studies of $B^0 \to K^{*0}\gamma$ transitions reconstructed in the $K^{*0}e^+e^-$ final state

This Master thesis has been carried out by Jonathan Brandt

at the

Physikalisches Institut

under the supervision of

Prof. Dr. Stephanie Hansmann-Menzemer

Untersuchung von $B^0 \to K^{*0}\gamma$ Übergängen im $K^{*0}e^+e^-$ Endzustand

Diese Arbeit präsentiert eine Messung des Verzweigungsverhältnisses und eine Analyse der Winkelverteilungen des $B^0 \to K^{*0}e^+e^-$ Zerfalls. Die Messungen basieren auf einem Datenset von pp Kollisionen, das mit dem LHCb Experiment aufgenommen wurde und einer integrierten Luminosität von 9.0 fb^{-1} entspricht. Die Analyse beschränkt sich auf den Bereich mit sehr niedrigem invarianten Massenquadrat des Elektronenpaares (q^2) zwischen 0.0008 und 0.257 GeV^2, in dem der Zerfall hauptsächlich durch den $B^0 \to K^{*0}\gamma$ Übergang mit einem virtuellen Photon stattfindet. Das Verzweigunsverhältnis in diesem Bereich wird zu $\mathcal{B}(B^0 \to K^{*0}e^+e^-) = (2.06 \pm 0.10 \pm 0.08) \times 10^{-7}$ bestimmt, wobei die erste Unsicherheit statistischer Natur ist und die zweite sich aus Unsicherheiten der externen Eingabewerte ergibt. Die Analyse der Winkelverteilung ergibt $F_{\rm L} = (4.4 \pm 2.6 \pm 1.4)\%$, wo die erste Unsicherheit statistisch und die zweite systematischer Natur ist, sowie $A_T^{Re} = -0.064 \pm 0.077 \pm 0.015$, $A_T^{(2)} = 0.106 \pm 0.103 \pm 0.017$ und $A_T^{Im} = 0.015 \pm 0.102 \pm 0.012$ für die restlichen Parameter der Winkelverteilung. Die letzten beiden sind sensitiv auf die Polarisation der virtuellen Photonen. Alle gemessenen Werte sind mit Vorhersagen des Standard Models vereinbar und stellen die stärksten Einschränkungen für die $b \to s\gamma$ Photon Polarisation dar.

Studies of $B^0 \to K^{*0}\gamma$ transitions reconstructed in the $K^{*0}e^+e^-$ final state

This thesis presents a branching fraction measurement and angular analysis of the $B^0 \to K^{*0}e^+e^-$ decay. The data sample corresponds to an integrated luminosity of 9.0 fb^{-1} of pp collisions collected with the LHCb experiment. The analysis is conducted in the very low dielectron mass squared (q^2) interval between 0.0008 and 0.257 GeV^2, where the decay is dominated by the $B^0 \to K^{*0}\gamma$ transition with a virtual photon. The branching fraction is measured to be $\mathcal{B}(B^0 \to K^{*0}e^+e^-) = (2.06 \pm 0.10 \pm 0.08) \times 10^{-7}$, where the first uncertainty is statistical and the second due to the uncertainty of external inputs. The angular observables are measured to be $F_{\rm L} = (4.4 \pm 2.6 \pm 1.4)\%$ and $A_T^{Re} = -0.064 \pm 0.077 \pm 0.015$, where the first uncertainty is statistical and the second systematic, as well as $A_T^{(2)} = 0.106 \pm 0.103 \pm 0.017$ and $A_T^{Im} = 0.015 \pm 0.102 \pm 0.012$. These last two observables are sensitive to the virtual photon polarization. The results are consistent with Standard Model predictions and provide the world's best constraint on the $b \to s\gamma$ photon polarization.

Contents

1 Introduction **3**

2 Theory **5**
2.1 Standard Model of particle physics 5
2.2 The weak interaction of quarks 6
2.3 Beyond the Standard Model 7
2.4 The $b \to s\gamma$ transition 8
2.5 Measuring the photon polarization with $B^0 \to K^{*0}e^+e^-$ decays . 10
2.6 Differential decay width of the $B^0 \to K^{*0}e^+e^-$ decay 12

3 The LHCb experiment at the LHC **17**
3.1 The Large Hadron Collider 17
3.2 The LHCb experiment 17
3.2.1 Tracking and vertex reconstruction 19
3.2.2 Particle identification and energy measurement 21
3.2.3 Trigger system 24
3.2.4 LHCb simulation 25

4 Analysis overview **27**
4.1 Data and simulation samples 27
4.2 Choice of q^2 region 27
4.3 Control channels 29
4.4 Maximum likelihood fits 30
4.5 Analysis strategy 31

5 Data selection **33**
5.1 Trigger and pre-selection 33
5.2 Data and simulation differences 34
5.3 Background contributions 35
5.3.1 Semi-leptonic background 36
5.3.2 $B^0 \to K^{*0}\gamma(\to e^+e^-)$ background 36
5.3.3 $B^0 \to K^{*0}\pi^0/\eta$ backgrounds 38
5.3.4 Partially reconstructed background 39
5.3.5 Combinatorial background 40

5.3.6 Other background contributions 41
5.3.7 Selection of $B^0 \to K^{*0} J/\psi\,(\to e^+e^-)$ candidates 43
5.4 Selection summary and efficiencies 43

6 Mass fits **49**
6.1 Mass fit in the $B^0 \to K^{*0} J/\psi\,(\to e^+e^-)$ reference channel 49
6.1.1 Mass shapes from simulation 50
6.1.2 Mass fit to data 52
6.2 Mass fit in the $B^0 \to K^{*0} e^+e^-$ signal channel 55
6.2.1 Mass shapes from simulation 55
6.2.2 Mass fit to $B^0 \to K^{*0} e^+e^-$ data 64
6.3 Branching ratio measurement 70
6.3.1 Modifications to the mass fit 70

7 Angular fits **73**
7.1 Angular fit strategy 73
7.2 Angular acceptance 73
7.2.1 Acceptance fit 74
7.3 Angular modeling of backgrounds 79
7.3.1 Angular modeling of partially reconstructed background 79
7.3.2 Angular modeling of $B^0 \to K^{*0}\gamma(\to e^+e^-)$ background . 80
7.3.3 Angular modeling of $B^0 \to K^{*0}\pi^0(\to \gamma e^+e^-)$ and $B^0 \to K^{*0}\eta(\to \gamma e^+e^-)$ backgrounds 82
7.3.4 Angular modeling of combinatorial background 84

8 Fit validation **87**
8.1 Angular fit to $B^0 \to K^{*0} e^+e^-$ simulation 87
8.2 Angular Fit to $B^0 \to K^{*0}\gamma(\to e^+e^-)$ data 89
8.3 Usage of pseudo-experiments 91

9 Results **97**
9.1 Angular observables 97
9.2 Photon polarization in $b \to s\gamma$ transitions 99
9.3 Branching fraction of the $B^0 \to K^{*0} e^+e^-$ decay 100

10 Conclusion **103**

A Appendix **105**
A.1 Angular observables in terms of transversity amplitudes 105

B Lists **107**
B.1 List of Figures 107

B.2 List of Tables 108

C Bibliography **109**

1 Introduction

The Standard Model (SM) of particle physics is currently the best known theory that describes fundamental interactions between particles. It covers three of the four fundamental interactions, namely the electromagnetic, weak and strong interaction. The Standard Model has been tested extensively over the past decades and has stood strong in nearly all experiments. But it is not a complete theory of fundamental interactions since it does not include a description of gravity and falls short of explaining some phenomena, such as the non-zero mass of neutrinos for example.
The last missing piece of the SM itself was experimentally found in 2012, when the ATLAS and CMS collaborations announced the discovery of the Higgs boson. So the quest of particle physics today is to find physics beyond the Standard Model (BSM physics).
This can be done in two different ways. The first option is to find new particles that are not part of the elementary particles predicted by the Standard Model, which are direct evidence of BSM physics. (One example are searches for Dark Matter particles.) The other option involves precision measurements of quantities that the Standard Model can predict. Deviations between experimental results and theory predictions would require BSM physics to explain them.
One ideal channel that is sensitive to possible BSM contributions is the transition of b quark to an s quark with the additional emission of a photon, $b \to s\gamma$. Decay processes that are mediated by this transition are suppressed in the SM, which makes them more susceptible to even small BSM contributions. The photons emitted in these $b \to s\gamma$ transitions predominantly have a left-handed polarization. A larger right-handed polarization would indicate BSM physics.

In this thesis, the $B^0 \to K^{*0} e^+ e^-$ decay is studied, which is mediated by the $b \to s\gamma$ transition with a virtual photon if one restricts the analysis to the very low region of dielectron invariant mass squared (q^2). The symbol K^{*0} denotes the $K^{*0}(892)$ meson reconstructed via its decay $K^{*0} \to K^+\pi^-$. The inclusion of charge-conjugate processes is implied throughout this thesis and natural units with $c = 1$ are used.
An angular analysis is performed, which allows the determination of the photon polarization in the $b \to s\gamma$ transition with great precision. In addition the branching fraction of the $B^0 \to K^{*0} e^+ e^-$ decay in the selected q^2 region is

measured. The data that is used in this analysis was recorded by the LHCb experiment in proton-proton collisions produced by the Large Hadron Collider (LHC) from 2011 to 2018.

This thesis is structured as follows. First, there is a short theoretical overview of the Standard Model and it is explained how an angular analysis of the $B^0 \to K^{*0} e^+ e^-$ decay can be used to measure the $b \to s\gamma$ photon polarization in Chapter 2. The LHCb detector is described in Chapter 3. Then an overview of the analysis strategy follows in Chapter 4. The data selection and background contributions are discussed in Chapter 5. The next Chapter 6 describes a fit to the invariant mass of the final state particles from which the branching fraction of the $B^0 \to K^{*0} e^+ e^-$ decay can be measured. This is followed by Chapter 7, where the angular fit is presented that is the integral part of the angular analysis. These fits are validated with different methods that are described in Chapter 8. At last, the results are presented and discussed in Chapter 9.

The author of this thesis worked together with other LHCb collaborators on the angular analysis presented here. The results of the angular analysis were published recently as part of an official LHCb analysis in Ref. [1]. In addition, the angular analysis is documented in detail in the PhD thesis of one of the LHCb collaborators in Ref. [2]. The author of this thesis contributed mainly to the angular fit and the fit validation in the angular analysis. In addition, the author performed the necessary steps to do the branching fraction measurement, which is presented here for the first time.
In order to deliver a comprehensive thesis, all parts of the analysis will be introduced. It will be marked, where work from the other collaborators is summarized.

2 Theory

2.1 Standard Model of particle physics

The Standard Model (SM) of particle physics is currently the best known quantum theory that describes the interactions of subatomic particles. It describes three of the four fundamental interactions, namely the electromagnetic, weak and strong interactions, while a quantum description of gravity is not included. The interactions between particles are mediated by spin 1 particles, called gauge vector bosons. The gluons mediate the strong interaction. There are eight types of gluons, each carrying a color and anti-color, which is the charge of the strong interaction. The $W^{\pm}$ and Z bosons mediate the weak interaction, while the photon γ mediates the electromagnetic interaction. The $W^{\pm}$ and Z bosons are massive and therefore have three degrees of freedom, called polarizations. The gluon and photon are massless and only have two possible polarizations.
The twelve fermions with spin 1/2 are the building blocks of matter in the SM. They are further divided into quarks and leptons. All fermions also have their associated anti-particle and participate in the weak interaction and, with exception of the three electrically neutral neutrinos, also in the electromagnetic interaction. The three neutrinos and the electron, muon and tau form the leptons. The six quarks carry an additional color charge and are therefore subject to the strong interaction. Due to the nature of the strong interaction, quarks are never observed as free particles and only form color neutral bound states consisting of a quark and anti-quark or three quarks, called mesons and baryons, respectively. Recently, also exotic states consisting of more quarks have been observed (see for example Ref. [3]). All particles that consist of quarks are called hadrons. The quarks are divided into *up-type* quarks (u,c,t) with electric charge $q = +2/3e$ and *down-type* quarks (d,s,b) with $q = -1/3e$. These types of quarks are referred to as quark flavor.
The last piece in the SM is the Higgs boson, which was experimentally found in 2012 [4, 5]. This spin 0 scalar particle provides a mechanism through which all other fundamental particles acquire their mass.
A summary of the elementary particles in the SM with their mass, charge and spin is given in Figure 2.1. As one can see, both quarks and leptons, appear in three so-called generations, where the second and third generation essentially are heavier copies of the first generation. The origin of this structure is

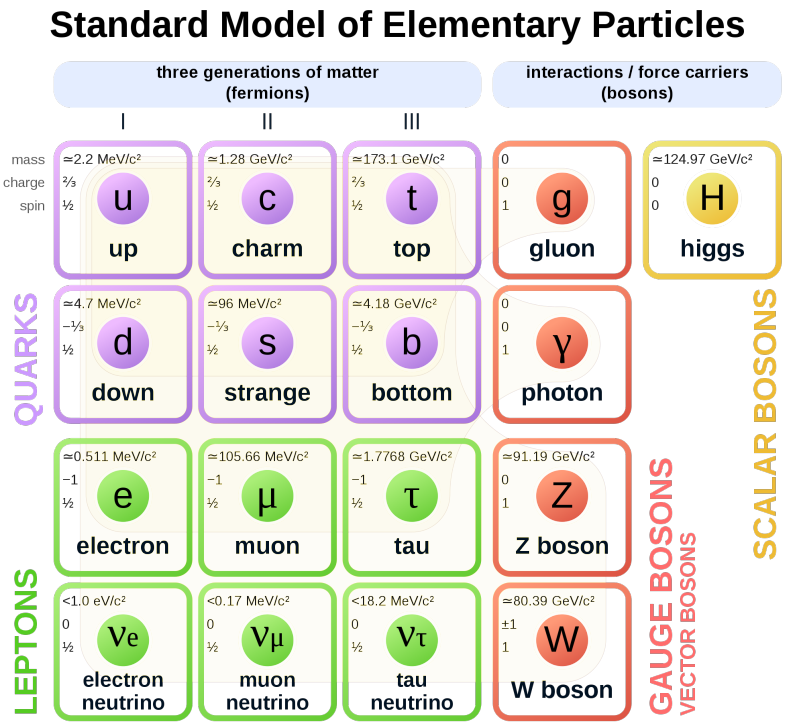

Figure 2.1: Overview of the elementary particles in the Standard Model with their main properties. From Ref. [6]

currently not understood in the SM.

2.2 The weak interaction of quarks

The weak interaction has the ability to change quark flavor. A common example is the β^- decay of radioactive materials, where a d quark changes into a u quark and therefore transforms a neutron into a proton inside the nucleus. The flavor-changing weak interaction is mediated by the charged W^+ and W^- bosons. In order to conserve electric charge, they only couple to pairs of fermions that differ by one unit of the elementary charge e. Charge neutral flavor-changing transitions (FCNC) are therefore forbidden at tree-level and are thus very suppressed in the SM.
The relative coupling strength of flavor-changing interactions between quarks

are described by the unitary Cabibbo-Kobayashi-Maskawa (CKM) matrix

$$V_{CKM} = \begin{pmatrix} V_{ud} & V_{us} & V_{ub} \\ V_{cd} & V_{cs} & V_{cb} \\ V_{td} & V_{ts} & V_{tb} \end{pmatrix} \tag{2.1}$$

where the transition between flavor i and flavor j is associated with the matrix element V_{ij}. The magnitudes and phases of the CKM matrix elements are not predictions of the SM but rather have to be measured from interactions of mesons and baryons containing the corresponding quarks (see for example Ref. [7]). The CKM matrix has near diagonal from and interactions between quarks of the same generation are favored. Interactions between quarks of different generations are heavily suppressed.

2.3 Beyond the Standard Model

The Standard Model had and still has unprecedented success in predicting a vast amount of observables that have been verified by experiments with very high precision. But the SM presents some shortcomings additional to a missing inclusion of general relativity and no explanation of the strong hierarchy in the CKM matrix, as mentioned above. In particular, the SM does not provide a mechanism to explain the non-vanishing neutrino mass [8] nor does it provide a Dark Matter candidate [9] or enough *CP* violation to explain the matter/anti-matter asymmetry in the universe [10], both of which are well established through cosmological observations. This therefore motivates theories that go beyond the Standard Model (BSM) and are able to solve at least some of the shortcomings of the SM.

There are two ways of searching for Beyond Standard Model physics experimentally. Firstly, one can find BSM physics directly, by producing new particles that are not part of the SM in highly energetic particle collisions. The world's most energetic accelerator for that is the Large Hadron Collider (LHC) [11] that reaches center-of-mass energies up to 13 TeV. This energy can be used to create particles with a mass up to the TeV scale. The best limits on searches for new particles at these scales are set by the ATLAS [12] and CMS [13] experiments, in for example Refs. [14, 15].

Secondly, one can measure known SM processes and look indirectly for deviations coming from BSM contributions. This relies on a precise measurement and theory prediction so that even small deviations can be spotted. Such indirect approaches have been quite successful in particle physics, such as the observation of CP violation in kaon decays that led to the prediction of a third

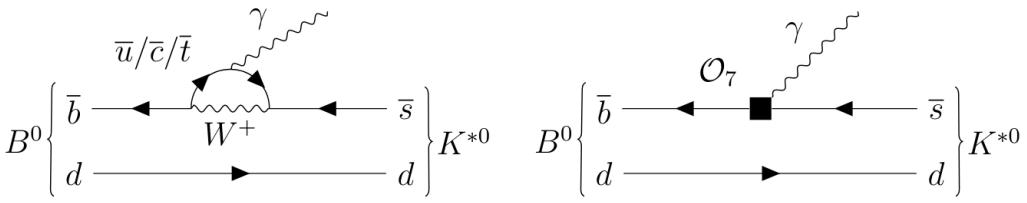

Figure 2.2: Example of a $b \to s\gamma$ transition with the $B^0 \to K^{*0}\gamma$ decay. One possible Feynman diagram is shown on the left, while the effective diagram is depicted on the right.

quark family [16, 17] several years before they (and even the c quark) were directly observed [18, 19].

2.4 The $b \to s\gamma$ transition

A well suited candidate for indirect searches for BSM physics are B decays involving the transition of a b quark to an s quark. This transition is a FCNC and forbidden in the SM at tree level. It is still possible, however, if the process occurs via electroweak loops in the Feynman diagrams, as depicted in Figure 2.2. This means that these processes are rare in the SM and thus more sensitive to BSM physics, which may contribute with new tree level diagrams (such as leptoquark models [20]) or new particles entering in the loop (such as a new light scalar [21]).
In addition, the mass of the b quark m_b provides advantages. It is much larger than the typical scale of the strong interaction ($m_b \gg \Lambda_{QCD}$) so that troublesome long-distance contributions are generally less important. At the same time, it is much smaller than the masses of the electroweak gauge bosons and the top quark. This allows the construction of an effective low-energy theory describing the quark interaction, similar to Fermi's effective theory of weak decays, where the four fermions would couple directly instead of the interaction being mediated by the heavy $W^\pm$ bosons. This effective approach is called Operator Product Expansion (OPE) [22], which separates the low-energy (large distance) from the high energy (small distance) degrees of freedom by building an effective Hamiltonian of the form

$$\langle f \,|\mathcal{H}_{\text{eff}}|\, i\rangle = \sum_k \mathcal{C}_k(\mu)\, \langle f \,|\mathcal{O}_k(\mu)|\, i\rangle \,, \tag{2.2}$$

where the low-energy part is encoded in the local operators $\mathcal{O}_k$ and the high-energy part is encoded in the so called Wilson coefficients $\mathcal{C}_k$, both depending

on the renormalization scale μ. As in Fermi's effective theory, the propagation of the high-energy degree of freedoms is reduced to point-like interactions with an effective coupling strength given by the Wilson coefficients (see Figure 2.2). The effective Hamiltonian of the $b \to s$ transition is given by [23]

$$\mathcal{H}_{\text{eff}} = -\frac{4G_F}{\sqrt{2}} V_{tb} V_{ts}^* \sum_k \left(\mathcal{C}_k \mathcal{O}_k + \mathcal{C}'_k \mathcal{O}'_k \right), \tag{2.3}$$

where G_F is the Fermi constant and V_{ij} are the CKM matrix elements. The relevant operators for the $b \to s\gamma$ transition are

$$\begin{aligned} \mathcal{O}_7 &= \frac{e}{16\pi^2} m_b \left(\bar{s} \sigma_{\mu\nu} P_{\text{R}} b \right) F^{\mu\nu}, \\ \mathcal{O}'_7 &= \frac{e}{16\pi^2} m_b \left(\bar{s} \sigma_{\mu\nu} P_{\text{L}} b \right) F^{\mu\nu} \end{aligned} \tag{2.4}$$

where e is the fundamental electric charge, $\sigma_{\mu\nu} = [\gamma_\mu, \gamma_\nu]$ and $P_{R,L} = (1 \pm \gamma_5)$ are the projectors on the right- (left-) handed chirality. The symbols $\overline{s}$ and b denote the fields for the quarks, while the electromagnetic field tensor $F_{\mu\nu}$ represents the photon involved in the $b \to s\gamma$ transition.
The Wilson coefficients are first calculated at the electroweak mass scale $\mu = m_W$ by matching the effective theory to the full SM theory. At this scale, corrections from QCD are small and can be calculated precisely. The Wilson coefficients are then developed down to $\mu = m_b$ using the renormalization group equations, which ensures that the QCD corrections are taken into account.
In this framework, contributions from BSM physics manifests itself by modifying the values of these coefficients or enhancing Wilson coefficients that are suppressed in the SM.
The Wilson coefficients $\mathcal{C}_7^{(\prime)}$ describe the helicity structure of the $b \to s\gamma$ transition. In the SM, the photon emitted in this transition is predominantly left-handed, since the weak interaction is left-handed. The contribution with right-handed polarization is suppressed by a factor

$$\frac{\mathcal{C}'_7}{\mathcal{C}_7} \simeq \frac{m_s}{m_b} \simeq 0.02 \tag{2.5}$$

up to QCD corrections [24]. On the other hand, many BSM theories allow for large right-handed currents, i.e. values of $\mathcal{C}'_7$, such as Minimally Supersymmetric Standard Models (MSSM) [25–28] or Left-Right Symmetric Models (LRSM) [29]. A measurement of the photon polarization in $b \to s\gamma$ transitions is therefore an excellent way of probing BSM physics.

2.5 Measuring the photon polarization with $B^0 \to K^{*0} e^+ e^-$ decays

The photon polarization in $b \to s\gamma$ transitions has been probed by several experiments by constraining the allowed values of the Wilson coefficients $\mathcal{C}_7^{(\prime)}$. Usually, observables in radiative decays with a photon in the final state are used as probe.

One possibility is the measurement of inclusive branching fractions of $B \to X_s\gamma$ decays, where X_s is any state containing an s quark. The branching fraction is proportional to $|\mathcal{C}_7|^2 + |\mathcal{C}_7'|^2$, and thus provides circular constraints in the $(\mathcal{C}_7, \mathcal{C}_7')$ plane. This measurement is performed by the Belle and BaBar collaborations [30–34]. The world average [35] is $\mathcal{B}(B \to X_s\gamma)_{exp}(E_\gamma > 1.6\,\text{GeV}) = (3.32 \pm 0.15) \times 10^{-4}$, which is in very good agreement with the SM prediction $\mathcal{B}(B \to X_s\gamma)_{th}(E_\gamma > 1.6\,\text{GeV}) = (3.36 \pm 0.23) \times 10^{-4}$ [36].

Other possibilities to probe the chirality of the $b \to s\gamma$ transition include measurements of mixing-induced CP asymmetries and time-dependent decay rates of radiative B^0 and B_s^0 decays. This is done by the Belle and BaBar collaborations in $B^0 \to K_S^0\pi^0\gamma$ decays [37,38] and by the LHCb collaboration in $B_s^0 \to \phi\gamma$ decays [39].

The analysis presented in this thesis focuses on another possibility. Instead of

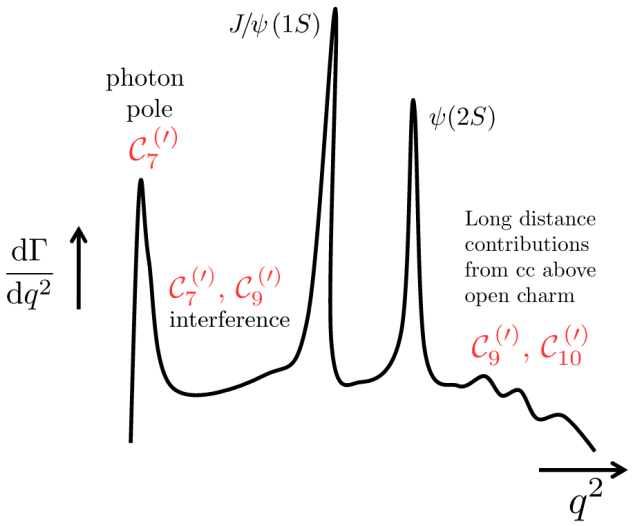

Figure 2.3: Artistic sketch of the $B^0 \to K^{*0}\ell^+\ell^-$ spectrum as function of q^2 [40]. The main Wilson coefficients contributing in the different q^2 regions are indicated on top of the curve.

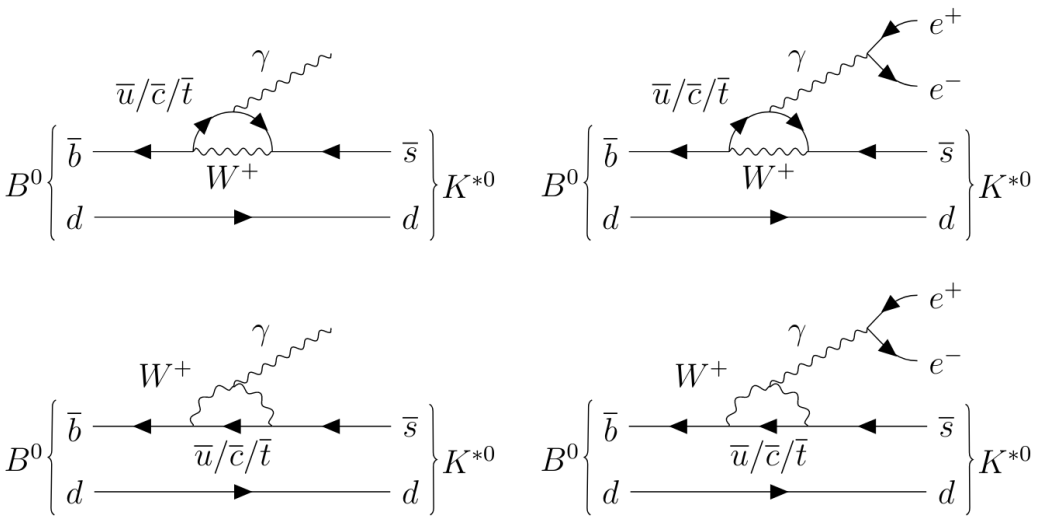

Figure 2.4: Dominant Feynman diagrams of the $B^0 \to K^{*0}\gamma$ decay (left) and $B^0 \to K^{*0}e^+e^-$ decay (right) at very-low q^2.

measuring the handedness of real photons in $b \to s\gamma$ transitions, virtual photons in $b \to s\ell^+\ell^-$ transitions that materialize into a dilepton pair are used. In order to isolate $b \to s\ell^+\ell^-$ transitions dominated by the $b \to s\gamma$ contribution, one has to restrict the analysis to a region of very low dilepton mass squared (q^2). Figure 2.3 sketches the q^2 spectrum of $B^0 \to K^{*0}\ell^+\ell^-$ decays that involve $b \to s\ell^+\ell^-$ transitions. The contribution of $\mathcal{C}_7^{(\prime)}$ is largely dominant at the low end of the q^2 spectrum and can thus be isolated from contributions of other Wilson coefficients such as $\mathcal{C}_9^{(\prime)}$ and $\mathcal{C}_{10}^{(\prime)}$. This region of very-low q^2 can only be accessed via $b \to se^+e^-$ transitions, however, due to the low mass of electrons compared to muons and taus [41, 42]. Figure 2.4 shows Feynman diagrams for the decays $B^0 \to K^{*0}\gamma$ and $B^0 \to K^{*0}e^+e^-$ that are dominant in the region of very-low q^2. The only difference between both decays is an additional electromagnetic vertex, which comes from the fact that the photon in $B^0 \to K^{*0}e^+e^-$ decays is virtual. It is therefore possible to study the photon polarization in $b \to s\gamma$ transitions with the decay $B^0 \to K^{*0}e^+e^-$ at very-low q^2.
One possible observable that can be studied in $B^0 \to K^{*0}e^+e^-$ decays is the branching fraction of this decay. The theoretical prediction of the branching fraction of $B^0 \to K^{*0}e^+e^-$ decays in the q^2 region considered in this thesis is $\mathcal{B}\left(B^0 \to K^{*0}e^+e^-\right)_{th} = (2.0 \pm 0.4) \times 10^{-7}$, as calculated with the FLAVIO software package [43]. This prediction comes with relatively large uncertainties due to hadronic form factors [44], so that the sensitivity to the photon polarization is reduced.

Another possibility is the study of angular distributions of the final state particles of the $B^0 \to K^{*0} e^+ e^-$ decay. As described below, angular observables can be defined that are sensitive to the photon polarization in $b \to s\gamma$ transitions. A previous angular analysis of $B^0 \to K^{*0} e^+ e^-$ decays was published by the LHCb collaboration in the q^2 region between 0.0002 and 1.120 GeV^2 [45]. This thesis presents an updated analysis, including a larger data sample and an improved selection process.

2.6 Differential decay width of the $B^0 \to K^{*0} e^+ e^-$ decay

The differential decay width of the $B^0 \to K^{*0} e^+ e^-$ decay can be described as a function of q^2 and three angles θ_l, θ_K and ϕ. The angle θ_l is defined as the angle between the direction of the e^+ and the direction opposite to that of the B^0 meson in the dielectron rest-frame. The angle θ_K is defined as the angle between the direction of the kaon and the direction opposite to that of the B^0 meson in the K^{*0} meson rest-frame. The angle ϕ is defined as the angle between the plane containing the electron and positron and the plane containing the kaon and pion in the B^0 meson rest-frame. This angular basis is chosen such that the angular definition for the $\overline{B}^0$ decay is the CP conjugate of that of the B^0 decay. These definitions are identical to those used for other angular analysis, such as Ref. [46], including the sign flip of ϕ ($\phi \to -\phi$) for the $\overline{B}^0$ decay. The angular basis is sketched in Figure 2.5. A detailed definition of the angles can be found in Ref. [2].
A description of the full angular decay distribution is derived in Ref. [47] starting from the matrix element of the effective Hamiltonian (see Equation 2.2). The angular decay distribution is defined as CP average between B^0 and $\overline{B}^0$ decays. In addition a limit of massless leptons is considered. With this, the

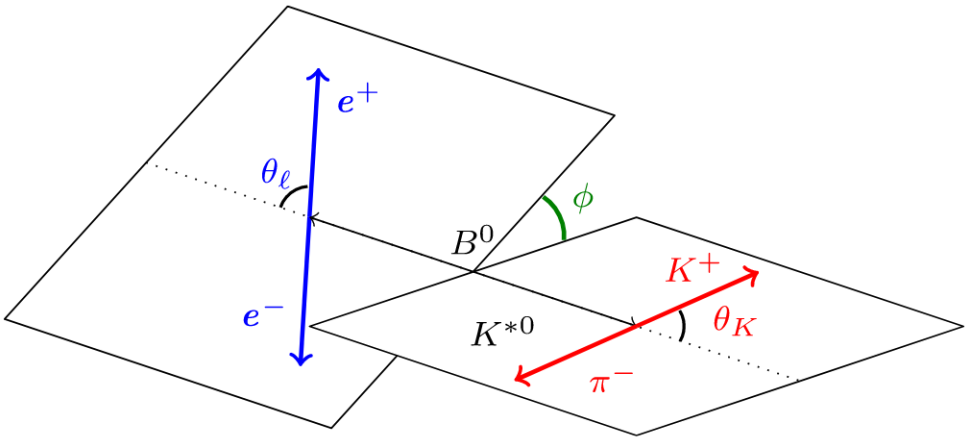

Figure 2.5: A sketch of the definition of the angular basis θ_l, θ_K and ϕ for the $B^0 \to K^{*0} e^+ e^-$ decay. From Ref. [40]

CP-averaged differential decay width reads

$$\begin{aligned}\left\langle \frac{d^4\Gamma}{dq^2\, d\cos\theta_\ell\, d\cos\theta_K\, d\phi} \right\rangle_{CP} = \frac{9}{32\pi} \Bigg\{ & \frac{3}{2}\left(1 - F_{\mathrm{L}}\right)\sin^2\theta_K + F_{\mathrm{L}}\cos^2\theta_K \\ & + \left[\frac{1}{2}\left(1 - F_{\mathrm{L}}\right)\sin^2\theta_K - F_{\mathrm{L}}\cos^2\theta_K\right]\cos 2\theta_l \\ & + S_3 \sin^2\theta_K \sin^2\theta_l \cos 2\phi \\ & + S_4 \sin 2\theta_K \sin 2\theta_l \cos\phi \\ & + S_5 \sin 2\theta_K \sin\theta_l \cos\phi \\ & + \frac{4}{3} A_{\mathrm{FB}} \sin^2\theta_K \cos\theta_l \\ & + A_7 \sin 2\theta_K \sin\theta_l \sin\phi \\ & + A_8 \sin 2\theta_K \sin 2\theta_l \sin\phi \\ & + A_9 \sin^2\theta_K \sin^2\theta_l \sin 2\phi \Bigg\}\,,\end{aligned} \tag{2.6}$$

with *CP* averaged observables S_i, *CP* asymmetries A_i, the forward-backward asymmetry, A_{FB}, and the longitudinal polarization fraction of the K^{*0} meson, F_{L}. This expression can be further simplified by applying the transformation

$$\tilde{\phi} = \begin{cases} \phi + \pi & \text{if } \phi < 0 \\ \phi & \text{if } \phi \geq 0 \end{cases} \tag{2.7}$$

to the angle ϕ. This folding cancels out terms that are proportional to $\sin\phi$ and $\cos\phi$ and thus reduces the number of free parameters. It does not affect the sensitivity to the photon polarization, however, as the sensitive observables are unchanged [48]. The remaining coefficients can be expressed in terms of transverse observables [49]

$$\begin{aligned} S_3 &= \frac{1}{2}\left(1 - F_{\mathrm{L}}\right) A_T^{(2)} \\ A_{\mathrm{FB}} &= \left(1 - F_{\mathrm{L}}\right) A_T^{Re} \\ A_9 &= \frac{1}{2}\left(1 - F_{\mathrm{L}}\right) A_T^{Im}, \end{aligned} \tag{2.8}$$

which are optimized observables for which the leading form-factor uncertainties cancel [49, 50]. This allows for more precise theoretical predictions.
The $B^0 \to K^{*0} e^+ e^-$ differential decay width can therefore be expressed as function of three angles θ_l, θ_K and $\tilde{\phi}$ and four angular observables F_{L}, $A_T^{(2)}$, A_T^{Re} and A_T^{Im} as

$$\begin{aligned} \left\langle \frac{d^4\Gamma}{dq^2 d\cos\theta_\ell d\cos\theta_K d\tilde{\phi}} \right\rangle_{CP} = \frac{9}{16\pi} \Bigg\{ & \frac{3}{4}\left(1 - F_{\mathrm{L}}\right)\sin^2\theta_K + F_{\mathrm{L}}\cos^2\theta_K \\ & + \left[\frac{1}{4}\left(1 - F_{\mathrm{L}}\right)\sin^2\theta_K - F_{\mathrm{L}}\cos^2\theta_K\right]\cos 2\theta_l \\ & + \frac{1}{2}\left(1 - F_{\mathrm{L}}\right) A_T^{(2)} \sin^2\theta_K \sin^2\theta_l \cos 2\tilde{\phi} \\ & + \left(1 - F_{\mathrm{L}}\right) A_T^{Re} \sin^2\theta_K \cos\theta_l \\ & + \frac{1}{2}\left(1 - F_{\mathrm{L}}\right) A_T^{Im} \sin^2\theta_K \sin^2\theta_l \sin 2\tilde{\phi} \Bigg\} \end{aligned} \tag{2.9}$$

The definition of the four angular observables in terms of transversity amplitudes A_0, $A_\perp$ and $A_{||}$ is given in Appendix A.1 and Ref. [49].
As mentioned, the observable F_{L} corresponds to the longitudinal polarization fraction of the K^{*0} meson. It is expected to be small at low q^2, since the virtual photon is quasi-real and therefore transversely polarized. The observable A_T^{Re} is related to the lepton forward-backward asymmetry A_{FB} as shown in Equation 2.8 [50]. The observable $A_T^{(2)}$ is averaged between B^0 and $\overline{B}^0$ decays, while A_T^{Im} corresponds to a CP asymmetry, as can be seen in Equation 2.8 [51].
The observables $A_T^{(2)}$ and A_T^{Im} depend only on the $B^0 \to K^{*0} e^+ e^-$ transversity amplitudes, $A_\perp$ and $A_{||}$, and vanish if these amplitudes are completely left-handed. In the limit of $q^2 \to 0$, which is a valid approximation for the q^2 region considered in this thesis, both observables are closely related to the photon polarization in $B^0 \to K^{*0}\gamma$ transitions. They can be related to the ratio of right-

to left-handed photon amplitudes, A_{R} and A_{L}, through [44, 50]

$$\begin{aligned} \tan\chi &\equiv |A_{\mathrm{R}}/A_{\mathrm{L}}| \\ A_T^{(2)} &= \sin(2\chi)\cos(\phi_7 - \phi_7')\cos(\delta_7 - \delta_7') \\ A_T^{Im} &= \sin(2\chi)\sin(\phi_7 - \phi_7')\cos(\delta_7 - \delta_7'), \end{aligned} \tag{2.10}$$

where $\phi_7^{(\prime)}$ is the weak phase and $\delta_7^{(\prime)}$ the strong phase of the corresponding Wilson coefficients $\mathcal{C}_7^{(\prime)} = |\mathcal{C}_7^{(\prime)}| e^{i\phi_7^{(\prime)}} e^{i\delta_7^{(\prime)}}$. Corrections to these approximations that could come from the influence of the Wilson coefficients C_9 and C_{10} are smaller than 0.006 even if large BSM effects are assumed [43]. As a final step the FLAVIO software package [43] (version 2.0.0) can be used to translate the photon polarization in $B^0 \to K^{*0}\gamma$ transitions to the photon polarization in $b \to s\gamma$ transitions, which can be expressed as the ratio of right- to left-handed $\mathcal{C}_7^{(\prime)}$ Wilson coefficients. In this calculation, hadronic contributions have to be taken into account [44].
The SM predictions for the four angular observables in the q^2 range considered in this thesis are

$$\begin{aligned} F_{\mathrm{L}}(\mathrm{SM}) &= 0.051 \pm 0.013 \\ A_T^{Re}(\mathrm{SM}) &= -0.0001 \pm 0.0004 \\ A_T^{(2)}(\mathrm{SM}) &= 0.033 \pm 0.020 \\ A_T^{Im}(\mathrm{SM}) &= -0.00012 \pm 0.00034 \end{aligned} \tag{2.11}$$

calculated using the FLAVIO software package [43, 44]. The theoretical uncertainties on the angular observables are much smaller than the experimental sensitivity of the results of this thesis.

3 The LHCb experiment at the LHC

3.1 The Large Hadron Collider

The Large Hadron Collider (LHC) [11] is the world's most energetic particle accelerator. It is located in Geneva, Switzerland, at the European Organization for Nuclear Research (CERN). The accelerator is housed underground in a 27 km long circular tunnel, crossing the French-Swiss border and passing under Lake Geneva. Two opposing beams of protons are kept on circular orbits by superconducting magnets, bringing them into collision at four interaction points, where the main LHC experiments are located.
The ATLAS [12] and CMS [13] experiments are designed as general purpose detectors and cover a wide spectrum of high energy physics. The ALICE [52] experiment is specialized in the study of heavy ion collisions aiming to achieve a better understanding of strongly interacting matter. The LHCb [53] experiment is dedicated to precision measurements in b and c hadrons. Is described in detail in the following Section 3.2.
The LHC started its operations in 2008 and functions as the highest center-of-mass energy stage of the CERN accelerator complex depicted in Figure 3.1. During operation in 2011 and 2012 it reached center-of-mass energies of $\sqrt{s} = 7$ TeV and $\sqrt{s} = 8$ TeV, respectively. This data taking period is denoted as Run 1, which enabled the discovery of the Higgs boson by the ATLAS and CMS experiments. The data taking was followed by an upgrade period where the center-of-mass energy was increased. From 2015 to 2018 the LHC ran at center-of-mass energies of 13 TeV collecting data in the so called Run 2. Since 2019 the accelerator complex is in a shutdown again, undergoing massive upgrades for the accelerators and experiments.

3.2 The LHCb experiment

The LHCb [53, 54] experiment is one of the four main experiments at the LHC. It is specialized in the study of b (and c) hadrons mainly produced through hadronization of $b\bar{b}$ quark-pairs produced in the proton-proton collisions of the LHC. Due to the high-energies provided by the LHC and the fact that the main $b\bar{b}$ production process at the LHC is gluon fusion, the $b\bar{b}$ quark-pairs are boosted in the forward or backward direction. The LHCb detector is therefore

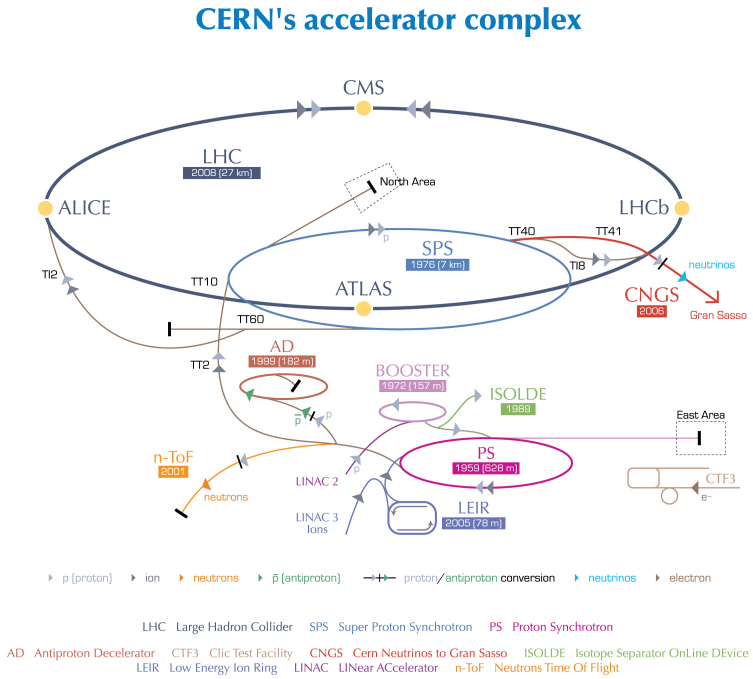

Figure 3.1: Sketch of the CERN accelerator complex. The date below each accelerator denotes the year this accelerator was first used. The lower stage accelerators do not only function as input to the LHC but also deliver beam to several other experiments. Taken from CERN-DI-0812015 and not to scale.

designed as a single-arm spectrometer covering the forward direction to detect $b\bar{b}$ quark-pairs and their decay products.
With that, the LHCb experiment has collected the world's largest data set of B meson decays that is used to make significant contributions in the field of flavor physics. Crucial to this achievement is an exact location of decay vertices as well as excellent momentum resolution and identification of the particles involved in the decay.
The general layout of the LHCb detector is shown in Figure 3.2. The proton-proton collisions happen inside the VErtex LOcator (VELO). This high precision tracking detector is used to measure the coordinates of vertices near the interaction point and to determine the impact parameter[1](IP) of tracks. A dipole magnet creates a magnetic field that bends the trajectory of charged particles. Tracking detectors before (upstream) and after (downstream) the

[1]The impact parameter is the transverse distance of closest approach between a particle track and a interaction vertex.

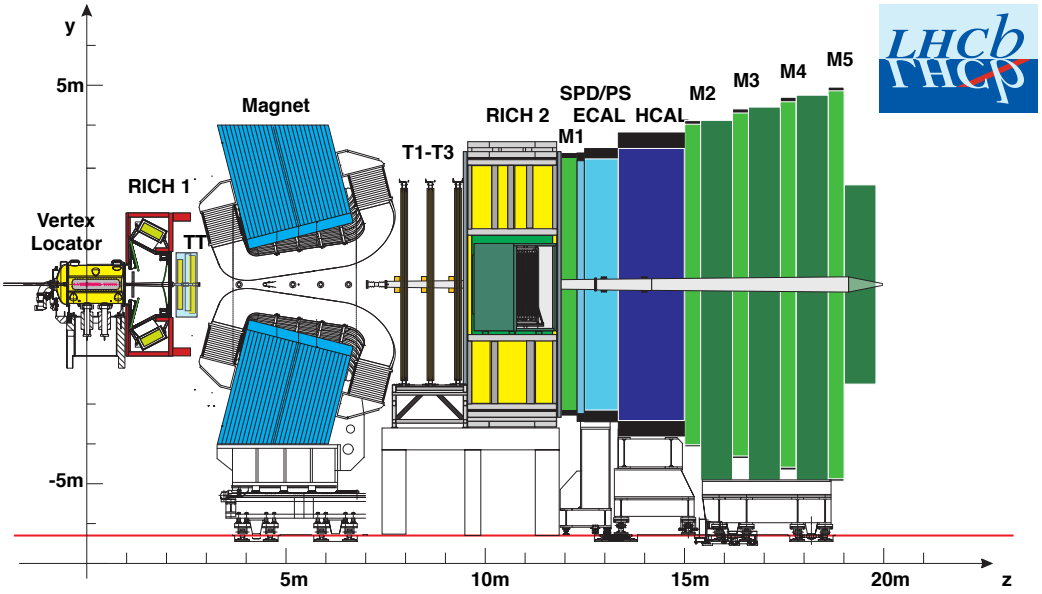

Figure 3.2: Schematic side view of the LHCb detector with the LHCb collaboration logo. A right-handed coordinate system is defined with z along the beam axis, y vertical and x horizontal. From Ref. [53].

magnet detect the trajectory of particles, enabling a momentum measurement. A calorimeter system consisting of Electromagnetic (ECAL) and Hadronic (HCAL) CALorimeters provides particles identification of electrons, photons and hadrons as well as a measurement of their energies. Additionally, particle identification for hadrons is provided by two Ring Imaging CHerenkov (RICH) detectors. Muon chambers located at the downstream end of the detector provide muon identification.

3.2.1 Tracking and vertex reconstruction

The tracking and vertexing system at LHCb is responsible for reconstructing vertices close to the proton-proton interaction point and measuring the momentum of charged particles by reconstructing their trajectories, called tracks.

Vertex reconstruction

Hadrons containing a b or c quark are long lived particles. At LHCb they typically travel a distance of a few millimeters before further decaying. Their daughter particles are therefore created at distinct vertices other than the primary interaction vertex (PV). The precise measurement of track coordinates in

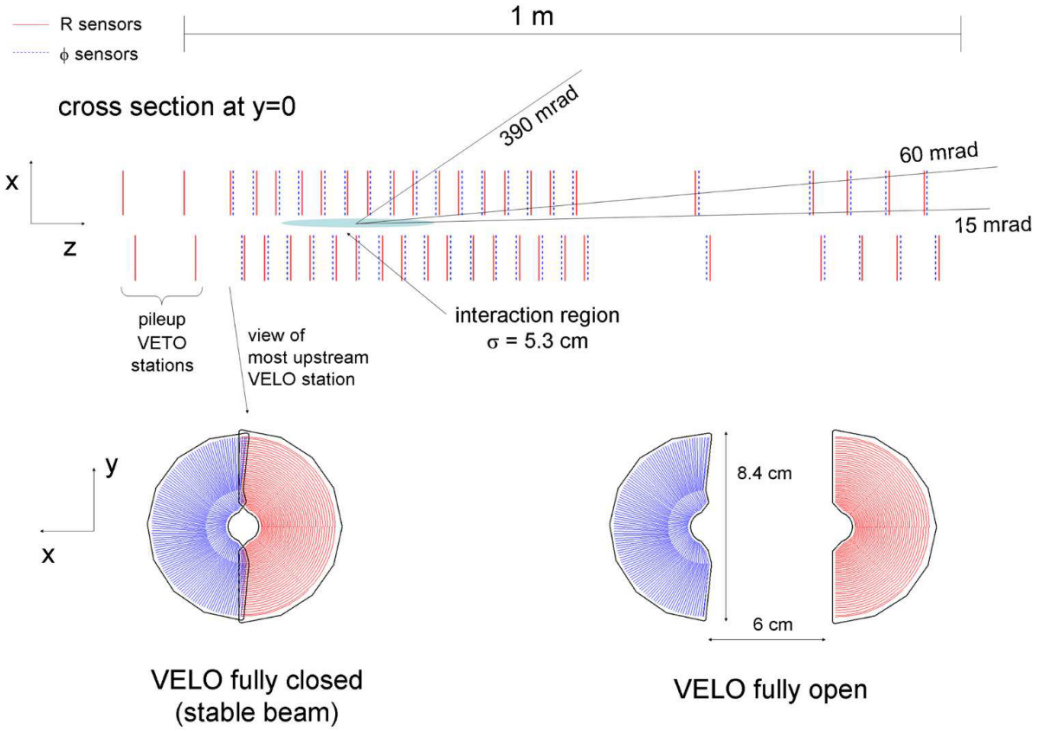

Figure 3.3: (Top) Cross-section in the (x, z) plane of the VELO detector in fully closed position. (Bottom) Front face of the VELO modules in closed (left) and open (right) position. From Ref. [53].

this region near the primary interaction point is provided by the VELO detector [55].
The VELO detector (Figure 3.3) consists of 21 stations of silicon semi-disks along the beam axis equipped with two silicon microstrip sensors. One sensor is used to measure the radial distance r, the other sensor to measure the azimuthal angle ϕ. The modules are as close as 8 mm to the beam axis during data taking and can be retracted when the detector is not used in order to not be damaged by the large beam size during injection.

Track reconstruction

A dipole magnet with an integrated magnetic field strength of about 4 Tm bends the trajectories of charged particles. The magnetic field created by the magnet is known with high precision. This allows the determination of a particle's momentum by measuring the bending radius of the particle's trajectory. This trajectory is detected by a series of tracking detectors installed upstream and downstream of the magnet. The four stations of the Trigger Tracker (TT) are

upstream of the magnet. The three downstream tracking stations (T1-3) are divided into two parts: the Inner Trackers (IT) close to the beam axis and the Outer Trackers (OT) [56] farther away. The same technology of silicon microstrip sensors is used for the TT and IT. Since the occupancy is lower in the outer region, drift-time detectors with straw-tubes are used for the OT. The best momentum resolution is achieved for tracks where information from all tracking stations and hits in the VELO detector are combined (so called *long tracks*). These long tracks have a relative momentum resolution $\delta p/p$ of $0.4\% - 1\%$ and tracking efficiencies of about 95% in the momentum range of interest for B meson decays.

3.2.2 Particle identification and energy measurement

After the momentum reconstruction for particles the remaining tasks for the detector is to provide an energy measurement for the particles and to identify their species. For charged particles these two are the same task, since particles are identified via their mass, which is connected to the energy via

$$E = \sqrt{p^2c^2 + m^2c^4}, \tag{3.1}$$

where E is the energy, p the momentum and m the mass of a particle and c the speed of light. At LHCb different techniques and subdetectors are used to provide particle identification: the two RICH detectors, the calorimeters and the muon system. Special care has to be taken for photons and electrons, as they come with some difficulties for the subsystems.

Ring-imaging Cherenkov detectors

The LHCb detector utilizes two RICH detectors [57] to identify and distinguish different charged hadrons. Most importantly, the subdetectors are able to distinguish kaons and pions, which are present in many decays of B mesons. The detection principle of RICH detectors is based on Cherenkov radiation that is emitted by particles traveling faster than the speed of light in a medium. This Cherenkov light is emitted in a cone with angle θ, depending on the particles velocity as

$$\theta = \frac{1}{n\beta}, \tag{3.2}$$

where n is the refractive index of the medium and β the particles velocity relative to the speed of light. Together with the momentum measurement this allows the determination of the mass through

$$m = \frac{p}{c\beta\gamma}, \tag{3.3}$$

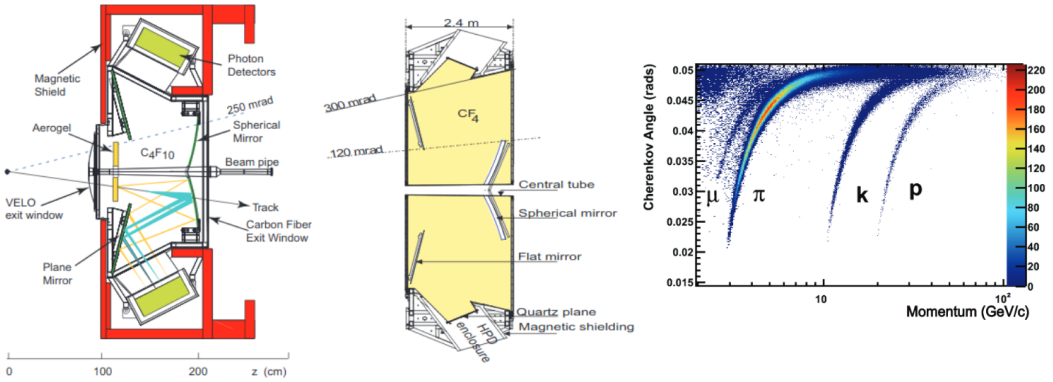

Figure 3.4: Schematic side view of the RICH 1 detector (left) and top view of RICH 2 detector (middle) [53]. Measured Cherenkov angle as a function of particle momentum for 2011 LHCb data (right) [57].

where $\gamma = 1/\sqrt{1-\beta^2}$ is the relativistic Lorentz factor. The RICH detectors are designed to measure the opening angle by projecting the Cherenkov light away from the beam axis onto photon detectors using an array of optical mirrors. RICH 1, located upstream, is optimized for low-momentum charged particles in the range $1 - 60\,\text{GeV}$, using a silica aerogel (removed in Run 2) and C_4F_{10} gas as radiators to produce the Cherenkov light. RICH 2 is located downstream and uses a CF_4 gas radiator to identify high-momentum particles in the range $15 - 100\,\text{GeV}$. A schematic view of both detectors as well as an illustration of the particle identification capabilities is shown in Figure 3.4.

Calorimeter system

The calorimeter system is located downstream of the RICH 2 detector and provides the identification of electrons, photons and hadrons, as well as a measurement of their energy and location. When high energetic particles interact with dense matter, they produce cascades of lower energetic particles that subsequently decay until all energy is absorbed. These so called *showers* are categorized depending on the initiating particle as either electromagnetic or hadronic. Electromagnetic showers are characterized by the radiation length X_0 and hadronic showers by the nuclear interaction length λ, with $X_0 \ll \lambda$. The calorimeter system consists of a Scintillator Pad Detector (SPD) and a Pre Shower (PS) detector separated by a lead plate, followed by the ECAL and HCAL detectors. All charged particles leave a hit in the SPD detector. Electrons and photons then start to initiate an electromagnetic shower in the lead plate, while hadrons do not. The electromagnetic showers of electrons and photons are contained by the ECAL, while the main energy deposition of

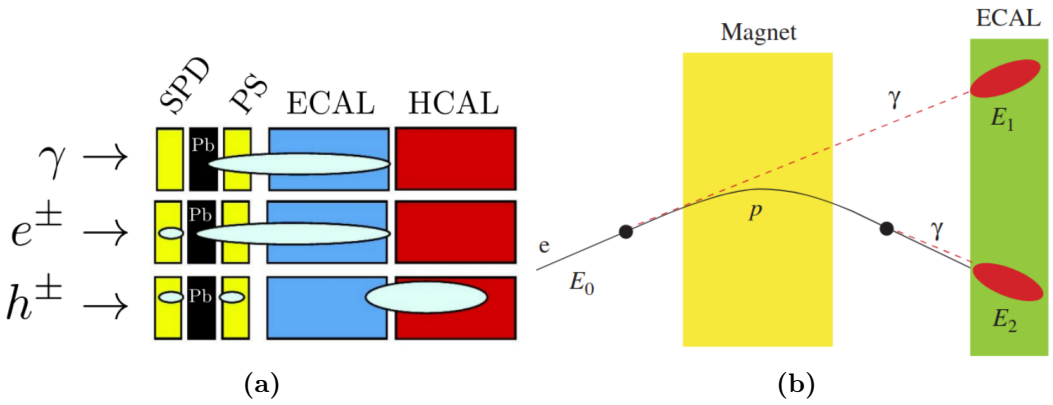

Figure 3.5: (a) Schematic explanation of particle identification with the calorimeter system between photons, electrons and hadrons [40]. (b) Schematic representation of bremsstrahlung photons emitted by an electron before and after the magnet [53].

hadrons is collected by the HCAL. Figure 3.5 (a) illustrates the particle identification capabilities of the calorimeter system. The energy deposition in the calorimeters is also used to provide a fast trigger for high energetic hadrons, electrons and photons.

Muon stations

The muon system [58] consists of five muon stations (M1-5) and provides the identification of muons as well as a fast trigger on muons. The stations M2-5 are located at the downstream end of the detector. They are equipped with MultiWire Proportional Chambers (MWPC) interleaved with thick iron absorber plates. Only high energetic muons with a momentum above 6 GeV are able to transverse all muon stations. The M1 station is located between RICH 2 and SPD and is designed to help triggering high transverse momentum muons.

Photon and electron reconstruction

The reconstruction of photons relies solely on the information from the ECAL. Since photons are neutral particles they do not leave hits in the trackers. They can only be reconstructed as clusters of energies in the ECAL with no pointing track to that cluster and no hit in the SPD in front of it. The relative energy resolution of the ECAL is at the level of $\sigma_E/E = 10\%/\sqrt{E} \oplus 1\%$ (with E given in GeV).
The correct energy reconstruction of electrons requires special care. Due to

their small mass, electrons are likely to emit collinear Bremsstrahlung photons when interacting with the material of the detector. If this happens downstream of the magnet (after the track of the electron is bent due to the magnetic field), this does not constitute a problem. The photon is emitted collinear to the electron's momentum and therefore ends up in the same ECAL region as the shower initiated by the electron. Its energy is added to the electron, therefore the energy measurement gives the correct value for the electron before emitting the photon in the first place. If the Bremsstrahlung photon is emitted upstream of the magnet, however, it does not end up in the same ECAL region. The electron track is bent by the magnet, while the photon continues on the original flight direction of the electron, as illustrated in Figure 3.5 (b). The energy emitted with the photon is lost and the measured momentum of the electron is biased towards lower values. A dedicated algorithm is used that searches for ECAL depositions coming from such lost Bremsstrahlung photons in order to add their energy back to the electron [59]. Not all Bremsstrahlung photons can be recovered and sometimes even too much energy is added. This procedure improves the momentum resolution for electrons but it is still much worse than for muons.

3.2.3 Trigger system

The proton beams cross each other with a frequency of 40 MHz at the LHCb interaction points. The amount of data produced in all these collisions is too large in order to be saved to disk. In addition, most of the collisions do not contain interesting events. The LHCb experiment therefore makes use of a three staged trigger system [60] that reduces the amount of data and only keeps the events deemed interesting.
The Level 0 (L0) trigger is implemented at hardware level and reduces the rate from 40 MHz to 1 MHz. It uses basic information from the calorimeters, muon chambers and the VELO in order to reconstruct the highest transverse energy hadron, electron and photon as well as the two highest transverse momentum muons. If the energy of one of this candidates is above a predefined threshold, the event is kept and sent to the next stage of the trigger.
The High Level Trigger (HLT) is a software based trigger divided into two parts, HLT1 and HLT2. The first stage HLT1 uses only parts of the full event data. Its main purpose is to select beauty and charmed decays by partial reconstruction of their decay products and some requirements on track quality and displaced vertices. The rate is reduced to a few tens of kHz.
The HLT2 trigger fully reconstructs the event. The exact procedure was changed during Run 1 and Run 2, where the computing capabilities were upgraded and a buffer was introduced, allowing a full event reconstruction online. Events are

kept by the HLT2 if they match a so called HLT2 *line*. These lines are a set of loose requirements aiming at selecting a specific type of decay. One can trigger on specific event topologies like two- or three-body decays, for example.
Events that have fired the L0 trigger and passed one or several HLT lines are saved to disk. For physics analysis the datasets are further split into so called *stripping lines*. These *stripping lines* correspond to sets of lose cuts and requirements in order to select events of a given type. For example, there is a stripping line, which is used to select $b \to s\ell^+\ell^-$ decays.

3.2.4 LHCb simulation

Monte Carlo (MC) simulation is an important tool in high energy physics, since it allows the study of various properties of the collisions and particles created as well as their response in the detector. In the LHCb simulation framework the proton-proton collisions are generated with the PYTHIA [61, 62] software, with a specific LHCb configuration [63]. The decay of generated particles is simulated by the EVTGEN [64] software. Final state radiation and photons are generated with the PHOTOS [65] software. The full LHCb detector and the interaction of simulated particles with the detector is simulated with the GEANT4 [66, 67] software. Then the simulated events are reconstructed using the same reconstruction software as used for real LHCb data [68].

4 Analysis overview

This thesis presents an angular analysis and branching fraction measurement of the $B^0 \to K^{*0} e^+ e^-$ decay in the q^2 interval between 0.0008 and 0.257 GeV^2. The symbol K^{*0} denotes the $K^{*0}(892)$ meson reconstructed via its decay $K^{*0} \to K^+ \pi^-$. The inclusion of charge-conjugated processes is implied throughout this thesis. In addition, natural units with $c = 1$ are used.

4.1 Data and simulation samples

The analysis uses a data sample of pp collision collected by the LHCb detector during 2011 and 2012 (Run 1), and 2015, 2016, 2017 and 2018 (Run 2). This corresponds to a total integrated luminosity of 9.1 fb^{-1}. Due to the different center-of-mass energies, this analysis is separated into two categories, labeled Run 1 and Run 2, according to the two data taking periods. Table 4.1 summarizes the center-of-mass energy and integrated luminosity corresponding to each year.
Suitable $B^0 \to K^{*0} e^+ e^-$ candidates have to trigger the LHCb detector and have to be selected from the recorded LHCb data (see Chapter 5). Signal candidates are triggered in two ways for this analysis. Since these triggers affect the angular distributions of $B^0 \to K^{*0} e^+ e^-$ candidates, they are treated separately in two additional categories (see Section 5.1) throughout this analysis.
Furthermore, this analysis uses simulated MC samples to compute efficiencies of the selection process, to model the mass and angular shapes, to train a multivariate classifier to separate background and to study specific backgrounds. These simulated samples are generated for each year of data taking with the same energy and detector conditions as in data and reconstructed with the same reconstruction software that is used on data, as described in Section 3.2.4.

4.2 Choice of q^2 region

The q^2 region under study is chosen in order to maximize the sensitivity to $b \to s\gamma$ contributions in the decay $B^0 \to K^{*0} e^+ e^-$ (see Section 2.5).
First of all, the reconstructed invariant mass of the dielectron pair differs from the true dielectron mass due to the non-negligible electron momentum resolu-

Table 4.1: Summary of the data samples used in the analysis with the integrated luminosity and center-of-mass energy corresponding to each year of data-taking.

Year	$\mathcal{L}[\,\mathrm{fb}^{-1}]$	$\sqrt{s}[\,\mathrm{TeV}]$
2011	1.1	3.5
2012	2.1	4.0
2015	0.3	6.5
2016	1.7	6.5
2017	1.7	6.5
2018	2.2	6.5

tion. The resolution can be improved by recomputing the four vectors of the electrons in a kinematic fit that constrains the $K^+\pi^-e^+e^-$ mass to the nominal B^0 mass of 5279.65 MeV [69] and constrains the vertices. The invariant mass of the dielectron pair computed in this fit is called $m_{ee}^{B^0}$ and is used to select the events relevant for this analysis.
Signal candidates with the lowest q^2 are most sensitive to the Wilson coefficient $C_7^{(\prime)}$. The lower boundary of the q^2 region should therefore be low as possible, in principle down to the threshold at $q^2 = (2m_e)^2$. However, at small dielectron invariant mass the resolution in $\tilde{\phi}$ is degraded due to multiple scattering of the quasi-collinear electrons in the tracking detectors. In addition, $B^0 \to K^{*0}\gamma$ decays, where the photon converts into a dielectron pair in the material of the detector, contaminate the lower end of the q^2 spectrum. The dielectron invariant mass is therefore required to be larger than $m_{ee}^{B^0} > 10$ MeV, resulting in a $\tilde{\phi}$ resolution of 0.11 rad and a $B^0 \to K^{*0}\gamma$ background fraction of about 2% (see Section 5.3.2).
The choice of the upper boundary of the q^2 region is a trade-off between retaining as many signal candidates as possible and reducing the sensitivity to the $C_9^{(\prime)}$ and $C_{10}^{(\prime)}$ Wilson coefficients. In addition, unwanted resonances such as the ρ^0 resonance at 770 MeV with its large width of 149 MeV should be excluded. An upper limit of $m_{ee}^{B^0} < 500$ MeV is chosen.
The analysis is therefore performed on $B^0 \to K^{*0}e^+e^-$ candidates with a q^2 in the range $m_{ee}^{B^0} \in [10, 500]$ MeV. This region is referred to as very-low q^2-bin. However, due to the resolution of the reconstructed dielectron invariant mass, the q^2 requirement does not have a uniform efficiency when compared to the true dielectron invariant mass obtained from simulation, especially close to the boundaries (see Figure 4.1). This presents a problem for theoretical predictions,

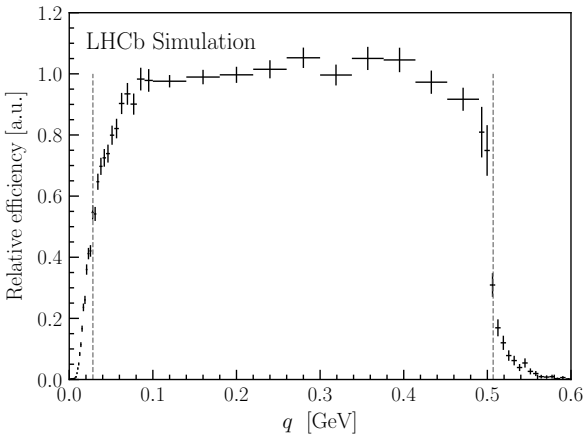

Figure 4.1: Relative efficiency as function of dielectron invariant mass q. The points represent the efficiency obtained from simulation, while the vertical lines represent the effective q^2 boundaries.

which are based on the true q^2, when comparing them to experimental results of this analysis, if the efficiency description is unknown. Following Ref. [45], effective q^2 boundaries are defined between 0.0008 GeV^2 and 0.257 GeV^2 to allow theoretical predictions without the input from LHCb simulation. Using the FLAVIO [43] software package, it is checked that predicitions with both SM and BSM values for the Wilson coefficients calculated in this effective q^2 range (grey line in Fig. 4.1) agree very well with those calculated taking into account a complete description of the q^2 efficiency using LHCb simulation (points in Fig. 4.1).

4.3 Control channels

The region of q^2 with $m_{ee}^{B^0} \in [0, 10]$ MeV is considered as a control channel for this analysis, denoted as gamma q^2-bin. Due to the large branching fraction of the $B^0 \to K^{*0}\gamma$ decay (about two orders of magnitude larger than for the $B^0 \to K^{*0}e^+e^-$ decay), the reconstructed $B^0 \to K^{*0}e^+e^-$ candidates are dominated by $B^0 \to K^{*0}\gamma(\to e^+e^-)$ decays in this q^2 region, where the photon converts into a dielectron pair in the material of the detector (see Section 5.3.2). These candidates have very similar kinematics as the $B^0 \to K^{*0}e^+e^-$ signal candidates but with much larger candidate yields and the background level in the gamma q^2-bin is similar to the very-low q^2-bin. The gamma q^2-bin is therefore used as a control channel in the fits of this analysis.
At LHCb the branching fraction of a decay is almost always measured with respect to a reference channel, because the total number of mother particles

(here B^0 mesons) produced in the detector is unknown. The $B^0 \to K^{*0}\gamma$ decay with the photon conversion $\gamma \to e^+e^-$ can not be used as the reference channel for the branching fraction measurement of the $B^0 \to K^{*0}e^+e^-$ decay, however, since the photon conversion efficiency is unknown as it depends on an accurate detector material simulation, which is hard to obtain. The decay $B^0 \to K^{*0}\gamma$ itself (i.e. reconstructing the photon) is not a fully charged final state and therefore introduces additional experimental challenges.
Instead, the decay $B^0 \to K^{*0}J/\psi\,(\to e^+e^-)$ is a good reference channel for the branching fraction measurement. The decay via the J/ψ resonance has a large branching fraction and fully charged final state. In addition it can be selected quite cleanly in $B^0 \to K^{*0}e^+e^-$ candidates, since the dielectron pair stems from the J/ψ resonance and the dielectron invariant mass should therefore equal the J/ψ mass. Hence, the region of q^2 with $m_{ee}^{B^0} \in [6, 11]$ GeV, called jpsi q^2-bin, is used as reference channel, where candidates come from the resonant decay mode $B^0 \to K^{*0}J/\psi\,(\to e^+e^-)$.

4.4 Maximum likelihood fits

This analysis relies on the Maximum Likelihood method to obtain estimates of fit parameters. This method is based on the construction of the likelihood function L, which is the combined probability distribution of all measurements. The best estimate of parameters is given by the set of parameters that maximizes the likelihood function. The Maximum Likelihood method is frequently used because of its good statistical properties [70]. The Maximum Likelihood Estimators (MLE) are

- asymptotically unbiased: With larger number of measurements they converge to the true value.
- consistent: With larger number of measurements they get more precise.
- efficient: Asymptotically they have minimal variance.
- commutative: They are invariant under reparameterization.

Given a set of n random variables $\vec{x} = (x_1, \cdots, x_n)$ that are modeled by a probability density function (PDF) that depends on a set of m unknown parameters $\vec{\theta} = (\theta_1, \cdots \theta_m)$, one can write the likelihood function of N measurements of the set of n variables as

$$L(\vec{x}; \vec{\theta}) = \prod_{i=1}^{N} f\left(x_1^i, \cdots, x_n^i; \theta_1, \cdots, \theta_m\right), \tag{4.1}$$

where f is the joint PDF for a single measurement. The best fit estimates of the parameters are usually found numerically by minimizing the negative logarithm of the likelihood function. In this analysis, the RooFit [71] software package that is part of the Root [72, 73] software framework is used.
One can perform simultaneous fits in several categories by simply multiplying the corresponding likelihood functions of the categories that are build from the measurements belonging to the respective category. It is possible to share fit parameters between the categories, if the PDF of each category depends on the common parameters.
If the number of measurements N itself is a random variable one has to extend the likelihood function. In almost all physics cases, the number of measurements N follows a Poisson distribution, with average μ that may depend on the m unknown parameters. One defines the extended likelihood function as

$$L = \frac{e^{-\mu(\theta_1,\cdots,\theta_m)}\mu\left(\theta_1,\cdots,\theta_m\right)^N}{N!}\prod_{i=1}^{N} f\left(x_1^i,\cdots,x_n^i;\theta_1,\cdots,\theta_m\right). \tag{4.2}$$

The number of measurements N is now additional information that is used to determine the parameters, along side the distribution of the data.
If the maximum likelihood fit is performed as an unbinned fit, the PDF is constructed for each measurement individually and then combined to the likelihood function. In case of very large number of measurements this may become unpractical from a numerical point of view, as the implementation would require intensive computing power. In these cases one can perform a binned fit, where the distributions of the random variables are binned and only the number of entries in each bin is used as information, which again follows a Poisson distribution. The expected number of entries in each bin again depends on the model PDF and unknown parameters.

4.5 Analysis strategy

A pure sample of $B^0 \to K^{*0}e^+e^-$ candidates is obtained from LHCb data with the selection described in Chapter 5. Then, a fit to the reconstructed $K^+\pi^-e^+e^-$ invariant mass, $m(K^+\pi^-e^+e^-)$, in a wide range between 4500 and 6200 MeV is used to estimate the remaining background contamination, as described in Chapter 6.
The mass fit is performed as a simultaneous unbinned maximum likelihood fit in eight categories (see Section 6.2): The two data taking periods times the two trigger decisions and simultaneous in the signal and control channel. The inclusion of the control channel improves the modeling of the background contributions. An additional binned extended maximum likelihood fit is performed

in the reference channel to extract possible data and MC simulation differences and to extract the yield in the reference channel for the branching fraction measurement (see Section 6.1). Together with the efficiencies obtained from simulation (see Section 5.4), this yield is used as external constraint in an extended maximum likelihood fit to the signal channel in order to measure the branching fraction of the $B^0 \to K^{*0} e^+ e^-$ decay.
The angular observables F_{L}, A_T^{Re}, $A_T^{(2)}$ and A_T^{Im} are determined from a four-dimensional fit to the $K^+\pi^- e^+ e^-$ invariant mass and the three angles $\cos\theta_\ell$, $\cos\theta_K$ and $\tilde{\phi}$, as described in Chaper 7. This fit is performed in a reduced $m(K^+\pi^- e^+ e^-)$ window between 5000 and 5400 MeV in order to ease the angular modeling of background components. The background fractions are constrained to their values obtained from the mass fit in the wider $m(K^+\pi^- e^+ e^-)$ window. The angular fit is performed as a simultaneous unbinned maximum likelihood fit in the four trigger categories, where especially the angular observables F_{L}, A_T^{Re}, $A_T^{(2)}$ and A_T^{Im} are shared among the categories.
An angular fit to the $m(K^+\pi^- e^+ e^-)$ invariant mass and the angle $\cos\theta_K$ is performed on the control channel sample (see Section 8.2). This fit functions as excellent validation of the fit procedure and background treatment. Additional fit validation is performed through pseudo-experiments and the study of MC simulation (see Section 8.3).

5 Data selection

In order to perform studies on a specific decay, candidates of this decay have to be selected from the data recorded with the experiment. This chapter explains how $B^0 \to K^{*0} e^+ e^-$ candidates are selected from the LHCb data and how the contamination of background processes in the selected candidates is minimized. The selection requirements are developed and studied as part of the official LHCb analysis [1, 2]. The author of this thesis contributed to the calculation of efficiencies that are relevant for the branching fraction measurement.

5.1 Trigger and pre-selection

As explained in Section 3.2.3, only events which have fired the L0 trigger are saved. In this analysis for $B^0 \to K^{*0} e^+ e^-$ candidates this predominantly happens in two ways:

- At least one of the electrons belonging to the signal candidate has fired the L0 electron trigger. These events are referred to as L0 Lepton (L0L) category.
- The event was triggered by a particle not belonging to the signal candidate. Since b hadrons are produced in pairs at LHCb, these events are usually triggered by a decay product of the other b hadron. The events are therefore referred to as L0 Independent (L0I) category.

In principle, an event can be triggered by both requirements. In order to assure mutually exclusive categories, events in the L0I category are additionally required to not have passed the electron trigger on signal candidates. These exclusive categories are important, because the shape of the reconstructed $m(K^+\pi^- e^+ e^-)$ mass as well as the background contributions and angular acceptance depend on the L0 trigger. The analysis is therefore split in the two independent trigger categories L0L and L0I.
After the L0 hardware trigger the $B^0 \to K^{*0} e^+ e^-$ events have to pass the HLT software trigger as explained in Section 3.2.3. The software trigger employs topological lines and is trained to find a two-, three-, or four-track vertex that is significantly displaced from the a primary pp interaction (PV). In addition, at least one charged particle has to have a significant transverse momentum (p_{T})

and has to be inconsistent with originating from any PV. Lastly, a multivariate algorithm is used to identify displaced vertices consistent with the decay of a b hadron.
The stripping line `Bu2LLKeeLine2` is used to select $B^0 \to K^{*0}e^+e^-$ candidates from data. The requirements of this line are complemented by pre-selection requirements.
The $B^0 \to K^{*0}e^+e^-$ candidates are formed by combining a K^{*0} candidate with a pair of oppositely charged tracks that were identified[1] as electrons. The K^{*0} candidate is formed from a pair of charged tracks identified as K^+ and π^- mesons.
All tracks are required to have high transverse momentum, be inconsistent with originating from a PV and have a good track quality. The track quality is characterized by a small χ^2/ndf, which is the χ^2 of the fit to the track divided by the number of degrees of freedom. The inconsistency to a PV is measured by the χ^2_{IP}, which is the difference in χ^2 of the fit to the PV vertex, when it is reconstructed with and without the track under consideration. In addition, the probability[2] of a track to be fake and originating from random combinations of hits in the tracker has to be low.
The originating vertices of the electron pair, the K^{*0} meson and the B^0 meson have to be of good quality and be displaced from the PV as well. Additionally, the angle (called `DIRA`) between the B^0-candidate momentum vector and the vector between the associated PV and the B^0 decay vertex has to be small.
Lastly, requirements on the reconstructed mass of the candidates are applied. The reconstructed mass of the $K^+\pi^-$ system has to be within 100 MeV of the mass of the K^{*0} meson. The range on the reconstructed mass of the B^0-candidate is chosen as $m(K^+\pi^-e^+e^-) \in [4500, 6200]$ MeV. An overview of all requirements on $B^0 \to K^{*0}e^+e^-$ candidates can be found in Table 5.3 and Table 5.4.

5.2 Data and simulation differences

This analysis relies on the usage of Monte Carlo (MC) simulation to characterize signal and background contributions. The LHCb MC simulation, however, is know to not perfectly reproduce the LHCb data. These differences have to be corrected for by weighting the MC distributions of specific variables to match the data. The weights are computed using a general approach developed by

[1] Particle identification variables are computed using a likelihood method (`DLL` and `PIDX`) or a neural network algorithm [74] (`ProbNN`) based on information from all subdetectors
[2] The variable `GhostProb` is calculated from a dedicated neural-network algorithm [75] based on tracking information.

the LHCb collaboration for tests of lepton universality [59].
The particle identification response of MC samples is estimated using collaboration wide efficiency tables [76]. They are produced separately for each year of data taking and particle species. Weights are calculated as functions of the momentum p and the pseudo-rapidity η.
The L0 trigger response is corrected for both trigger categories. For the L0L category the weights are computed as function of the electron transverse energy and the region of the ECAL in which the electron was triggered. For the L0I category the weights are computed as function of the B^0-candidate transverse momentum.
Differences in the MC simulation in B kinematics and event multiplicity are corrected for as function of

- B kinematics: B transverse momentum and pseudo-rapidity
- Multiplicity: number of PVs and number of tracks in VELO detector.

Since these proxy variables are correlated, a multivariate classifier is used to compute the weights. Additional differences due to reconstruction effects are corrected for as function of reconstructed B transverse momentum and pseudo-rapidity, the χ^2 of the vertex fit and the χ^2 of the impact parameter of the B meson. The weights are again computed with the use of a second multivariate classifier.
More detail on the data/MC corrections can be found in Ref. [2] and references therein.

5.3 Background contributions

The selection of $B^0 \to K^{*0}e^+e^-$ candidates requires a final state consisting of a kaon and pion, compatible with originating from a K^{*0} meson, as well as a pair of oppositely charged electrons. It is not given that all events that end up being selected stem from the signal decay $B^0 \to K^{*0}e^+e^-$. Instead, other decays where one or several final state particles were missed or misidentified by the detector can contribute to the $B^0 \to K^{*0}e^+e^-$ candidates as well and pass the stripping and pre-selection. In fact, since the decay $B^0 \to K^{*0}e^+e^-$ is rare, the contribution of other decays may be sizable so that they have to be included and modeled in the mass and angular fits. These decays are therefore studied and specific veto requirements are developed to reduce their contributions.

5.3.1 Semi-leptonic background

A large background comes from the semi-leptonic $B^0 \to D^- e^+ \nu$ decay, where the D^- meson decays via $D^- \to K^{*0} e^- \overline{\nu}$. This decay has the same final state as the signal $B^0 \to K^{*0} e^+ e^-$ decay, since neutrinos are not measured by the LHCb detector. Additionally, its branching fraction is four orders of magnitude larger than that of the signal. In the case where both neutrinos have low energies, the signal selection is ineffective at rejecting these decays.
The positron from the B^0 decays tends to be more energetic than the electron from the D^- decay. This energy asymmetry reflects onto the $\cos\theta_\ell$ distribution, since $\cos\theta_\ell$ can be expressed as

$$\cos\theta_\ell \sim \frac{E_{e^+} - E_{e^-}}{E_{e^+} + E_{e^-}} \qquad \text{for } B^0 \text{ and} \qquad \cos\theta_\ell \sim \frac{E_{e^-} - E_{e^+}}{E_{e^+} + E_{e^-}} \qquad \text{for } \overline{B}^0. \quad (5.1)$$

The semi-leptonic decays peak at high values of $\cos\theta_\ell$. Therefore a cut on the angle $|\cos\theta_\ell < 0.8|$ is chosen. It is made symmetric in order to avoid introducing a potential systematic effect on the angular observable A_T^{Re} (which is related to the forward-backward asymmetry and therefore to an asymmetry in the $\cos\theta_\ell$ distribution). About 5% of the signal $B^0 \to K^{*0} e^+ e^-$ is lost by this requirement. But the terms sensitive to the photon polarization involving $A_T^{(2)}$ and A_T^{Im} are proportional to $\sin^2\theta_L$ and therefore less affected by this cut. On the other hand the requirement on $\cos\theta_\ell$ reduces the contamination of semi-leptonic decays by 98%.
Still, this semi-leptonic background remains a sizable contribution of about 6% of $B^0 \to K^{*0} e^+ e^-$ candidates. This background is therefore included in the mass and angular fit. Since it is very hard to disentangle from combinatorial background, the modeling of mass and angular shape is combined with the combinatorial background into a single shape for the mass and angular fit (called SL/C).

5.3.2 $B^0 \to K^{*0}\gamma(\to e^+e^-)$ background

An important background to this analysis comes from radiative $B^0 \to K^{*0}\gamma$ decays. When the photon interacts with the material of the detector and converts into an e^+e^- pair, this decay has the exact same final state as the signal decay $B^0 \to K^{*0} e^+ e^-$. In addition, its branching fraction is two orders of magnitude larger than for the $B^0 \to K^{*0} e^+ e^-$ decay.
In the q^2 range of this analysis the only difference between the decays $B^0 \to K^{*0}\gamma(\to e^+e^-)$ and the signal $B^0 \to K^{*0} e^+ e^-$ is that the photon is real and not virtual. The dielectron pair formed by the conversion of the real photon only acquires mass through the momentum transfer of the nucleus of the material.

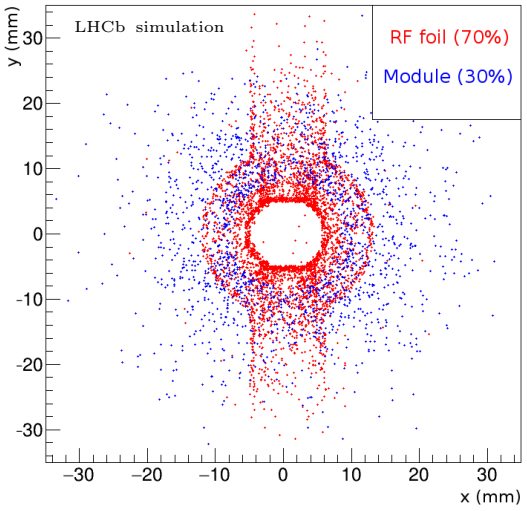

Figure 5.1: Conversion point of $B^0 \to K^{*0}\gamma(\to e^+e^-)$ simulated events converting in the VELO material in the (x, y) plane. In red (blue) the conversion happened in the RF foil (modules) of the VELO detector, respectively.

Therefore, the dielectron mass of $B^0 \to K^{*0}\gamma(\to e^+e^-)$ decays is usually very small. Most of these background decays have $m_{ee} < 10\,\text{MeV}$ and are thus not part of the very-low q^2-bin considered in the analysis. Instead, they form the gamma q^2-bin, which is used as control channel as introduced in Section 4.3. Still, the contamination of $B^0 \to K^{*0}\gamma(\to e^+e^-)$ to $B^0 \to K^{*0}e^+e^-$ decays reaches about 25% in the very-low q^2-bin. Therefore a specific veto is developed, which reduces the contamination. Studying the distribution of the conversion point of the photon in $B^0 \to K^{*0}\gamma(\to e^+e^-)$ MC simulation, one can see that most photons are converted when interacting with the nucleus of the VELO detector material. Figure 5.1 depicts the distribution of conversion points. About 70% of the conversion occur in the material of the RF foil[3] of the VELO detector, while the other 30% occur in the material of the modules. Therefore, $B^0 \to K^{*0}\gamma(\to e^+e^-)$ decays can be vetoed by rejecting events where the dielectron origin vertex is compatible with a region where there is material of the detector.
One can define the distance to the nearest VELO module in uncertainty space as

$$\sigma_{\text{mod}} = \sqrt{\left(\frac{\delta_x}{\sigma_x}\right)^2 + \left(\frac{\delta_y}{\sigma_y}\right)^2 + \left(\frac{\delta_z}{\sigma_z}\right)^2}, \tag{5.2}$$

[3]The RF foil is a thin aluminum foil that shields the VELO modules against the primary LHC vacuum.

where $\delta_{x,y,z}$ are the distances in real space between the reconstructed dielectron vertex and the nearest point in the VELO module, and $\sigma_{x,y,z}$ are the uncertainties of the vertex position. In order to find the distance to the closest VELO module, a precise mapping of the VELO detector material is required. This map is produced for the LHCb VELO detector using beam-gas collisions [77]. The cut value is chosen as $\sigma_{\text{mod}} > 0.3$ as a trade-off between rejecting $B^0 \to K^{*0}\gamma(\to e^+e^-)$ decays and keeping $B^0 \to K^{*0}e^+e^-$ signal decays. After applying this cut, the background contamination of $B^0 \to K^{*0}\gamma(\to e^+e^-)$ decays is as low as 2%, while the signal efficiency is above 99%. This background contribution is modeled and included in the angular and mass fit. The gamma q^2-bin, where the $B^0 \to K^{*0}\gamma(\to e^+e^-)$ dominates, is further used as control channel and included in the mass fit, as explained in Section 6.2.

5.3.3 $B^0 \to K^{*0}\pi^0/\eta$ backgrounds

The decays of $B^0 \to K^{*0}\pi^0$ and $B^0 \to K^{*0}\eta$ can contribute as background in this analysis. Different subsequent decays play a role, depending on the q^2 bin and main signal decay.

Dalitz decays

In the very-low q^2-bin ($m_{ee} \in [10, 500]$ MeV), another background to $B^0 \to K^{*0}e^+e^-$ candidates comes from $B^0 \to K^{*0}\pi^0$ and $B^0 \to K^{*0}\eta$ decays, when the π^0 or η meson decays to $e^+e^-\gamma$. These so called Dalitz decays [78] can end up being selected in two ways. Either the photon is missed, but is soft so that the reconstructed $m(K^+\pi^-e^+e^-)$ mass still falls into the selected B^0 mass region, or the photon is added as a bremsstrahlung photon to one of the electrons, resulting in no energy loss. The latter case results in a $m(K^+\pi^-e^+e^-)$ mass distribution that peaks at the B^0 mass.
The branching fractions of both decays are small compared to the signal $B^0 \to K^{*0}e^+e^-$ decay (one to two orders of magnitude), but the very-low q^2-bin covers the whole phase space that is occupied by these Dalitz decays. The contamination in the mass range of the angular fit is at the level of 4% (2%) for the η (π^0) Dalitz decay, respectively, estimated using MC simulation.
There is no specific veto applied to these backgrounds, but both are modeled and included in the mass and angular fit as background contribution in the very-low q^2-bin.

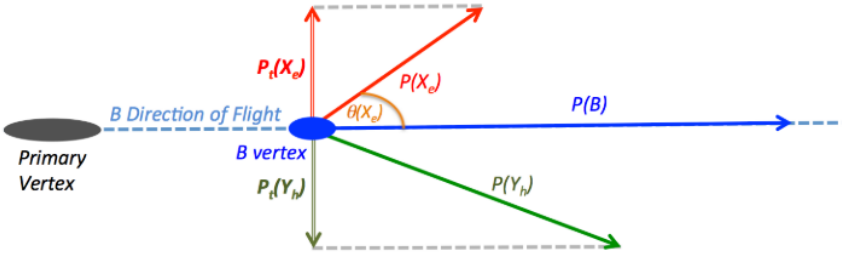

Figure 5.2: Sketch of the kinematics of a $B \to Y_h X_e$ decay, where Y_h is the hadronic part (here the K^{*0} meson) and X_e the leptonic part (here the dielectron pair). From Ref. [79]

Diphoton decays

In the gamma q^2-bin ($m_{ee} \in [0, 10]$ MeV), the subsequent decay of the π^0 and η meson into two photons, where one photon converts into a e^+e^- pair, can be a background to $B^0 \to K^{*0}\gamma(\to e^+e^-)$ decays. The other photon is either lost or recovered as bremsstrahlung photon, similar to the Dalitz decays.
The decays $B^0 \to K^{*0}\pi^0(\to \gamma(\to e^+e^-)\gamma)$ and $B^0 \to K^{*0}\eta(\to \gamma(\to e^+e^-)\gamma)$ are negligible in the very-low q^2-bin. Their contribution in the gamma q^2-bin to $B^0 \to K^{*0}\gamma(\to e^+e^-)$ candidates is about 6% to 10% depending on the decay and trigger category. Both backgrounds are modeled in the gamma q^2-bin and included to the mass fit (see Section 6.2) and angular fit to the control channel (see Section 8.2).

5.3.4 Partially reconstructed background

Another large background contribution stems from partially reconstructed decays. These are decays of a B meson into $B \to K^{*0}Xe^+e^-$, where X represents a particle that was not reconstructed. In decays relevant to this analysis X mostly comprises missed pions. One can suppress these background contributions by exploiting the kinematic imbalance of the decay, with the concept of the HOP[4] mass [79].
Looking at the kinematic balance along the plane transverse to the B^0 flight direction, as sketched in Figure 5.2, one can define the ratio of the transverse momentum of the hadronic part over the leptonic part as

$$\alpha_{\text{HOP}} = \frac{p_T\left(K^{*0}\right)}{p_T\left(e^+e^-\right)}. \tag{5.3}$$

[4]This acronym doesn't have a meaning. Some sources say it is connected to a particular French regional airline ...

If this ratio is unequal to unity, it means that some energy is missing in the final state. For signal $B^0 \to K^{*0}e^+e^-$ candidates, this missing energy is most likely lost in the leptonic part due to emission of bremsstrahlung photons. These bremsstrahlung photons are emitted in the same direction as the electron. Therefore, the fraction of transverse momentum that is lost, is the same as the fraction of longitudinal momentum lost. Hence, one can recover the full momentum using

$$p_{corr}\left(e^+e^-\right) = \alpha_{\mathrm{HOP}} \cdot p\left(e^+e^-\right). \tag{5.4}$$

The corrected momentum can then be used to recompute the invariant mass of the B^0 candidate, $m_{\mathrm{HOP}}(K^+\pi^-e^+e^-)$.
The correct recovery of the momentum does not work in the case of partially reconstructed background, since the missing particles have no reason to fly in the same direction as the electron. The distribution of m_{HOP} therefore has discriminating power between signal and partially reconstructed background. In order to not sculpt the mass shape of the signal a rather loose veto cut of $m_{\mathrm{HOP}}(K^+\pi^-e^+e^-) > 4900\,\mathrm{MeV}$ is chosen. This veto reduces the amount of partially reconstructed background by 70%, while the signal efficiency is above 90%.

5.3.5 Combinatorial background

When the reconstruction algorithm tries to find $B^0 \to K^{*0}e^+e^-$ candidates among the many tracks produced in the proton-proton collision, it is common that a candidate is formed by combining random tracks present in the event due to other decays. This type of background is called combinatorial background and it is present in almost every analysis. In order to reduce this background a multivariate classifier is used that separates signal from combinatorial background candidates.
The multivariate classifier used in this analysis is based on a boosted decision tree algoritm (BDT) [80]. As this is a form of supervised learning, the BDT has to be trained on labeled data. The sample used to model the signal is taken from $B^0 \to K^{*0}e^+e^-$ MC simulation, while the sample used to model the background is taken from the upper invariant mass sideband ($m(K^+\pi^-e^+e^-) > 5600\,\mathrm{MeV}$). The classifier uses eight kinematic and decay topology variables as listed in Table 5.1. These variables are chosen because their distribution is different for the signal and background samples. The strongest discriminating power is given by the χ^2 of the kinematic fit to the full decay chain, the p_{T} of the B^0 candidate and the χ^2_{IP} of the electron.
Two independent BDTs are used for Run 1 and Run 2, due to the different

Table 5.1: Training variables used for the multivariate classifier that are found to have discriminating power between signal and background.

Particle	Variables
B^0	p_{T} $\chi^2_{\mathrm{FD\_OWNPV}}$, $\chi^2_{\mathrm{DTF}}/\mathrm{ndf}$
K^{*0}	$\log \chi^2_{\mathrm{IP\_OWNPV}}$
h	$\log \chi^2_{\mathrm{IP\_OWNPV}}$
$e^{\pm}$	$min(\log \chi^2_{\mathrm{IP\_OWNPV},e^+},\ \log \chi^2_{\mathrm{IP\_OWNPV},e^-})$
e^+e^-	$\log \chi^2_{\mathrm{IP\_OWNPV}}$

center-of-mass energy. In addition a different BDT cut for the two trigger categories is allowed, since the level of combinatorial background is expected to the higher in the L0I category than in the L0L category.
The BDT is optimized by maximizing the figure of merit $S/\sqrt{S+B}$, where S and B are estimations of the signal and background yield in the angular fit window $m(K^+\pi^-e^+e^-) \in [5000, 5400]$ MeV. The yields S and B are summed over both runs and trigger categories. The set of cuts that maximizes the figure of merit is {BDT Run 1 L0L > 0.2, BDT Run 1 L0I > 0.4, BDT Run 2 L0L > 0.3, BDT Run 2 L0I > 0.4}. For this set of cuts, the signal efficiency is about 94% with a background rejection of about 90%. More detail on the training of the classifier can be found in Ref. [2].

5.3.6 Other background contributions

There are several other processes that can contribute to $B^0 \to K^{*0}e^+e^-$ candidates. The processes listed in the following are studied and found to be negligible in the signal channel after applying dedicated vetoes. They are therefore not modeled and included in the mass and angular fit. More detail on these background contributions can be found in Ref. [2].

$B_s^0 \to \phi e^+e^-$ background

Other species of B mesons can also contribute to background processes. One example is the $B_s^0 \to \phi e^+e^-$ decays, where $\phi \to K^+K^-$. If one of the kaons is misidentified as a pion, the ϕ meson can be reconstructed as a K^{*0} meson instead. This background is removed by a veto cut on the invariant mass of the two hadrons, computed under the assumption that both hadrons are kaons, $m(K^+(\pi^- \to K^-)) > 1040\,\mathrm{MeV}$. The signal efficiency of this cut is estimated

from MC simulation and found to be above 99%.

$B^+ \to K^+e^+e^-$ background

Another species of B mesons can contaminate the signal, through $B^+ \to K^+e^+e^-$. This decay can mimic the signal if a random pion is associated to the kaon to form a K^{*0} candidate or if the kaon is misidentified as a pion and a random kaon is picked up instead.
This decay is not expected to contribute in the very-low q^2-bin, since the di-electron pair does not come from a virtual photon and its invariant mass is expected to be larger.
On the other hand, the decay $B^+ \to K^+J/\psi(\to e^+e^-)$ is present in the jpsi q^2-bin. Since the mass fit in the jpsi q^2-bin is relevant for data/MC differences and the branching ratio measurement, this background is removed by a veto cut. The invariant mass $m(K^+e^+e^-)$ and $m((\pi \to K)e^+e^-)$ are required to be lower than 5100 MeV. The efficiency of this cut on signal $B^0 \to K^{*0}J/\psi(\to e^+e^-)$ decays is estimated from MC simulation and above 99%.

$\Lambda_b^0 \to pK^-e^+e^-$ background

Events coming from $\Lambda_b^0 \to pK^-e^+e^-$ decays can pass the selection in case of misidentification $\pi \to p$ or double misidentification $\pi \to K$ and $K \to p$. The contamination of this decay to $B^0 \to K^{*0}e^+e^-$ decays is estimated from MC simulation and found to be below 1%.

$\pi \to e$ misidentification

The misidentification of a pion as an electron can lead to additional background contributions. These would come from similar decay chains as the semi-leptonic background, where the D meson would decay to $D^- \to K^{*0}(\to K^+\pi^-)\pi^-$, for example. It was checked that these backgrounds are not present in data.
The double misidentification of $\pi \to e$ would allow contamination from $B^0 \to K^{*0}\pi^+\pi^-$. Due to the pion mass, this background would be expected to have a larger q^2 with little leakage to the very-low q^2-bin considered in the analysis. It is checked that the contribution from this decay is negligible.

K^{*0} and $\overline{K}^{*0}$ misidentification

The misidentification of a K^{*0} meson as a $\overline{K}^{*0}$ meson can happen through double misidentification of the pion to a kaon and vice versa. This background would lead to an important bias in the angular observables. The measured flavor of the K^{*0} meson defines the measured flavor of the B^0. Depending

on the flavor of the B^0 meson, a sign flip is included in the definition of the angles (see Section 2.6). This sign flip in the angles introduces a bias in the angular observables F_{L}, A_T^{Re} and A_T^{Im}. The observable $A_T^{(2)}$ is unaffected, since it represents a CP averaged observable.
It is checked that the contribution of double misidentification is negligible.

5.3.7 Selection of $B^0 \to K^{*0} J/\psi\,(\to e^+e^-)$ candidates

The decay $B^0 \to K^{*0} J/\psi\,(\to e^+e^-)$ is used as a reference channel for the branching ratio measurement in this analysis. It is selected from data in the q^2 region with $m_{ee}^{B^0} \in [6, 11]$ GeV, where the dielectron pair stems from the J/ψ meson. Since the q^2 of this region is different, some of the background contributions discussed above are not relevant to $B^0 \to K^{*0} J/\psi\,(\to e^+e^-)$ candidates, while others are more important.
The rejection of partially reconstructed background through the m_{HOP} cut does not work well in the q^2 region of the J/ψ meson. Instead a similar momentum correction can be applied, where the B mass is recomputed with the constraint that the dielectron invariant mass equals the J/ψ meson mass, called $m_{B^0}^{J/\psi}$. The partially reconstructed background in $B^0 \to K^{*0} J/\psi\,(\to e^+e^-)$ candidates can therefore be reduced by requiring $m_{B^0}^{J/\psi} > 5150\,\mathrm{MeV}$. This cut is only applied in the reference channel.

5.4 Selection summary and efficiencies

The full selection of the analysis, as applied on top of the trigger requirements (see Section 5.1), is shown in Table 5.3 and 5.4. In case of duplicated requirements, the harsher requirement of the selection is applied on top of the stripping requirement.
Table 5.5 and Table 5.6 show the selection efficiencies of $B^0 \to K^{*0} e^+e^-$ candidates and $B^0 \to K^{*0} J/\psi\,(\to e^+e^-)$ candidates, respectively. The selection efficiency is computed from MC simulation for each year of data taking and the contributions of individual cuts are listed separately:

- **geo**: The geometric efficiency is due to the fact that the MC simulation is restricted to the LHCb detector acceptance.
- **reco**: The reconstruction efficiency includes the reconstruction and preselection requirements.
- **PIDw**: This represents the efficiency of the PID requirements on the particles.

- **HOP**: This represents the efficiency of the m_{HOP} cut. It is only applied for $B^0 \to K^{*0} e^+ e^-$ candidates.
- **BDT**: This represents the efficiency of the BDT requirement on the signal.
- **ctLPk**: This efficiency includes the veto for photon conversions in the detector material and the symmetric cut on the $\cos\theta_\ell$ angle.
- **total**: Total selection efficiency per year as product of individual steps. This value is not given in percent.

Table 5.7 shows the ratio of the selection efficiency of $B^0 \to K^{*0} e^+ e^-$ candidates over $B^0 \to K^{*0} J/\psi\,(\to e^+ e^-)$ candidates for each year and step in the selection. The ratios are close to unity and consistent between the years of the data taking periods.
These selection efficiencies are relevant as input for the branching ratio measurement. In the branching ratio measurement it is required that the efficiencies are split up into the four fit categories, the two data taking periods times the two trigger categories. The simulation samples for each data-taking year are weighted so that their relative contribution is consistent with the luminosity acquired in each year (from Table 4.1). The efficiencies that are used as input for the branching ratio measurement are shown in Table 5.2.

Table 5.2: Summary of selection efficiencies for $B^0 \to K^{*0} e^+ e^-$ and $B^0 \to K^{*0} J/\psi\,(\to e^+ e^-)$ candidates per category. These efficiencies are used as input to the branching ratio measurement.

	$\epsilon_{ee}\left(B^0 \to K^{*0} e^+ e^-\right)$ [%]	$\epsilon_{J/\psi}\left(B^0 \to K^{*0} J/\psi\,(\to e^+ e^-)\right)$ [%]
Run 1 L0L	0.0760 ± 0.0007	0.1090 ± 0.0004
Run 1 L0I	0.0440 ± 0.0005	0.02862 ± 0.00016
Run 2 L0L	0.1251 ± 0.0007	0.1604 ± 0.0004
Run 2 L0I	0.0643 ± 0.0005	0.04134 ± 0.00014

Table 5.3: Summary of the stripping requirements implemented in the `Bu2LLKeeLine2` line.

Type	**Requirement**
Global	`nSPDHits` $< 600(450)$ Run 1 (Run 2)
B	$\lvert m - m_B^{\mathrm{PDG}} \rvert < 1500\,\mathrm{MeV}$
	`DIRA` > 0.9995
	$\chi^2_{\mathrm{IP}}(primary) < 25$
	end vertex $\chi^2/\mathrm{ndf} < 9$
	primary vertex χ^2 separation > 100
K^{*0}	$\lvert m - m_{K^{*0}}^{PDG} \rvert < 300\,\mathrm{MeV}$
	$p_{\mathrm{T}} > 500\,\mathrm{MeV}$
	origin vertex $\chi^2/\mathrm{ndf} < 25$
K	$\mathtt{DLL}_{K\pi} > -5$
	$\chi^2_{\mathrm{IP}}(primary) > 9(4)$
π	$\chi^2_{\mathrm{IP}}(primary) > 9$
$\ell\ell$	$m < 5500\,\mathrm{MeV}$
	end vertex $\chi^2/\mathrm{ndf} < 9$
	origin vertex χ^2 separation > 16
e	$\mathtt{DLL}_{e\pi} > 0$
	$p_{\mathrm{T}} > 300\,\mathrm{MeV}$
	$\chi^2_{\mathrm{IP}}(primary) > 9$

Table 5.4: Summary of the selection cuts applied on top of the stripping and trigger requirements.

Type		**Requirement**
Quality	all tracks	$\chi^2/ndf < 3$
		`GhostProb` < 0.4
	e	Inside ECAL acceptance
ID	K^{*0}	$\lvert m(K\pi) - m^{PDG}_{K^{*0}}\rvert < 100\,\text{MeV}$
PID	all	Has hits in the RICH detectors
	e	Has deposited a signal inside the ECAL
	K, π	$p_T > 250\,\text{MeV}$
	e	$p_T > 500\,\text{MeV}$
	K	`ProbNNk` $\times (1 -$ `ProbNNp`$) > 0.05$
		& `K_PIDK` > 0
	π	`ProbNNpi` $\times (1 -$ `ProbNNk`$)$
		$\times (1 -$ `ProbNNp`$) > 0.1$
	e	`V3ProbNNe` > 0.2 & `E_PIDe > 2`
BKG	Semi-leptonic	$\lvert\cos\theta_\ell\rvert < 0.8$
	$B^0 \to K^{*0}\gamma(\to e^+e^-)$	$\sigma_{\text{mod}} > 0.3$
	$B^0_s \to \phi e^+e^-$	$m(K(\pi \to K)) > 1040\,\text{MeV}$
	Partially reconstructed	$m_{\text{HOP}}(K^+\pi^-e^+e^-) > 4900\,\text{MeV}$
	Combinatorial Run 1	L0L : $BDT > 0.2$, L0I : $BDT > 0.4$
	Combinatorial Run 2	L0L : $BDT > 0.3$, L0I : $BDT > 0.4$
Mass ranges	$m(K^+\pi^-e^+e^-)$	$m(K^+\pi^-e^+e^-) \in [4500, 6200]\,\text{MeV}$
	very-low q^2-bin	$m^{B^0}_{ee} \in [10, 500]$ MeV
	gamma q^2-bin	$m^{B^0}_{ee} \in [0, 10]$ MeV

Table 5.5: Selection efficiencies of $B^0 \to K^{*0} e^+ e^-$ events computed from MC simulation.

year	geo [%]	reco [%]	PIDw [%]	HOP [%]	BDT [%]	ctLPk [%]	total
2011	15.99 ± 0.02	1.19 ± 0.01	84.44 ± 0.44	93.00 ± 0.25	95.36 ± 0.24	93.67 ± 0.25	$(1.33 \pm 0.02) \times 10^{-3}$
2012	16.35 ± 0.02	1.00 ± 0.01	84.25 ± 0.36	92.60 ± 0.20	94.76 ± 0.19	93.22 ± 0.20	$(1.13 \pm 0.01) \times 10^{-3}$
2015	17.35 ± 0.03	1.46 ± 0.02	74.66 ± 0.52	93.26 ± 0.26	94.72 ± 0.27	93.26 ± 0.27	$(1.56 \pm 0.02) \times 10^{-3}$
2016	17.31 ± 0.04	1.92 ± 0.01	77.00 ± 0.20	92.98 ± 0.11	92.79 ± 0.13	94.15 ± 0.10	$(2.08 \pm 0.01) \times 10^{-3}$
2017	17.32 ± 0.04	1.88 ± 0.01	75.08 ± 0.33	93.00 ± 0.17	93.24 ± 0.19	94.11 ± 0.16	$(1.99 \pm 0.02) \times 10^{-3}$
2018	17.35 ± 0.04	1.65 ± 0.01	73.77 ± 0.36	92.73 ± 0.18	93.67 ± 0.19	93.52 ± 0.18	$(1.72 \pm 0.02) \times 10^{-3}$

Table 5.6: Selection efficiencies of $B^0 \to K^{*0} J/\psi (\to e^+ e^-)$ events computed from MC simulation.

year	geo [%]	reco [%]	PIDw [%]	HOP [%]	BDT [%]	ctLPk [%]	total
2011	15.32 ± 0.02	1.50 ± 0.01	85.67 ± 0.14	100.00 ± 0	94.02 ± 0.08	83.70 ± 0.12	$(1.55 \pm 0.01) \times 10^{-3}$
2012	15.63 ± 0.02	1.22 ± 0.00	85.54 ± 0.12	100.00 ± 0	93.50 ± 0.07	83.58 ± 0.10	$(1.28 \pm 0.01) \times 10^{-3}$
2015	16.64 ± 0.03	1.81 ± 0.01	73.77 ± 0.18	100.00 ± 0	92.02 ± 0.11	83.08 ± 0.14	$(1.70 \pm 0.01) \times 10^{-3}$
2016	16.68 ± 0.03	2.32 ± 0.01	76.42 ± 0.07	100.00 ± 0	90.18 ± 0.05	83.20 ± 0.05	$(2.22 \pm 0.01) \times 10^{-3}$
2017	16.68 ± 0.03	2.22 ± 0.01	73.79 ± 0.11	100.00 ± 0	90.37 ± 0.07	83.34 ± 0.08	$(2.06 \pm 0.01) \times 10^{-3}$
2018	16.68 ± 0.03	2.02 ± 0.01	72.85 ± 0.12	100.00 ± 0	90.54 ± 0.07	83.44 ± 0.09	$(1.86 \pm 0.01) \times 10^{-3}$

Table 5.7: Ratio of selection efficiencies per year and selection step.

year	geo	reco	PIDw	HOP	BDT	ctLPk	total
2011	1.044 ± 0.002	0.791 ± 0.009	0.986 ± 0.005	0.930 ± 0.003	1.014 ± 0.003	1.119 ± 0.003	0.86 ± 0.01
2012	1.046 ± 0.002	0.819 ± 0.007	0.985 ± 0.004	0.926 ± 0.002	1.014 ± 0.002	1.115 ± 0.003	0.88 ± 0.01
2015	1.043 ± 0.002	0.808 ± 0.010	1.012 ± 0.007	0.933 ± 0.003	1.029 ± 0.003	1.122 ± 0.004	0.92 ± 0.01
2016	1.038 ± 0.003	0.826 ± 0.004	1.008 ± 0.003	0.930 ± 0.001	1.029 ± 0.002	1.132 ± 0.001	0.94 ± 0.01
2017	1.039 ± 0.003	0.845 ± 0.007	1.018 ± 0.005	0.930 ± 0.002	1.032 ± 0.002	1.129 ± 0.002	0.97 ± 0.01
2018	1.040 ± 0.003	0.817 ± 0.007	1.013 ± 0.005	0.927 ± 0.002	1.035 ± 0.002	1.121 ± 0.002	0.93 ± 0.01

6 Mass fits

After the selection of signal candidates, the data still contains contributions from various backgrounds in addition to the signal events, as described in the previous Section 5.3. To extract the yield or fraction of signal events in data one has to perform a fit to a quantity that allows a separation of signal and background contributions. This quantity is typically the invariant mass of all particles in the final state, here $m(K^+\pi^-e^+e^-)$. The signal component has a peaking structure in this invariant mass around the mass of the B^0 meson $m_{B^0} = 5279.65 \pm 0.12\,\text{MeV}$ [69], since the relevant decay is $B^0 \to K^{*0}e^+e^-$. Most of the backgrounds end up passing the signal selection, when one or more particles of the respective decay are missed. Therefore the invariant mass $m(K^+\pi^-e^+e^-)$ does not necessarily correspond to the B^0 mass and the shape of the mass distribution differs from the signal shape. This allows a good separation of signal from the various background components through the mass fit. The angular analysis needs to know how large the background contributions are when including these components in the angular fit. Therefore, a mass fit to $B^0 \to K^{*0}e^+e^-$ candidates is performed, measuring the fractions of all components included (see Section 6.2).
The branching ratio measurement needs the number of signal candidates in $B^0 \to K^{*0}e^+e^-$ and $B^0 \to K^{*0}J/\psi\,(\to e^+e^-)$ data. The former yield can be extracted from the mass fit to $B^0 \to K^{*0}e^+e^-$ after some modifications, the latter requires and additional fit of $B^0 \to K^{*0}J/\psi\,(\to e^+e^-)$ events (see Section 6.1). This fit to the resonant mode is also used to extract possible data/MC differences, relevant to the rare mode fit.
The mass fit to the rare mode is developed as part of the official LHCb analysis [1, 2]. The author of this thesis contributed to the mass fit to the reference channel and the modifications to the mass fit to the rare mode that are relevant for the branching fraction measurement.

6.1 Mass fit in the $B^0 \to K^{*0}J/\psi\,(\to e^+e^-)$ reference channel

The mass fit to $B^0 \to K^{*0}J/\psi\,(\to e^+e^-)$ candidates serves two purposes. On the one hand the signal yield of this fit is later used as input in the branching

ratio measurement. On the other hand this fit is used to extract possible data and MC simulation differences that would distort the mass shape of the signal component.
The mass fit to $B^0 \to K^{*0} J/\psi (\to e^+e^-)$ candidates is performed as a simultaneous extended binned maximum likelihood fit in the four categories in the mass range $m(K^+\pi^-e^+e^-) \in [4700, 6200]$ MeV. The signal and background components that are present are modeled from corresponding MC simulations and are included in the mass fit.

6.1.1 Mass shapes from simulation

The signal mass shape is modeled by a Double Crystal Ball (DCB) function to properly model the tails of the distribution. A Crystal Ball (CB) function consists of a Gaussian core and a power-law function as low-end tail, below a certain threshold. It takes the mean and width of the Gaussian function as parameters as well as the power and cut-off point of the power-law function. A Double Crystal Ball function also has a power-law function for the high-end tail, above a specified threshold. The normalization of the tails is done such that the function itself and its first derivative are both continuous.
The mass shape is fixed from a fit to $B^0 \to K^{*0} J/\psi (\to e^+e^-)$ MC simulation as shown in Figure 6.1. In order to account for data and MC simulation differences a shift to the mean, $m^y_{J/\psi}$, and a scale factor to the width, $s^y_{J/\psi}$, of the DCB are introduced in the fit to data, such that the signal PDF becomes

$$\mathcal{P}^{t,y}_{J/\psi} = DCB(\mu^{t,y}_{J/\psi,\mathrm{MC}} + m^y_{J/\psi}, \sigma^{t,y}_{J/\psi,\mathrm{MC}} \cdot s^y_{J/\psi}, \alpha^{t,y}_{1,J/\psi,\mathrm{MC}}, \alpha^{t,y}_{2,J/\psi,\mathrm{MC}}, n^{t,y}_{1,J/\psi,\mathrm{MC}}, n^{t,y}_{2,\gamma,\mathrm{MC}}), \tag{6.1}$$

where the upper script $t = \{\mathrm{L0L}, \mathrm{L0I}\}$ denotes the trigger and $y = \{\text{Run 1}, \text{Run 2}\}$ the data taking period. The symbol $\mu_{J/\psi,\mathrm{MC}}$ denotes the mean, $\sigma_{J/\psi,\mathrm{MC}}$ the width and $\alpha_{J/\psi,\mathrm{MC}}$, $n_{J/\psi,\mathrm{MC}}$ the parameters of the two tails of the DCB, all fixed from the fit to the MC sample.
Background contributions from $B^0_s \to K^{*0} J/\psi (\to e^+e^-)$ decays are modeled using the same mass shape as $B^0 \to K^{*0} J/\psi (\to e^+e^-)$ decays, with the only difference that the mean of the DCB is shifted by the difference of the nominal mass of the two mesons $m_{B^0} - m_{B^0_s}$.
Background contributions from $\Lambda^0_b \to pK^- J/\psi (\to e^+e^-)$ decays are modeled from MC simulation. The fit model consists of a non-parametric RooKeysPDF [81], provided by the ROOT software package. This class implements a one-dimensional kernel estimation PDF, which models the distribution of an arbitrary input dataset as a superposition of Gaussian kernels. The mass shapes are modeled from a fit to $\Lambda^0_b \to pK^- J/\psi (\to e^+e^-)$ MC simulation that is weighted for the

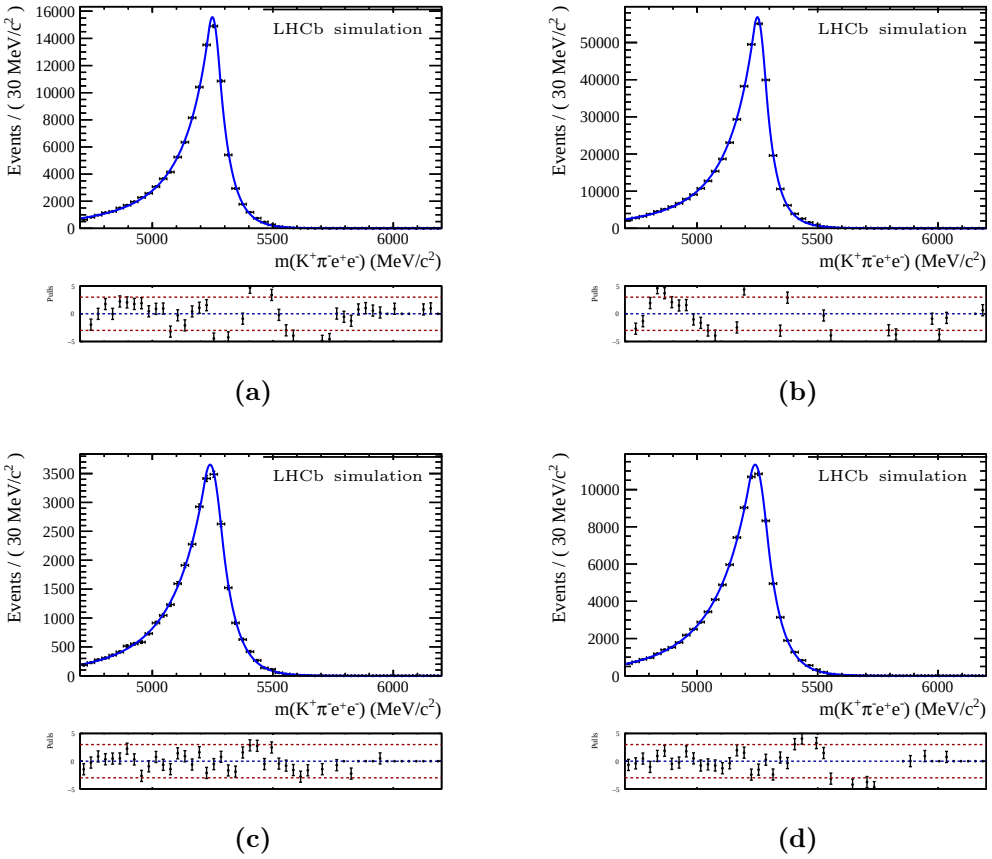

Figure 6.1: Invariant mass fits to the $B^0 \to K^{*0} J/\psi\,(\to e^+e^-)$ MC sample, in the trigger category L0L (top) and L0I (bottom), for Run 1 (left) and Run 2 (right).

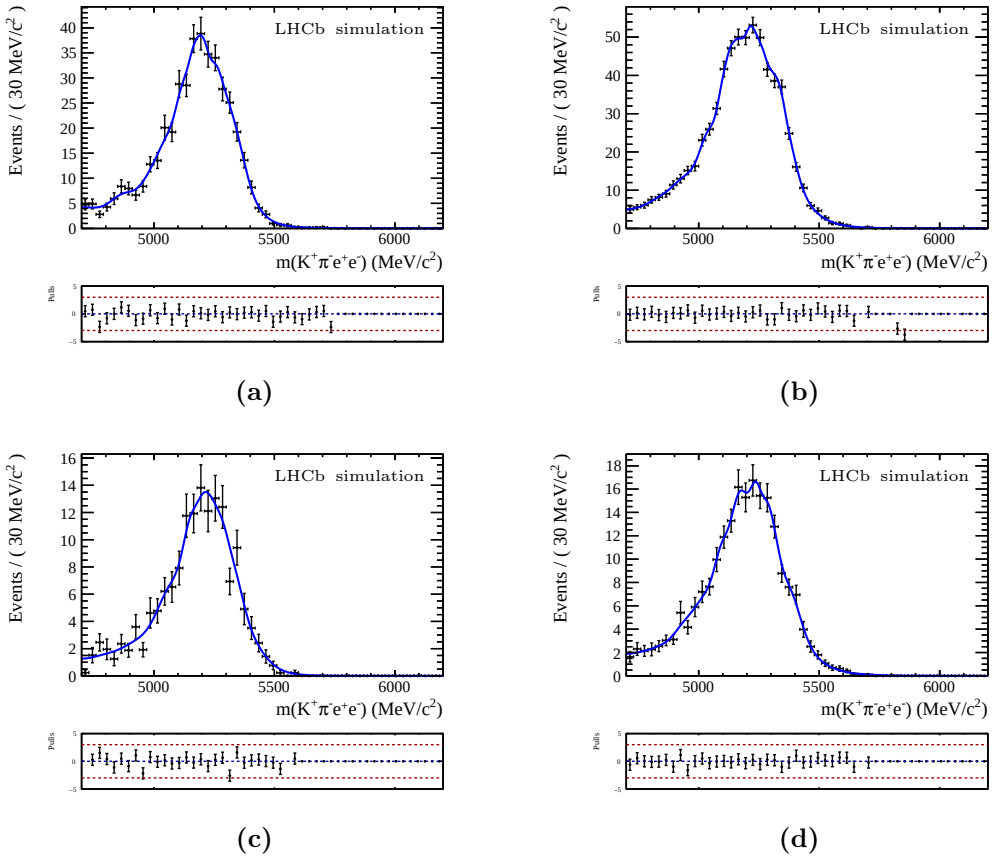

Figure 6.2: Invariant mass fits to the $\Lambda_b^0 \to pK^- J/\psi\,(\to e^+e^-)$ MC sample, in the trigger category L0L (top) and L0I (bottom), for Run 1 (left) and Run 2 (right).

pK Dalitz plot to account for all possible resonances [82]. The fits per category are shown in Figure 6.2.
Additional contributions from combinatorial background are modeled in the mass fit by an exponential function.

6.1.2 Mass fit to data

In the fit to data, the fractions of $B_s^0 \to K^{*0} J/\psi\,(\to e^+e^-)$ and $\Lambda_b^0 \to pK^- J/\psi\,(\to e^+e^-)$ decays with respect to the signal decays $B^0 \to K^{*0} J/\psi\,(\to e^+e^-)$ are fixed and given by

$$f_{B_s^0}^{y} = \frac{\mathcal{B}(B_s^0 \to K^{*0} J/\psi\,)}{\mathcal{B}(B^0 \to K^{*0} J/\psi\,)} \cdot \left(\frac{f_s}{f_d}\right)^y , \tag{6.2}$$

and

$$f_{\Lambda_b^0}^{t,y} = \frac{\mathcal{B}(\Lambda_b^0 \to pK^- J/\psi)}{\mathcal{B}(B^0 \to K^{*0} J/\psi)} \cdot \left(\frac{f_{\Lambda_b}}{f_d}\right)^y \cdot \frac{\varepsilon^{t,y}(\Lambda_b^0 \to pK^- J/\psi(\to e^+e^-))}{\varepsilon^{t,y}(B^0 \to K^{*0} J/\psi(\to e^+e^-))}, \quad (6.3)$$

where $\frac{f_s}{f_d}$ ($\frac{f_{\Lambda_b}}{f_d}$) is the B_s^0 (Λ_b^0) over B^0 hadron production fraction at LHCb [83, 84]. Since $\frac{f_{\Lambda_b}}{f_d}$ is dependent on the transverse momentum p_T, the ratio for the average p_T (estimated from the MC simulation) is taken.
As the yield of $B^0 \to K^{*0} J/\psi(\to e^+e^-)$ decays is required for the branching ratio measurement, the mass fit to data is performed as extended maximum likelihood fit and the full PDF for the reference channel is given by

$$\begin{aligned}\mathcal{P}_{tot,J/\psi}^{t,y}(N_{J/\psi}^{t,y}, m_{J/\psi}^y, s_{J/\psi}^y, \lambda^{t,y}) = {} & N_{J/\psi}^{t,y} \cdot \mathcal{P}_{J/\psi}^{t,y}(m_{J/\psi}^y, s_{J/\psi}^y) \\ & + N_{data}^{t,y} \cdot f_{B_s^0}^{t,y} \cdot \mathcal{P}_{B_s^0}^{t,y}(m_{J/\psi}^y, s_{J/\psi}^y) \\ & + N_{data}^{t,y} \cdot f_{\Lambda_b^0}^{t,y} \cdot \mathcal{P}_{\Lambda_b^0}^{t,y} \\ & + N_{comb}^{t,y} \cdot \mathcal{P}_{comb}^{t,y}(\lambda^{t,y}),\end{aligned} \quad (6.4)$$

where λ is the slope of the exponential function for the combinatorial background. Since the shift and scale factor $m_{J/\psi}$ and $s_{J/\psi}$ are found to be compatible for the two trigger categories, they are shared. To convert the fractions of the Λ_b^0 and B_s^0 background contributions into yields in the extended fit, the fixed number of $B^0 \to K^{*0} J/\psi(\to e^+e^-)$ candidates in data is used.
Figure 6.3 shows the results of the mass fit to $B^0 \to K^{*0} J/\psi(\to e^+e^-)$ data. The values of $m_{J/\psi}$ and $s_{J/\psi}$ are fixed and used as inputs to the mass fit to $B^0 \to K^{*0} e^+e^-$ candidates. The signal yields are listed in Table 6.1. They are used as inputs to the branching ratio measurement.

Table 6.1: Signal yields from the mass fit to $B^0 \to K^{*0} J/\psi(\to e^+e^-)$ data per category that are used as input to the branching fraction measurement.

category	**yield** $N_{J/\psi}$
Run 1 L0L	37313 ± 198
Run 1 L0I	9469 ± 100
Run 2 L0L	143593 ± 384
Run 2 L0I	36816 ± 210

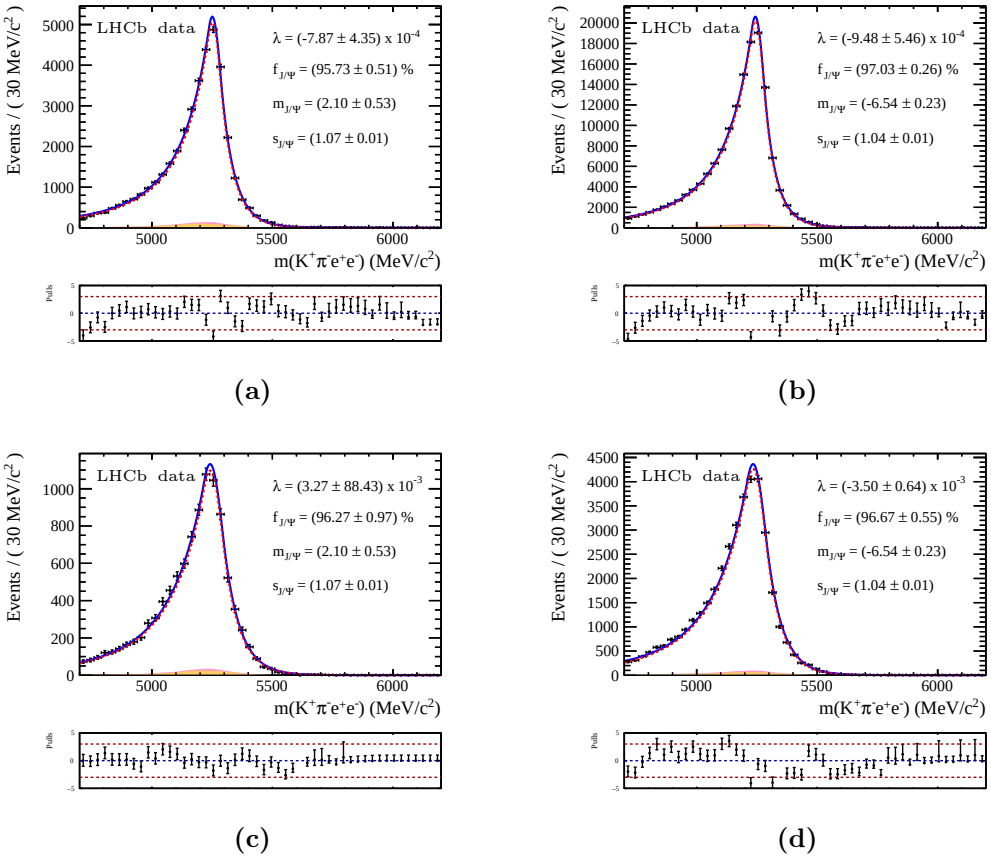

Figure 6.3: Invariant mass fits to $B^0 \to K^{*0} J/\psi (\to e^+e^-)$ data, in the trigger category L0L (top) and L0I (bottom), for Run 1 (left) and Run 2 (right). The signal is shown as red dotted line, the $B_s^0 \to K^{*0} J/\psi (\to e^+e^-)$ contribution in pink, the $\Lambda_b^0 \to pK^- J/\psi (\to e^+e^-)$ contribution in orange and combinatorial background in cyan.

6.2 Mass fit in the $B^0 \to K^{*0}e^+e^-$ signal channel

The fit to the invariant mass $m(K^+\pi^-e^+e^-)$ in $B^0 \to K^{*0}e^+e^-$ decays is an integral part of the analysis, since it allows to separate the signal from the remaining background components. In order to improve the separation capabilities of the fit, it is performed simultaneous to the signal and control channel, the two data taking periods and the two trigger categories. This brings the total up to eight categories:

very-low q^2-bin & gamma q^2-bin (see Section 4.3)

$\times$ Run 1 & Run 2 (see Section 4.1)

$\times$ L0L & L0I (see Section 5.1)

A wide mass range of $m(K^+\pi^-e^+e^-) \in [4500, 6200]$ MeV is chosen, so that radiative tails and the partially reconstructed background can be modeled properly.
In the angular analysis the mass fit is used to determine the fractions associated to each background component so that they can be constrained in the angular fit, where the separation between signal and background components is more difficult.
In the branching ratio measurement the mass fit is extended so that the signal yield of $B^0 \to K^{*0}e^+e^-$ decays can be extracted.

6.2.1 Mass shapes from simulation

The mass shapes of signal and specific background components that are included in the mass fit are determined from fits to corresponding simulated events. These simulation samples are corrected for data/MC simulation differences by applying the weights discussed in Section 5.2.

Signal component

The signal component in the gamma q^2-bin is given by the decay $B^0 \to K^{*0}\gamma(\to e^+e^-)$ and the decay $B^0 \to K^{*0}e^+e^-$ in the very-low q^2-bin. Both decays have very similar physics and give rise to the same mass shape. They are therefore both modeled with the same PDF. This PDF is a Double Crystal Ball (DCB) function to properly model the tails of the distribution that are due to bremsstrahlung loss and recovery.
The fits to $B^0 \to K^{*0}\gamma(\to e^+e^-)$ MC simulation are shown in Figure 6.4 and the fits to $B^0 \to K^{*0}e^+e^-$ MC simulation are shown in Figure 6.5.

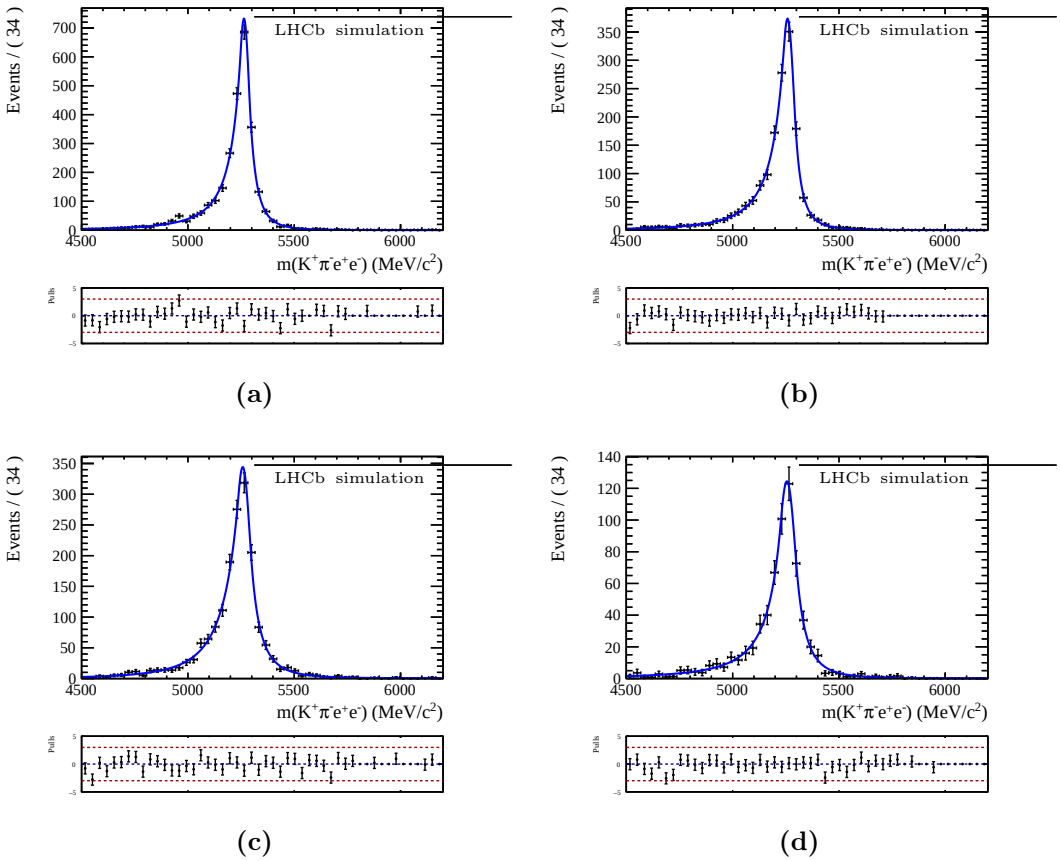

Figure 6.4: Invariant mass fits to the $B^0 \to K^{*0}\gamma(\to e^+e^-)$ MC sample in the gamma q^2-bin, in the trigger category L0L (top) and L0I (bottom), for Run 1 (left) and Run 2 (right).

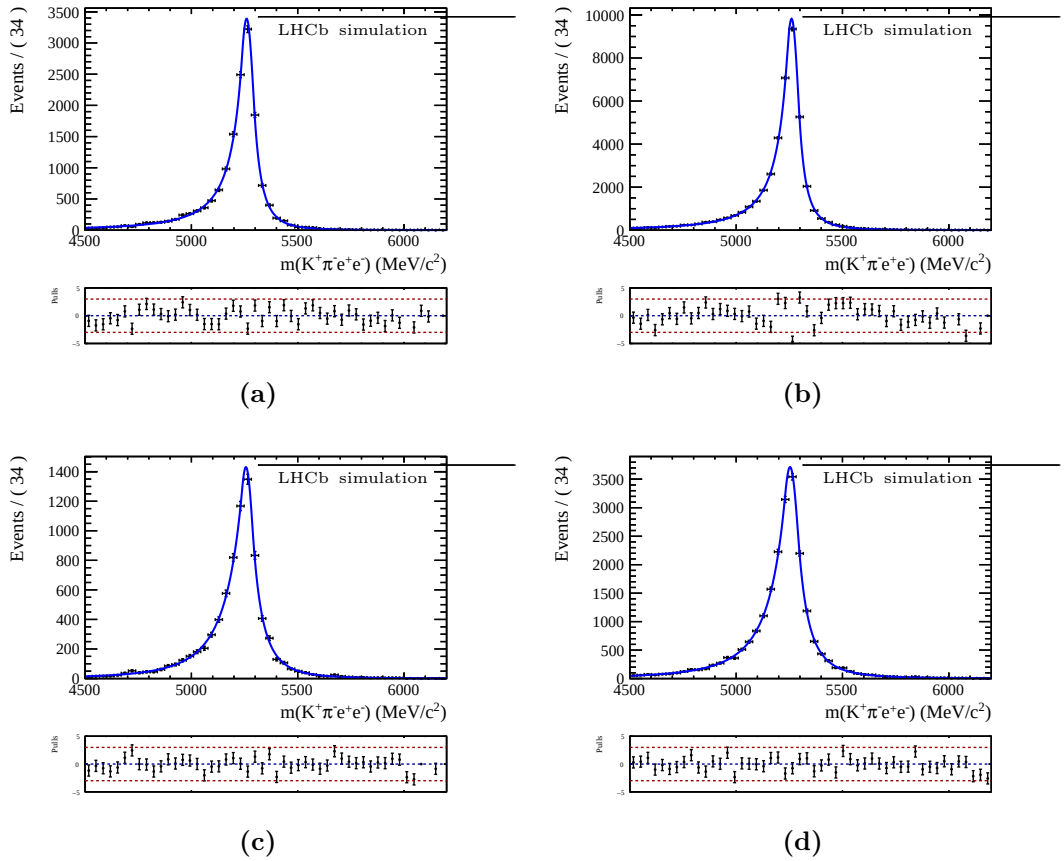

Figure 6.5: Invariant mass fits to the $B^0 \to K^{*0}e^+e^-$ MC sample in the very-low q^2-bin, in the trigger category L0L (top) and L0I (bottom), for Run 1 (left) and Run 2 (right).

Partially reconstructed background

Partially reconstructed background contributions arise from $B \to K^{*0}\pi e^+e^-$ decays, where one of the pions is not reconstructed. Therefore, the invariant mass $m(K^+\pi^-e^+e^-)$ does not peak at m_{B^0}. Rather, $m(K^+\pi^-e^+e^-)$ has a peaking structure a little above 5000 MeV, corresponding roughly to the mass of the B meson minus the mass of the missed pion. In addition the shape has a large tail to lower masses, where the missed pion was more energetic. A very small tail towards larger masses can be explained by the bremsstrahlung recovery.
In the range $0 < m_{ee}^{B^0} < 500\,\text{MeV}$, this background mostly consists of $B^+ \to K_1(1270)(\to K^+\pi^-X)e^+e^-$ decays for which simulated events are available to determine the mass shape. The PDF model is the sum of a CB function and a Gaussian function. The fits to $B^+ \to K_1(1270)(\to K^+\pi^-X)e^+e^-$ MC simulation are shown in Figure 6.6 and 6.7 in the gamma and very-low q^2-bin for each trigger category, respectively.

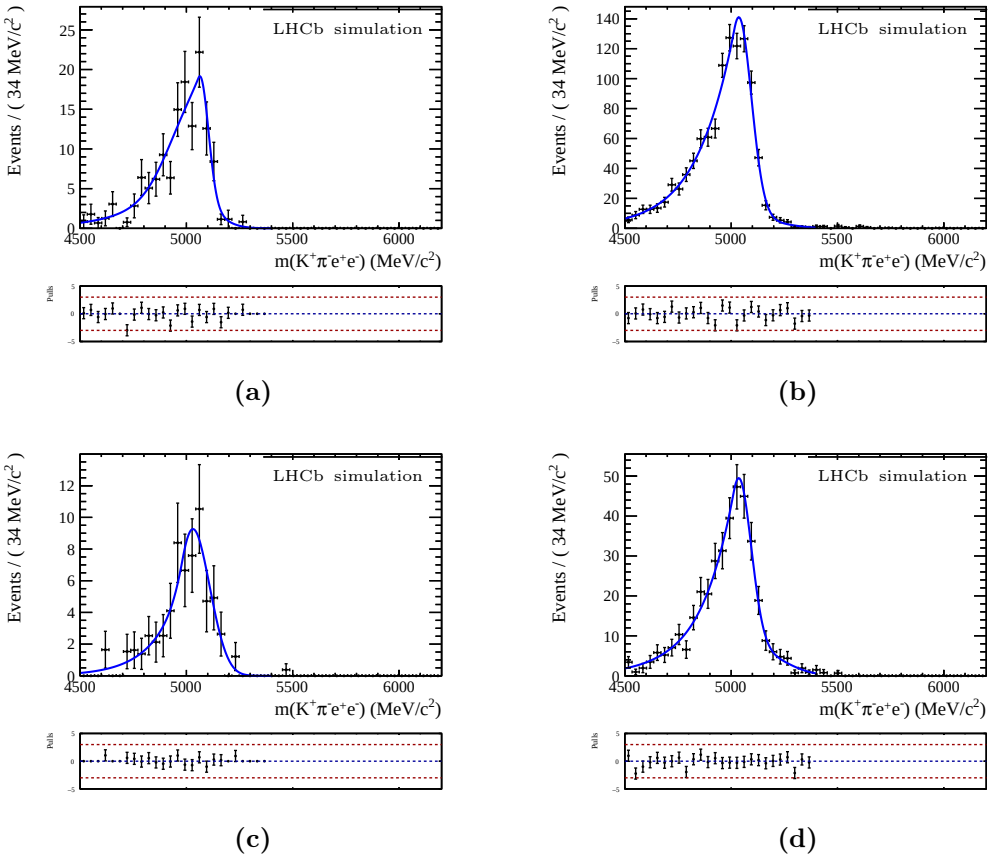

Figure 6.6: Invariant mass fits to the $B^+ \to K_1(1270)(\to K^+\pi^- X)e^+e^-$ MC sample in the gamma q^2-bin, in the trigger category L0L (top) and L0I (bottom), for Run 1 (left) and Run 2 (right).

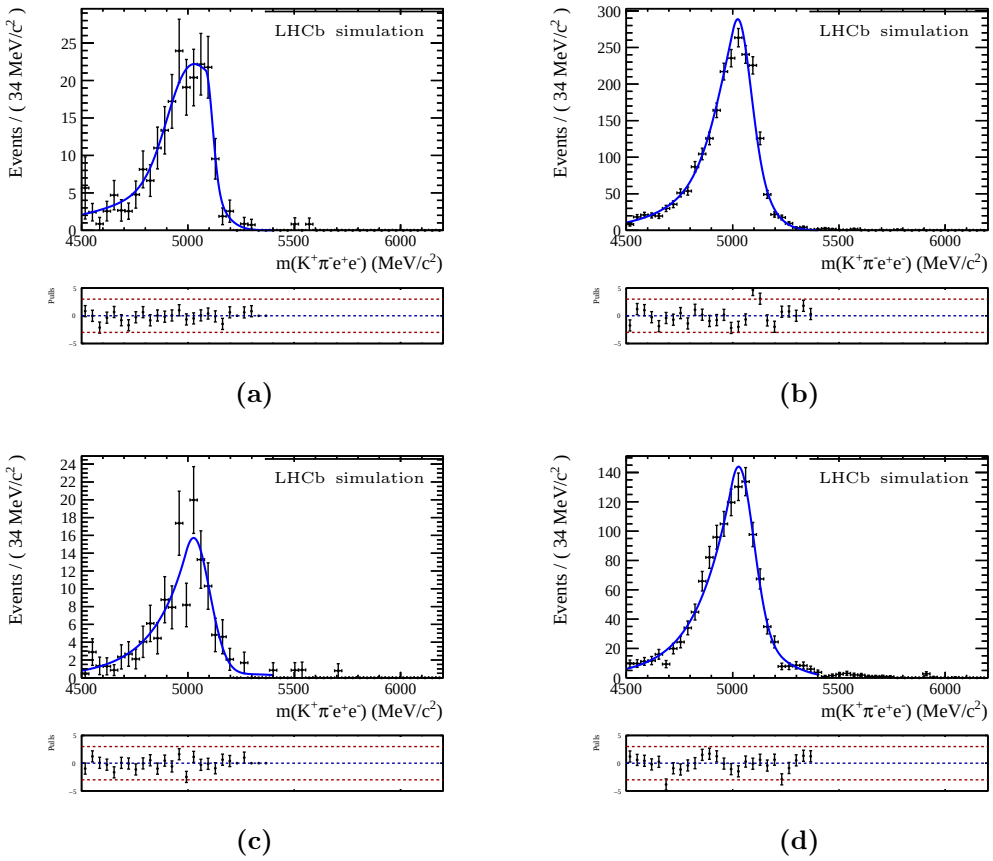

Figure 6.7: Invariant mass fits to the $B^+ \to K_1(1270)(\to K^+\pi^- X)e^+e^-$ MC sample in the very-low q^2-bin, in the trigger category L0L (top) and L0I (bottom), for Run 1 (left) and Run 2 (right).

$B^0 \to K^{*0}\pi^0/\eta$ background contributions

The background contributions from $B^0 \to K^{*0}\pi^0/\eta$ decays with either the π^0 or η meson differ in their subsequent decay chain for the q^2-bins.
In the gamma q^2-bin the pseudoscalars mostly decay to two photons, where one photon converts to two electrons. The respective decays are $B^0 \to K^{*0}\pi^0(\to \gamma(\to e^+e^-)\gamma)$ and $B^0 \to K^{*0}\eta(\to \gamma(\to e^+e^-)\gamma)$. Due to limited statistics in the available simulation files, all categories are merged together for the fits to MC simulation. The fit model consists of a non-parametric RooKeysPDF function. The fits to $B^0 \to K^{*0}\pi^0(\to \gamma(\to e^+e^-)\gamma)$ and $B^0 \to K^{*0}\eta(\to \gamma(\to e^+e^-)\gamma)$ are shown in Figure 6.8.
In the very-low q^2-bin the relevant decay of the pseudoscalars is the so called Dalitz decay, where the meson decays into two electrons and a photon. The respective decays are $B^0 \to K^{*0}\pi^0(\to \gamma e^+e^-)$ and $B^0 \to K^{*0}\eta(\to \gamma e^+e^-)$. Again, a RooKeysPDF is used to model the distributions. Simulation files for all years are available, therefore the components are modeled in the four trigger categories and runs. The fits to $B^0 \to K^{*0}\pi^0(\to \gamma e^+e^-)$ and $B^0 \to K^{*0}\eta(\to \gamma(\to e^+e^-)\gamma)$ are shown in Figure 6.9 and 6.10, respectively.

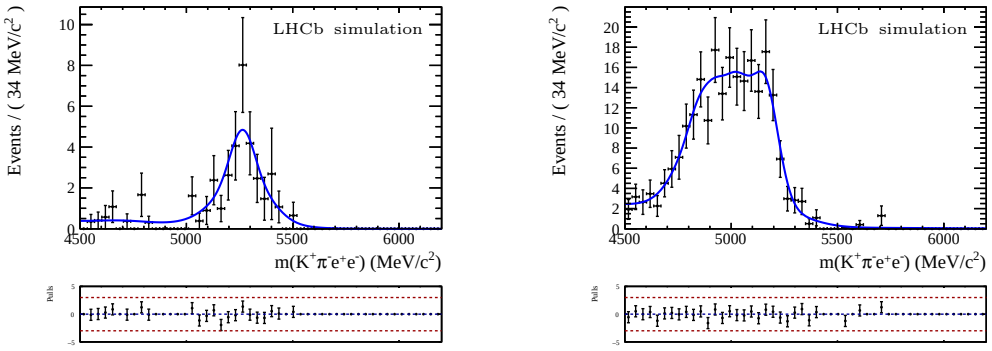

(a) **(b)**

Figure 6.8: Invariant mass fits to the $B^0 \to K^{*0}\pi^0(\to \gamma(\to e^+e^-)\gamma)$ MC sample (left) and the $B^0 \to K^{*0}\eta(\to \gamma(\to e^+e^-)\gamma)$ MC sample (right) in the gamma q^2-bin. Due to the limited available statistics this fit is merged for all categories.

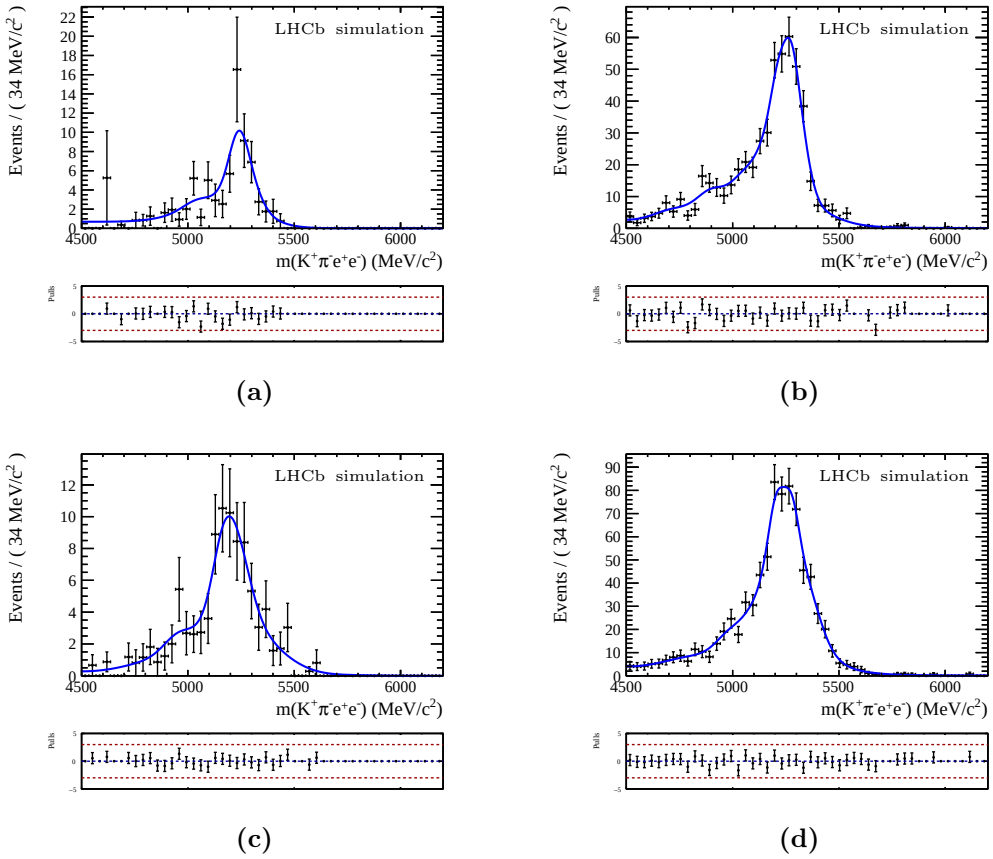

Figure 6.9: Invariant mass fits to the $B^0 \to K^{*0}\pi^0(\to \gamma e^+e^-)$ MC sample in the very-low q^2-bin, in the trigger category L0L (top) and L0I (bottom), for Run 1 (left) and Run 2 (right).

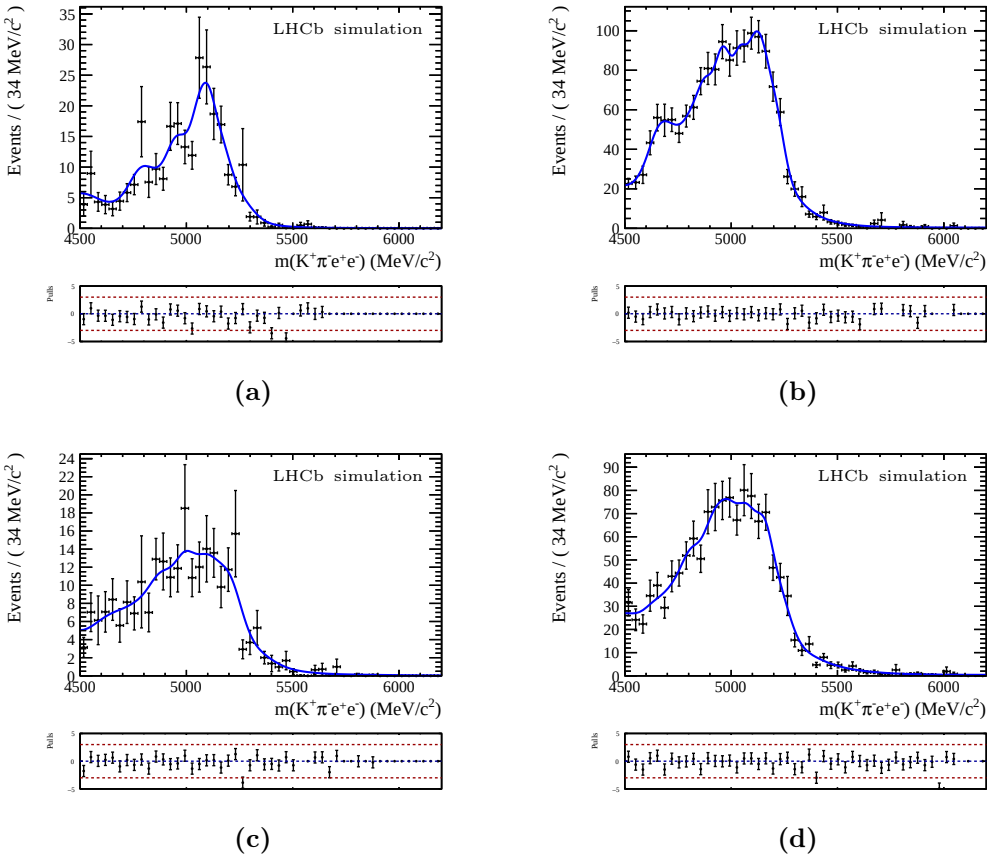

Figure 6.10: Invariant mass fits to the $B^0 \to K^{*0}\pi^0(\to \gamma e^+e^-)$ MC sample in the very-low q^2-bin, in the trigger category L0L (top) and L0I (bottom), for Run 1 (left) and Run 2 (right).

6.2.2 Mass fit to $B^0 \to K^{*0} e^+ e^-$ data

To model the invariant mass shape of $B^0 \to K^{*0} e^+ e^-$ data one has to construct a model that contains all background shapes. The fractions of contamination of each background component are the free fit parameters, since the shapes are fixed from fits to MC simulation as explained in the previous Section 6.2.1. Starting values for the fractions can be estimated using the efficiencies for the respective decays and measured values of the branching fractions from the PDG [69].
In the following, the full PDF for the mass fit to $B^0 \to K^{*0} e^+ e^-$ data will be constructed. The fit is performed simultaneously in eight categories. The two data taking periods, denoted in the following as $y = \{\text{Run 1}, \text{Run 2}\}$, the trigger categories $t = \{\text{L0L}, \text{L0I}\}$ and the gamma and very-low q^2-bin, denoted as $q = \{g, l\}$.
To account for possible data/MC differences the mean of the signal double crystal ball PDF is shifted by a value $m^y_{J/\psi}$ and the width is scaled by a factor $s^y_{J/\psi}$, which were extracted from the fit to the $B^0 \to K^{*0} J/\psi\,(\to e^+ e^-)$ reference channel (see Section 6.1).
The decays $B^0 \to K^{*0} e^+ e^-$ and $B^0 \to K^{*0}\gamma(\to e^+ e^-)$ result in the same mass shape. Therefore a mass fit in the very-low q^2-bin alone is not able to separate these two components. This means that the signal yield extracted from a fit would not only contain $B^0 \to K^{*0} e^+ e^-$ candidates but also a contribution from $B^0 \to K^{*0}\gamma(\to e^+ e^-)$ candidates. A solution to this problem is the inclusion of the gamma q^2-bin to the fit. In the gamma q^2-bin the signal yield is dominated by $B^0 \to K^{*0}\gamma(\to e^+ e^-)$ candidates with a small contribution of $B^0 \to K^{*0} e^+ e^-$ candidates. One can then use the ratio of candidates in the different q^2-bins estimated from MC simulation to constrain the leakage of candidates in the other q^2-bin.
Another reason to include the gamma q^2-bin in the fit is the similarity of background components in both q^2 regions and the larger statistics in the control channel. The underlying physics is similar between a real and a quasi real virtual photon. Therefore, the fraction of partially reconstructed background, for example, is expected to be the same in both q^2-bins, allowing this parameter to be shared among the q^2-bins. Since the gamma q^2-bin comprises a larger dataset it allows for a better determination of this parameter. By simultaneously fitting the gamma q^2-bin one can therefore improve the sensitivity in the very-low q^2-bin as well.
The following part defines the PDF for each component:

- Signal and leakage PDFs: $B^0 \to K^{*0}\gamma(\to e^+ e^-)$ and $B^0 \to K^{*0} e^+ e^-$

contributions, defined by

$$\mathcal{P}_s^{y,t,q} = DCB(\mu_{s,\mathrm{MC}}^{y,t,q} + m_{J/\psi}^{y}, \sigma_{s,\mathrm{MC}}^{y,t,q} \cdot s_{J/\psi}^{y}, \alpha_{1,s,\mathrm{MC}}^{y,t,q}, \alpha_{2,s,\mathrm{MC}}^{y,t,q}, n_{1,s,\mathrm{MC}}^{y,t,q}, n_{2,s,\mathrm{MC}}^{y,t,q}). \tag{6.5}$$

The fraction $f_s^{y,t,q}$ associated to this PDF is defined as the sum of the fractions of $B^0 \to K^{*0}\gamma(\to e^+e^-)$ and $B^0 \to K^{*0}e^+e^-$ candidates as

$$f_s^{y,t,q} = f_\gamma^{y,t,q} + f_{ee}^{y,t,q}. \tag{6.6}$$

The leakage of $B^0 \to K^{*0}e^+e^-$ candidates in the gamma q^2-bin is constrained by the MC simulation such that the fraction of the leakage is defined by

$$f_{ee}^{y,t,g} = \mathcal{G}_{ee}^{y,t} \left(\frac{N_{ee,\mathrm{MC}}^{y,t,g}}{N_{ee,\mathrm{MC}}^{y,t,l}} \right) \frac{N_{\mathrm{data}}^{y,t,l}}{N_{\mathrm{data}}^{y,t,g}} f_{ee}^{y,t,l}, \tag{6.7}$$

where $f_{ee}^{y,t,q}$ is the $B^0 \to K^{*0}e^+e^-$ fraction returned by the fit in each category, while $N_{\mathrm{data}}^{y,t,q}$ is the yield of data in each category. $\mathcal{G}$ is a Gaussian constraint parameterized by the ratio of yields extracted from the simulation. Similarly, the leakage from $B^0 \to K^{*0}\gamma(\to e^+e^-)$ candidates in the very-low q^2-bin is given by

$$f_\gamma^{y,t,l} = \mathcal{G}_\gamma^{y,t} \left(\frac{N_{\gamma,\mathrm{MC}}^{y,t,l}}{N_{\gamma,\mathrm{MC}}^{y,t,g}} \right) \frac{N_{\mathrm{data}}^{y,t,g}}{N_{\mathrm{data}}^{y,t,l}} f_\gamma^{y,t,g}. \tag{6.8}$$

- Partially reconstructed background PDF: defined by

$$\begin{aligned} \mathcal{P}_{PR}^{y,t,q} = {} & f_{CB}^{y,t,q} \cdot CB(\mu_{PR,\mathrm{MC}}^{y,t,q}, \sigma_{PR,\mathrm{MC}}^{y,t,q}, \alpha_{PR,\mathrm{MC}}^{y,t,q}, n_{PR,\mathrm{MC}}^{y,t,q}) \\ & + (1 - f_{CB}^{y,t,q}) \cdot Gauss(\tilde{\mu}_{PR,\mathrm{MC}}^{y,t,q}, \tilde{\sigma}_{PR,\mathrm{MC}}^{y,t,q}), \end{aligned} \tag{6.9}$$

where the fraction $f_{CB}^{y,t,q}$ is used to asses the contribution of the CB and Gaussian function.
The fraction of partially reconstructed background with respect to the signal (including leakage) is shared between the two q^2-bins, imposing the additional constraint

$$f_{PR}^{y,t,q} = C_{PR}^{y,t} \cdot f_s^{y,t,q}, \tag{6.10}$$

where $C_{PR}^{y,t}$ is a free parameter shared among the two q^2-bins.

- π^0/η background PDFs: defined by

$$\mathcal{P}_i^{y,t,q} \quad , \; i = \{\pi^0, \eta\}, \tag{6.11}$$

which are the non parametric shapes obtained from the fits to the corresponding MC simulations. The fractions of π^0/η backgrounds are Gaussian constrained from the yields in MC simulation such that

$$\begin{cases} f_i^{y,t,g} = \mathcal{G}_i^{y,t,g} \left(\frac{N_{i,\mathrm{MC}}^{y,t,g}}{N_{\gamma,\mathrm{MC}}^{y,t,g}} \right) f_\gamma^{y,t,g} \\ f_i^{y,t,l} = \mathcal{G}_i^{y,t,l} \left(\frac{N_{i,\mathrm{MC}}^{y,t,l}}{N_{ee,\mathrm{MC}}^{y,t,l}} \right) f_{ee}^{y,t,l} \end{cases} , \; i = \{\pi^0, \eta\}. \tag{6.12}$$

- Combinatorial background PDF: defined by

$$\mathcal{P}_{comb}^{y,t,q} = \exp(\lambda^{y,t,q}). \tag{6.13}$$

This PDF is left free in the fit, as the combinatorial background contribution is not fixed by a fit to simulation.

In summary, the total PDF is given by

$$\begin{aligned} \mathcal{P}_{tot}^{y,t,q}(f_s^{y,t,q}, C_{PR}^{y,t}, \lambda^{y,t,q}, \mathcal{G}_{ee}^{y,t}, \mathcal{G}_\gamma^{y,t}, \mathcal{G}_\eta^{y,t,q}, \mathcal{G}_{\pi^0}^{y,t,q}) = \\ = \sum_y \sum_t \sum_q f_{ee}^{y,t,q}(f_s^{y,t,q}, \mathcal{G}_{ee}^{y,t}) \cdot \mathcal{P}_s^{y,t,q} \\ + f_\gamma^{y,t,q}(f_s^{y,t,q}, \mathcal{G}_\gamma^{y,t}) \cdot \mathcal{P}_s^{y,t,q} \\ + f_{PR}^{y,t,q}(C_{PR}^{y,t}, f_s^{y,t,q}) \cdot \mathcal{P}_{PR}^{y,t,q} \\ + f_\eta^{y,t,q}(\mathcal{G}_\eta^{y,t,q}) \cdot \mathcal{P}_\eta^{y,t,q} \\ + f_{\pi^0}^{y,t,q}(\mathcal{G}_{\pi^0}^{y,t,q}) \cdot \mathcal{P}_{\pi^0}^{y,t,q} \\ + (1 - f_s^{y,t,q} - f_{PR}^{y,t,q} - f_\eta^{y,t,q} - f_{\pi^0}^{y,t,q}) \cdot \mathcal{P}_{comb}^{y,t,q}\left(\lambda^{y,t,q}\right). \end{aligned} \tag{6.14}$$

As it is a simultaneous fit, the individual components are summed over the eight categories. The only free parameters are the signal plus leakage fractions $f_s^{y,t,g}$, the partially reconstructed fraction relative to the signal plus leakage shared between the two q^2-bins, $C_{PR}^{y,t}$, the slopes of the exponential of the combinatorial background, $\lambda^{y,t,q}$, and the Gaussian constraints on the $B^0 \to K^{*0}e^+e^-/B^0 \to K^{*0}\gamma(\to e^+e^-)$ leakages as well as the Gaussian constraints on the η/π^0 contaminations. The fraction of combinatorial background is not a free parameter and expressed through all other fractions to ensure proper normalization of the PDF.
This version of the PDF is used in the angular analysis, since the free parameters are the fractions of background contributions, which are also relevant

in the three angular dimensions to separate signal from background contributions. A simultaneous unbinned maximum likelihood fit in the eight categories in the mass range $m(K^+\pi^-e^+e^-) \in [4500, 6200]$ is performed to extract the corresponding background fractions. The fits to data are shown in Figure 6.12 and 6.11 for the gamma and very-low q^2-bin, respectively. The resulting fractions of background components are shown in Table 6.2 and 6.3.

Table 6.2: Summary of the fractions associated to each fit component in the gamma q^2-bin obtained from the invariant mass fit. The uncertainties are statistical only.

Fraction [%]	Run 1		Run 2	
	L0L	L0I	L0L	L0I
f_{ee}	5.4 ± 0.5	4.2 ± 0.6	6.3 ± 0.2	3.6 ± 0.3
f_{γ}	66.4 ± 2.4	59.2 ± 3.0	66.1 ± 1.6	57.1 ± 2.0
f_{PR}	5.5 ± 1.2	11.0 ± 2.0	5.6 ± 1.2	10.5 ± 1.9
f_{η}	3.9 ± 0.5	3.4 ± 0.5	4.7 ± 0.6	4.3 ± 0.5
f_{π^0}	3.9 ± 1.4	4.0 ± 1.2	5.4 ± 1.2	4.5 ± 1.1
f_{comb}	14.9 ± 2.4	18.2 ± 3.4	11.9 ± 1.3	20.0 ± 2.1
N_{data}	703	463	2556	1366

Table 6.3: Summary of the fractions associated to each fit component in the very-low q^2-bin obtained from the invariant mass fit. The uncertainties are statistical only.

Fraction [%]	Run 1		Run 2	
	L0L	L0I	L0L	L0I
f_{ee}	69.6 ± 6.0	56.2 ± 7.8	74.3 ± 2.8	53.8 ± 4.3
f_{γ}	1.7 ± 0.5	1.3 ± 0.4	0.9 ± 0.4	0.7 ± 0.3
f_{PR}	5.5 ± 1.3	10.0 ± 2.2	5.8 ± 1.2	9.5 ± 1.8
f_{η}	4.6 ± 0.6	5.3 ± 0.9	5.3 ± 0.5	6.1 ± 0.7
f_{π^0}	1.0 ± 0.2	1.9 ± 0.5	1.0 ± 0.2	2.1 ± 0.4
f_{comb}	17.6 ± 6.9	25.2 ± 10.0	12.7 ± 3.1	27.8 ± 5.6
N_{data}	88	66	413	241

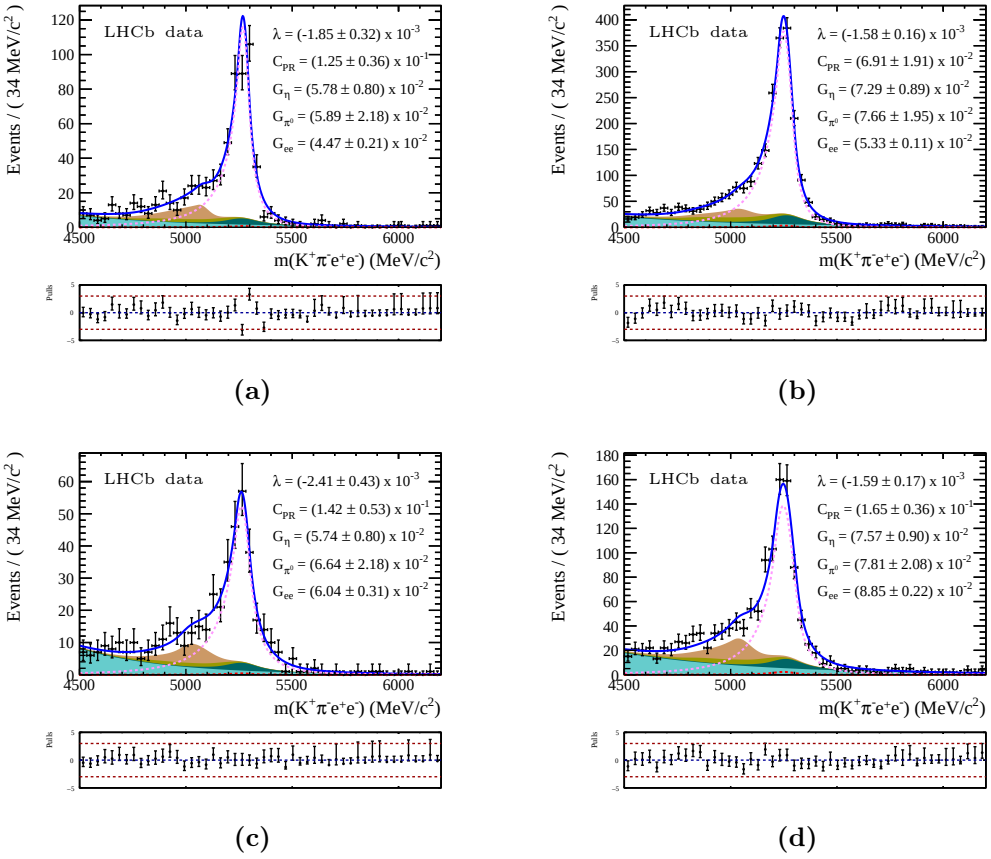

Figure 6.11: Invariant mass fits to $B^0 \to K^{*0}e^+e^-$ data in the gamma q^2-bin, in the trigger category L0L (top) and L0I (bottom), for Run 1 (left) and Run 2 (right). The signal $B^0 \to K^{*0}\gamma(\to e^+e^-)$ component is shown as pink dotted line, while the leakage of $B^0 \to K^{*0}e^+e^-$ decays is shown as red dotted line. The $B^0 \to K^{*0}\pi^0(\to \gamma(\to e^+e^-)\gamma)$ contribution is depicted in dark green, the $B^0 \to K^{*0}\eta(\to \gamma(\to e^+e^-)\gamma)$ contribution in light green, the partially reconstructed background in brown and combinatorial background in cyan.

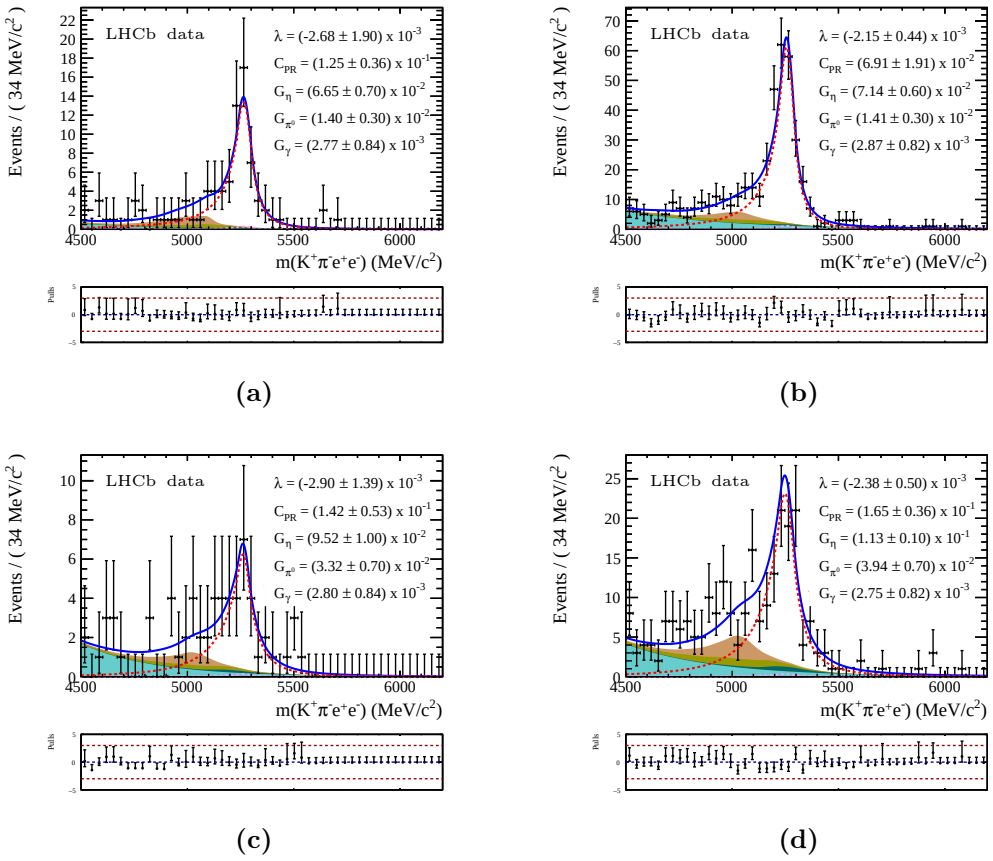

Figure 6.12: Invariant mass fits to $B^0 \to K^{*0}e^+e^-$ data in the very-low q^2-bin, in the trigger category L0L (top) and L0I (bottom), for Run 1 (left) and Run 2 (right). The signal $B^0 \to K^{*0}e^+e^-$ component is shown as red dotted line, while the leakage of $B^0 \to K^{*0}\gamma(\to e^+e^-)$ decays is shown as pink dotted line. The $B^0 \to K^{*0}\pi^0(\to \gamma e^+e^-)$ contribution is depicted in dark green, the $B^0 \to K^{*0}\eta(\to \gamma e^+e^-)$ contribution in light green, the partially reconstructed background in brown and combinatorial background in cyan.

6.3 Branching ratio measurement

In order to measure a branching fraction one has to count the number of candidates of the relevant decay and the total number of mother particles produced. The latter measurement is hard to do at LHCb and can be circumvented with the use of a reference channel. One measures a ratio of branching fractions in which the total number of produced mother particles cancels out and only the yields of the signal and reference channel as well as their efficiencies are needed for the measurement. Additionally systematic uncertainties common to both decays cancel in the ratio, allowing a higher precision in the measurement.
With the dataset selected for the angular analysis of $B^0 \to K^{*0}e^+e^-$ decays it is possible to also measure the ratio of branching fractions

$$R(\mathcal{B}) = \frac{\mathcal{B}(B^0 \to K^{*0}e^+e^-)}{\mathcal{B}(B^0 \to K^{*0}J/\psi\,(\to e^+e^-))} = \frac{N_{ee}}{N_{J/\psi}} \times \frac{\epsilon_{J/\psi}}{\epsilon_{ee}}, \tag{6.15}$$

where $N_{ee}(N_{J/\psi})$ is the number of candidates of $B^0 \to K^{*0}e^+e^-$ and $B^0 \to K^{*0}J/\psi\,(\to e^+e^-)$ decays in data, respectively and ϵ_i the efficiency with which the respective decay is reconstructed. The calculation of the efficiencies is described in Section 5.4. The reference channel yield is extracted from the mass fit to $B^0 \to K^{*0}J/\psi\,(\to e^+e^-)$ data, as described in Section 6.1. The signal channel yield can be extracted from the mass fit to $B^0 \to K^{*0}e^+e^-$ data after some modifications.

6.3.1 Modifications to the mass fit

In the angular analysis only the fraction of components in the mass fit is relevant, meaning the PDF is normalized to 1 and the overall number of events is not a fit parameter. For the branching ratio measurement one is interested in the signal yield itself. The overall number of events in data now contains valuable information as well and the likelihood function has to be extended, as described in Section 4.4.
To perform the extended maximum likelihood fit, the fit PDF has to be modified to comprise the additional fit parameter. One can either multiply the PDF by an overall number of events or one can reinterpret the fractions associated to each component as yields (by multiplying them with the fixed number of events in data). In the latter approach the additional fit parameter is introduced as the yield of combinatorial background which is no longer constrained by the other background components.
This change can be done for the mass fit to $B^0 \to K^{*0}e^+e^-$ data resulting in the yields of the signal. But as explained in Section 5.4, the efficiencies and

the yields itself differ in the trigger categories and data taking periods. So instead of one branching ratio one would compute a value for the branching ratio $R(\mathcal{B})$ measured in each of the four categories. These measurements would then have to be statistically combined in order to produce one final result. Since the proper statistical combination is not straight forward it is rather preferable to directly fit the branching ratio simultaneously in all categories.
This can be achieved by rewriting the fraction of $B^0 \to K^{*0} e^+ e^-$ candidates $f_{ee}^{y,t,l}$ in terms of the branching ratio $R(\mathcal{B})$ as well as the yield of $B^0 \to K^{*0} J/\psi (\to e^+ e^-)$ decays, $N_{J/\psi}^{y,t}$, and the respective efficiencies $\epsilon_{J/\psi}^{y,t}$ and $\epsilon_{ee}^{y,t}$

$$f_{ee}^{y,t,l} = \frac{N_{J/\psi}^{y,t}}{N_{\text{data}}^{y,t,l}} \times \frac{\epsilon_{ee}^{y,t}}{\epsilon_{J/\psi}^{y,t}} \times R(\mathcal{B}). \tag{6.16}$$

Here, the number of events in data $N_{\text{data}}^{y,t,l}$ is used to keep $f_{ee}^{y,t,l}$ a fraction. This is necessary in order to keep the definition of the constraint on the leakage fraction between the gamma and very-low q^2-bins (see Equations 6.7 and 6.8). The yield of $B^0 \to K^{*0} J/\psi (\to e^+ e^-)$ decays as well as the efficiencies are Gaussian constrained to their input values.
With that, one can rewrite the fit PDF of Equation 6.14 to accommodate the branching ratio measurement:

- The fractions associated to each PDF component are multiplied by the fixed number of events in data,
- the yield associated to the combinatorial background is an independent fit parameter and not constrained by other background contributions,
- the signal plus leakage fractions are replaced as free fit parameters by the branching ratio $R(\mathcal{B})$, which is shared between the four categories in the very-low q^2-bin (see Equation 6.16).

A simultaneous extended unbinned maximum likelihood fit in the eight categories in the mass range $m(K^+\pi^- e^+ e^-) \in [4500, 6200]$ MeV is performed on $B^0 \to K^{*0} e^+ e^-$ data to extract the branching ratio. The yields of the reference channel (see Table 6.1) and the efficiencies of the signal and reference channel (see Table 5.2) are Gaussian constraint to their input values.

7 Angular fits

7.1 Angular fit strategy

The aim of the angular analysis is to measure the four observables F_{L}, $A_T^{(2)}$, A_T^{Re} and A_T^{Im} on $B^0 \to K^{*0} e^+ e^-$ signal candidates by performing a four dimensional fit to the differential decay width (see Equation 2.9) in the three angles $\cos\theta_\ell$, $\cos\theta_K$ and $\tilde{\phi}$ and the $m(K^+\pi^- e^+ e^-)$ invariant mass. The fit is performed simultaneously in the two trigger categories and the two data taking periods, with shared parameters F_{L}, $A_T^{(2)}$, A_T^{Re} and A_T^{Im}.
As described in Section 6.2, the invariant mass fit is performed in a wide mass window $m(K^+\pi^- e^+ e^-) \in [4500, 6200]\,\mathrm{MeV}$ and the fractions associated to each fit component are determined. Since the angular distributions alone do not provide a good separation between the signal and background shapes, the invariant mass distribution is included again in the four dimensional fit. However, in order to reduce the background contamination and ease the angular modeling of backgrounds, the mass window is reduced for the angular fit to a narrow range of $m(K^+\pi^- e^+ e^-) \in [5000, 5400]\,\mathrm{MeV}$.
The reconstruction and selection of signal candidates introduces a distortion of the angular distributions. This is taken into account by an angular acceptance PDF, which is determined and discussed in Section 7.2.
Due to the non-negligible background contamination, the angular distributions of the present background components have to be modeled as well and have to be included in the total fit PDF, which is discussed in Section 7.3. The fraction associated to each component is Gaussian constrained from the mass fit in the wide range.
The angular fit strategy is developed and studied as part of the official LHCb analysis [1, 2]. The author of this thesis contributed to the angular modeling of background components and the angular fit to data.

7.2 Angular acceptance

The angular acceptance PDF describes the distortion to the angular distribution of $B^0 \to K^{*0} e^+ e^-$ candidates that is introduced due to the detector geometry and reconstruction and selection of the candidates. Since there are

year and trigger dependent differences in the selection process the angular acceptance has to be modeled for each trigger category and data taking period. These distortion effects are studied using a so-called phase-space MC sample of $B^0 \to K^{*0} e^+ e^-$ simulated events. The phase-space MC sample is generated without underlying physics except momentum conservation. In consequence the three angles $\cos\theta_\ell$, $\cos\theta_K$ and $\tilde{\phi}$ are generated with flat uncorrelated distributions. Applying the full reconstruction algorithm and candidate selection to the phase-space MC sample, distorts the flat distributions. These distorted distributions are taken as angular acceptance for each angle and can later be used to cancel the acceptance effects in the measured distributions.
The phase-space MC sample is also generated with a flat q^2 distribution, resulting in a dramatically different dielectron mass distribution than with SM physics. Even though the q^2 range of the analysis is very narrow, the angular acceptance is expected to have some correlation with the dielectron mass, especially the angle $\cos\theta_\ell$, which directly involves the two leptons. This problem is solved by a weighting procedure to match the physical dielectron mass distribution (see Ref. [2]).

7.2.1 Acceptance fit

The angular acceptance of each of the three angles $\cos\theta_\ell$, $\cos\theta_K$ and $\tilde{\phi}$ is extracted by an unbinned maximum likelihood fit to the phase-space MC sample of $B^0 \to K^{*0} e^+ e^-$ decays after applying the full reconstruction and selection. The corrections to MC simulation, discussed in Section 5.2, are also applied. The acceptance fits are performed separately in the two trigger categories and the two data taking periods. It is assumed that the angular acceptance factorizes in the three angles according to

$$\varepsilon_{\mathcal{A}}^{t,y}\left(\cos\theta_\ell, \cos\theta_K, \tilde{\phi}\right) \equiv \varepsilon_{\mathcal{A}}^{t,y}\left(\cos\theta_\ell\right) \cdot \varepsilon_{\mathcal{A}}^{t,y}\left(\cos\theta_K\right) \cdot \varepsilon_{\mathcal{A}}^{t,y}(\tilde{\phi}), \tag{7.1}$$

so that the acceptance function is derived individually for each angle. This assumption is validated in Ref. [2], where it is tested that flat distributions can be retrieved by applying the inverse acceptance.
The $\cos\theta_\ell$ and $\cos\theta_K$ angles are modeled by Legendre polynomials up to order four, given by

$$\begin{aligned} 1 + \sum_{i=1}^{4} c_i \mathcal{P}_i(x) = 1 + c_1 x + c_2 \frac{1}{2}\left(3x^2 - 1\right) \\ + c_3 \frac{1}{2}\left(5x^3 - 3x\right) + c_4 \frac{1}{8}\left(35x^4 - 30x^2 + 3\right). \end{aligned} \tag{7.2}$$

These Legendre polynomials are chosen in order to minimize the correlations between the coefficients c_i.
The angle $\cos\theta_\ell$ can be approximately expressed as an energy asymmetry between the two leptons. Since the reconstruction and selection are not expected to introduce a bias with respect to the lepton charge, the $\cos\theta_\ell$ acceptance is expected to be symmetric. Therefore, only the lowest order odd coefficient c_1 is kept. Indeed, as can be seen in Figure 7.1, this coefficient is compatible with zero. The PDF for the angular acceptance fit to $\cos\theta_\ell$ thus reads

$$\begin{aligned}\varepsilon^{t,y}_{\mathcal{A},\cos\theta_\ell}\left(\cos\theta_\ell; c^{t,y}_{l2}, c^{t,y}_{l4}\right) = 1 + c^{t,y}_{l1}\cos\theta_\ell + c^{t,y}_{l2}\frac{1}{2}\left(3\cos\theta^2_\ell - 1\right) \\ + c^{t,y}_{l4}\frac{1}{8}\left(35\cos\theta^4_\ell - 30\cos\theta^2_\ell + 3\right),\end{aligned} \tag{7.3}$$

where t denotes the trigger category and y the data taking period. The angular acceptance fits and fit parameters for $\cos\theta_\ell$ are shown in Figure 7.1.
The angle $\cos\theta_K$ can be approximately expressed as an energy asymmetry between the pion and kaon. Since there is a mass difference between the mesons, the $\cos\theta_K$ angular acceptance is expected to be asymmetric and is given by

$$\begin{aligned}\varepsilon^{t,y}_{\mathcal{A},\cos\theta_K}\left(\cos\theta_K; c^{t,y}_{K1}, c^{t,y}_{K3}\right) = 1 + c^{t,y}_{K1}\cos\theta_K \\ + c^{t,y}_{K2}\frac{1}{2}\left(3\cos\theta^2_K - 1\right) \\ + c^{t,y}_{K3}\frac{1}{2}\left(5\cos\theta^3_K - 3\cos\theta_K\right) \\ + c^{y,t}_{K4}\frac{1}{8}\left(35\cos\theta^4_K - 30\cos\theta^2_K + 3\right).\end{aligned} \tag{7.4}$$

The fit parameters and distributions of the $\cos\theta_K$ acceptance are shown in Figure 7.2.
The angle ϕ is found to be unaffected by the reconstruction and selection effects. Nevertheless, the flatness of the ϕ angular acceptance is tested against $\cos 2\phi$, $\sin 2\phi$, $\cos\phi$ and $\sin\phi$ effects. These are the most dangerous effects, since they could mimic BSM physics with non-zero values of $A_T^{(2)}$ or A_T^{Im}. The angular acceptance of ϕ is modeled by

$$\varepsilon^{t,y}_{\mathcal{A},\phi}\left(\phi; c^{t,y}_{c1}, c^{t,y}_{s1}, c^{t,y}_{c}, c^{t,y}_{s}\right) = 1 + c^{t,y}_{c}\cos 2\phi + c^{t,y}_{s}\sin 2\phi + c^{t,y}_{c1}\sin\phi + c^{t,y}_{s1}\cos\phi. \tag{7.5}$$

The acceptance fits and fit parameters are shown in Figure 7.3. All parameters are found to be compatible with zero within one to two σ. The χ^2/ndf with respect to a flat distribution is also computed and is found to be close to unity for all categories.

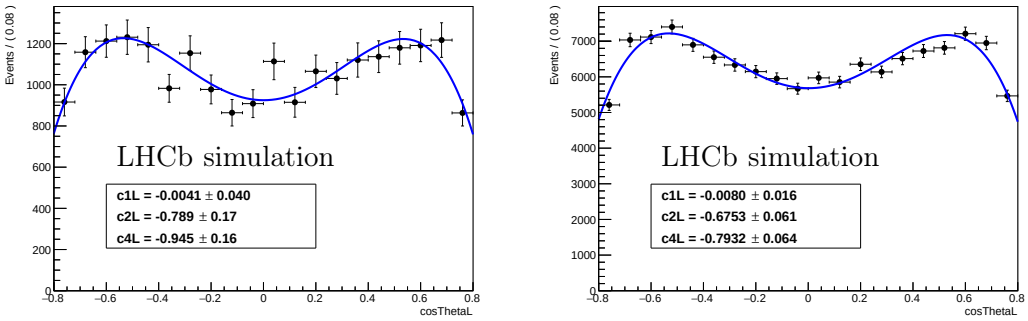

(a)

(b)

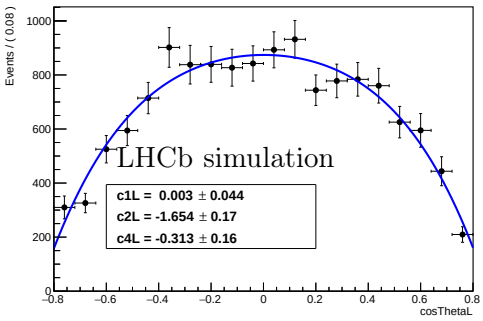

(c)

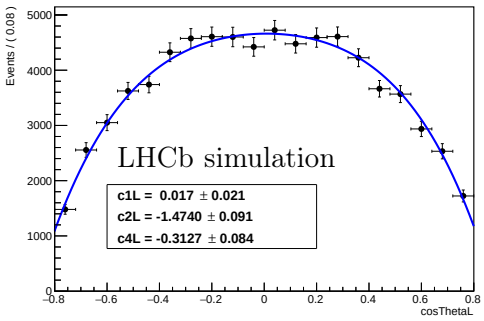

(d)

Figure 7.1: Fits to the $B^0 \to K^{*0} e^+ e^-$ phase-space MC sample of the $\cos\theta_\ell$ distribution, in the trigger category L0L (top) and L0I (bottom), for Run 1 (left) and Run 2 (right).

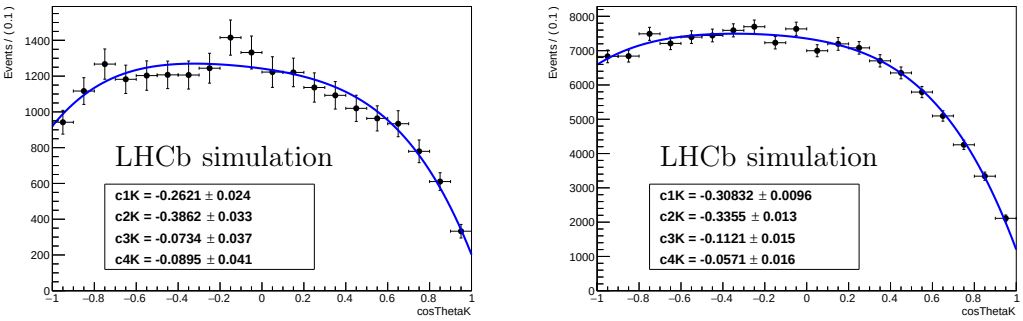

(a)

(b)

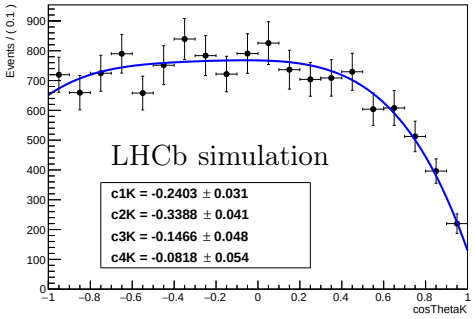

(c)

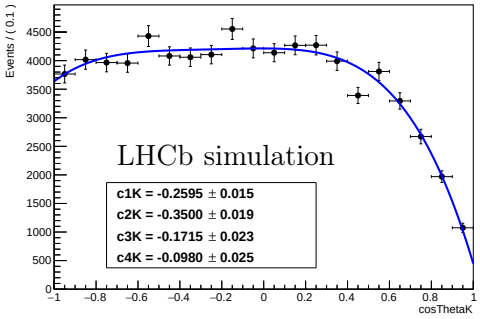

(d)

Figure 7.2: Fits to the $B^0 \to K^{*0}e^+e^-$ phase-space MC sample of the $\cos\theta_K$ distribution, in the trigger category L0L (top) and L0I (bottom), for Run 1 (left) and Run 2 (right).

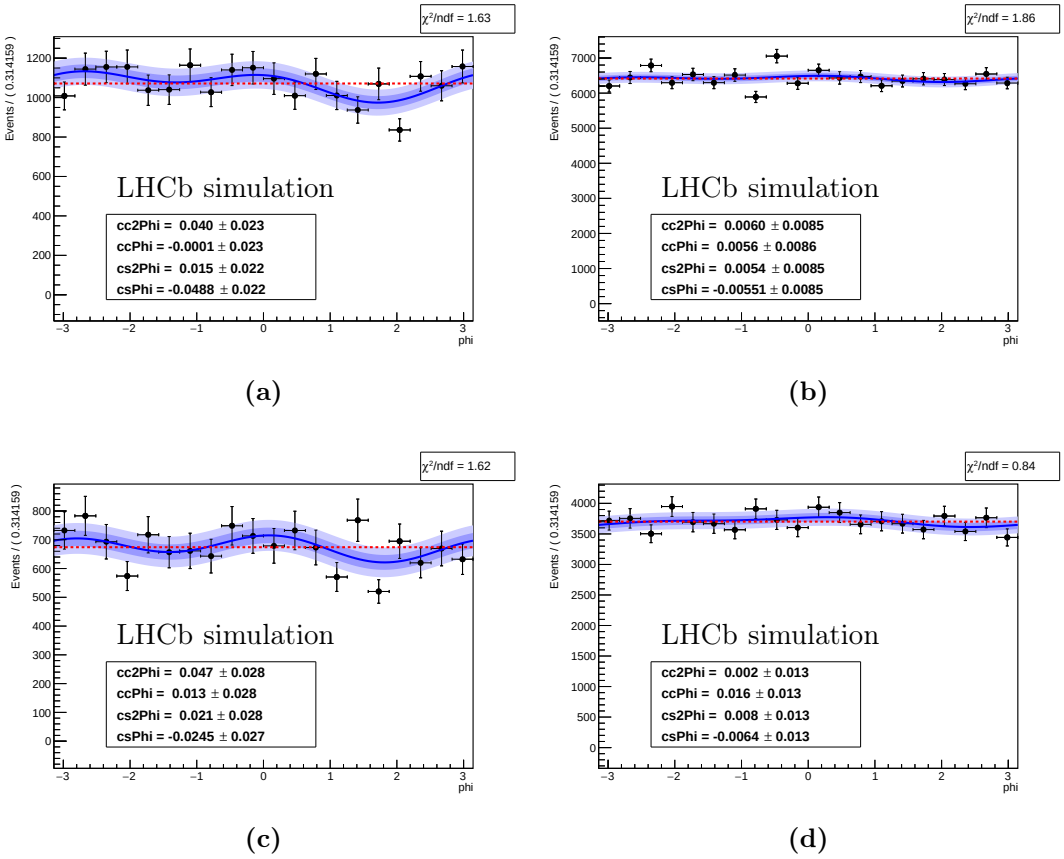

Figure 7.3: Fits to the $B^0 \to K^{*0}e^+e^-$ phase-space MC sample of the ϕ distribution, in the trigger category L0L (top) and L0I (bottom), for Run 1 (left) and Run 2 (right). The fitted function from Equation 7.5 is shown in blue with its associated 1 σ and 2 σ uncertainty bands. The χ^2/ndf with respect to a flat distribution (shown in dotted red) is given in the top right corner.

7.3 Angular modeling of backgrounds

As can be seen in the mass fit (see Section 6.2) there are several background components present in the fit. In order to perform the four dimensional fit to the $m(K^+\pi^-e^+e^-)$ invariant mass and the three angles $\cos\theta_K$, $\cos\theta_\ell$ and $\tilde{\phi}$, the angular shape of these background components has to be modeled as well. This section describes the different methods that are used to model each background component. When included in the four dimensional fit, the angular shapes of the background components are fixed to the shapes obtained in the following, only the fraction associated to each component is left to vary.

7.3.1 Angular modeling of partially reconstructed background

The easiest way to obtain a model for the angular shape of a background component is to use a dedicated MC simulation of this decay. Then, one takes a model PDF that is able to describe the shape and fixes the parameters by fitting it to the angular shape of the background component in MC simulation. For the partially reconstructed background one can use the $B^+ \to K_1(1270)(\to K^+\pi^-X)e^+e^-$ MC sample as is done in the mass fit (see Section 6.2.1). A simple choice for the modeling PDF can be the full angular signal PDF (see Equation 2.9), which is able to model compositions of quadratic shapes in $\cos\theta_K$ and $\cos\theta_\ell$ and trigonometric dependencies in $\tilde{\phi}$, multiplied with the angular acceptance functions.
The fit of the full angular signal PDF to the $B^+ \to K_1(1270)(\to K^+\pi^-X)e^+e^-$ MC sample is performed simultaneously in both runs and both trigger categories. The fit to the combined MC dataset is shown in Figure 7.4. The fit parameters are listed in Table 7.1. As one can see, the full angular signal PDF is able to model the angular shape of the partially reconstructed background.

Table 7.1: Fitted parameters of the full angular PDF on the $B^+ \to K_1(1270)(\to K^+\pi^-X)e^+e^-$ MC simulation.

Parameter	Value
$A_T^{(2)}$	0.003 ± 0.045
A_T^{Im}	-0.019 ± 0.044
A_T^{Re}	-0.003 ± 0.032
F_L	0.162 ± 0.012

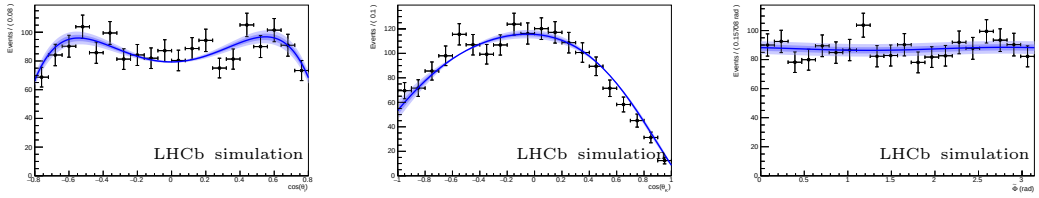

(a) **(b)** **(c)**

Figure 7.4: Fits of the full angular signal PDF to the $B^+ \to K_1(1270)(\to K^+\pi^- X)e^+e^-$ MC sample for all years (Run 1 + Run 2) and all trigger categories (L0L + L0I) combined.

7.3.2 Angular modeling of $B^0 \to K^{*0}\gamma(\to e^+e^-)$ background

The background component $B^0 \to K^{*0}\gamma(\to e^+e^-)$ has very similar physics to the signal channel $B^0 \to K^{*0}e^+e^-$. Therefore, a naive way to model the angular shape of this background would be to fit the full angular signal PDF to $B^0 \to K^{*0}\gamma(\to e^+e^-)$ MC sample, as is done for the partially reconstructed background. This does not work, however, as one can see in the fit projections onto the three angles in Figure 7.5. Especially the shape of the $\cos\theta_\ell$ distribution is not modeled properly. This can be explained, because the distributions of $\cos\theta_\ell$ and $\tilde{\phi}$ are not related to the physics of the $B^0 \to K^{*0}\gamma$ decay. Both distributions depend on the electrons, which for $B^0 \to K^{*0}\gamma(\to e^+e^-)$ are only present because of the interaction of the real photon with the detector material. Therefore, a new model has to be developed to describe the angular shape of $B^0 \to K^{*0}\gamma(\to e^+e^-)$.

The $\cos\theta_K$ distribution, however, is driven by the angular distributions of the kaon and pion, which stems from the longitudinal polarization of the K^* meson. One can capture this dependency by modeling the $\cos\theta_K$ distribution with the full angular signal PDF integrated over the $\cos\theta_\ell$ and $\tilde{\phi}$ angles, taking into account the angular acceptance. The resulting one-dimensional PDF describes the $\cos\theta_K$ distribution and has the longitudinal polarization F_L as only fit parameter.

It is checked that there is no remaining correlation between $\cos\theta_K$ and the other angles by comparing the distributions of $\cos\theta_\ell$ and $\tilde{\phi}$ in several bins of $\cos\theta_K$ as shown in Figure 7.7. The model is hence factorized into independent distributions for the three angles $\cos\theta_K$, $\cos\theta_\ell$ and $\tilde{\phi}$.

The $\cos\theta_\ell$ and $\tilde{\phi}$ distributions are not connected to the physics of the $B^0 \to K^{*0}\gamma$ decay and can therefore be modeled by polynomials that reproduce the shape

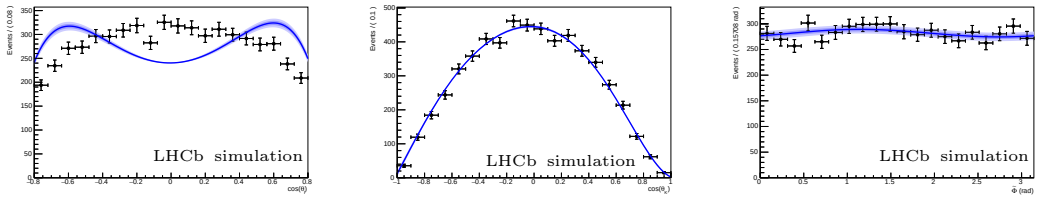

(a) **(b)** **(c)**

Figure 7.5: Fits of the full angular signal PDF to the $B^0 \to K^{*0}\gamma(\to e^+e^-)$ MC sample for all years (Run 1 + Run 2) and trigger categories (L0L + L0I) combined. One can see a clear mis-modeling of the $\cos\theta_\ell$ distribution.

of the distributions in MC simulation. The same functional form as used in the acceptance function is taken as model PDF given by

$$\begin{aligned} p_l^{t,y}(a_1^{t,y}, a_2^{t,y}, a_4^{t,y}, \cos\theta_\ell) = 1 + a_1^{t,y}\cos\theta_\ell + a_2^{t,y}\frac{1}{2}\left(3\cos{\theta_\ell}^2 - 1\right) \\ + a_4^{t,y}\frac{1}{8}\left(35\cos{\theta_\ell}^4 - 30\cos{\theta_\ell}^2 + 3\right), \\ p_{\tilde{\phi}}^{t,y}(C_s^{t,y}, C_c^{t,y}, \tilde{\phi}) = 1 + C_s^{t,y}\sin(2\tilde{\phi}) + C_c^{t,y}\cos(2\tilde{\phi}). \end{aligned} \tag{7.6}$$

The resulting fits projections are shown in Figure 7.6. The fitted F_L is found to be $0.32 \pm 0.33\%$, which is compatible with zero. This means a completely transverse K^* polarization, as expected due to the presence of the real photon.

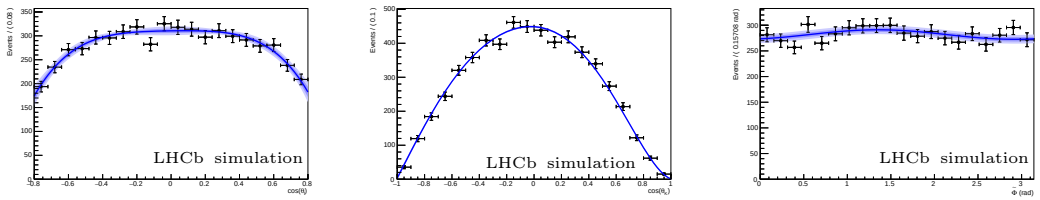

(a) **(b)** **(c)**

Figure 7.6: Fits of the custom model PDF to the $B^0 \to K^{*0}\gamma(\to e^+e^-)$ MC sample for all years (Run 1 + Run 2) and trigger categories (L0L + L0I) combined.

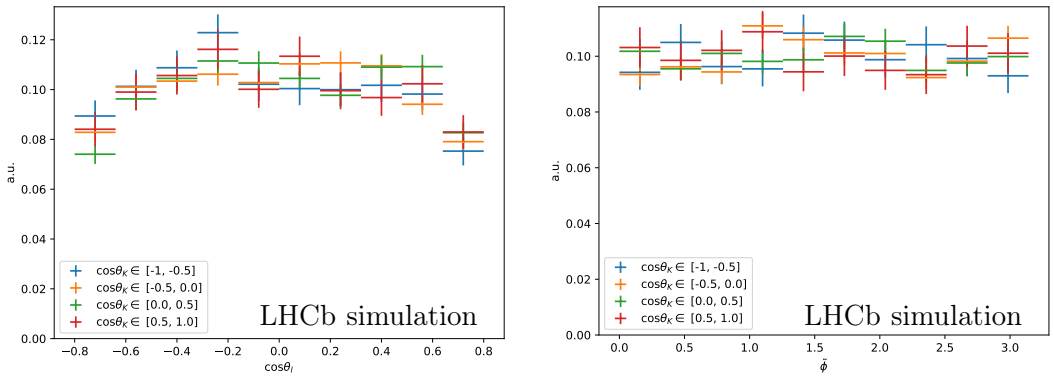

(a) **(b)**

Figure 7.7: Distribution of the $\cos\theta_\ell$ (left) and $\tilde{\phi}$ (right) angles in several bins of $\cos\theta_K$ in $B^0 \to K^{*0}\gamma(\to e^+e^-)$ MC simulation, for all years (Run 1 + Run 2) and trigger categories (L0L + L0I) combined.

7.3.3 Angular modeling of $B^0 \to K^{*0}\pi^0(\to \gamma e^+e^-)$ and $B^0 \to K^{*0}\eta(\to \gamma e^+e^-)$ backgrounds

The angular shapes of the background components $B^0 \to K^{*0}\pi^0(\to \gamma e^+e^-)$ and $B^0 \to K^{*0}\eta(\to \gamma e^+e^-)$, especially the $\cos\theta_K$ distribution, differ strongly from the angular shape of $B^0 \to K^{*0}\gamma(\to e^+e^-)$. The difference arises because the K^* longitudinal polarization is expected to be $F_\mathrm{L} = 1$ for these backgrounds because of the spin and angular momentum of the π^0 and η meson.
This can be tested by fitting the model developed for $B^0 \to K^{*0}\gamma$ to the $B^0 \to K^{*0}\pi^0(\to \gamma e^+e^-)$ MC sample. The resulting $\cos\theta_K$ distribution is shown in Figure 7.8. The fit does yield the expected value, but also hits the fit boundary of $F_\mathrm{L} = 1$ and lacks to describe the MC simulation at large values of $\cos\theta_K$. One can clearly see the different shape of the $\cos\theta_K$ distribution, however, compared to Figure 7.6 for $B^0 \to K^{*0}\gamma$ due to the different longitudinal polarization.
But since the shape of this background contribution is quite different to other backgrounds and the signal it is important to model it correctly in a converging fit. The $\cos\theta_K$ distribution can therefore not be modeled by the F_L dependent function but rather by polynomial functions to capture its shape. In order to do that a second problem has to be solved. The $\cos\theta_K$ distribution leads to the problem that there are basically no event with $\cos\theta_K \approx 0$. Fitting any polynomial function to the distribution would result in negative best fit values in the region of $\cos\theta_K \approx 0$. This is unphysical for a probability density distribution

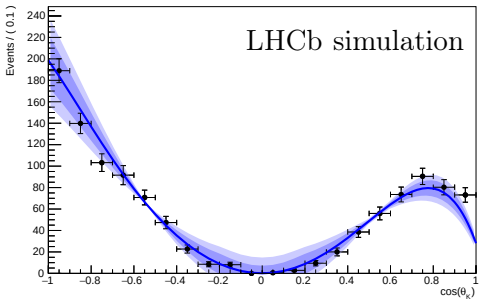

Figure 7.8: Fits of the F_{L} dependent PDF to the $\cos\theta_K$ distribution of $B^0 \to K^{*0}\pi^0(\to \gamma e^+e^-)$ MC simulation for all years (Run 1 + Run 2) and trigger categories (L0L + L0I) combined. The fit parameter F_{L} hits the physical boundary and one can see a mis-modeling for large values of $\cos\theta_K$.

and has to be avoided, especially when this background contribution is added as a component to the full fit to data.
This can be achieved by using Chebyshev polynomials and forcing positivity at $\cos\theta_K = 0$ by constraining the coefficients of the polynomial. Chebyshev polynomials of the first kind up to order four are given by

$$\begin{aligned} p_k(a_1, a_2, a_3, a_4, x) = 1 + a_1\, x + a_2\, \left(2x^2 - 1\right) + a_3\, \left(4x^3 - 3x\right) \\ + a_4\, \left(8x^4 - 8x^2 + 1\right). \end{aligned} \tag{7.7}$$

Constraining the coefficient a_4 such that

$$a_4 = a_2 - 1, \tag{7.8}$$

ensures that the function p_k is equal to zero at $x = 0$.
The $\cos\theta_\ell$ and $\tilde{\phi}$ distributions can again be modeled using the Legendre polynomials as used for the acceptance function. The fit to $B^0 \to K^{*0}\pi^0(\to \gamma e^+e^-)$ MC simulation is shown in Figure 7.9.
For the decay $B^0 \to K^{*0}\eta(\to \gamma e^+e^-)$ there is no event generator model available. Therefore, no physical MC simulation with correct angular shapes can be produced for this decay. Instead, the angular shape extracted for the π^0 meson from $B^0 \to K^{*0}\pi^0(\to \gamma e^+e^-)$ is used for the η meson. This is justified because both mesons have the same spin and parity. Therefore, both are expected to have very similar angular distributions.

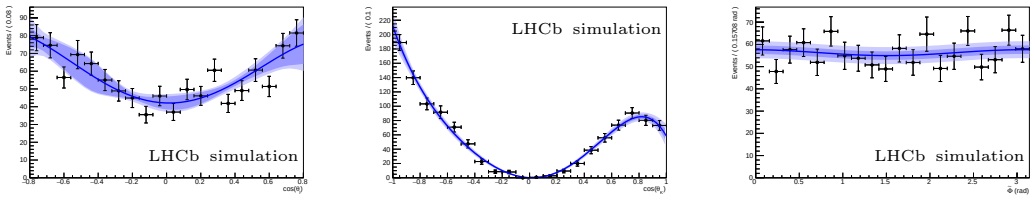

(a) **(b)** **(c)**

Figure 7.9: Fits of the fully polynomial PDF to the $B^0 \to K^{*0}\pi^0(\to \gamma e^+e^-)$ MC sample for all years (Run 1 + Run 2) and trigger categories (L0L + L0I) combined.

7.3.4 Angular modeling of combinatorial background

Modeling the angular shape of the combinatorial background is more difficult, since there is no MC sample consisting of combinatorial background that could be used directly. A widely used trick is to use data from the upper mass sideband, where there is little to no signal left and the data consists only of combinatorial background. This cannot be used for this analysis, however, since the *combinatorial* background considered here is a mixture of semi-leptonic background and combinatorial background contributions (SL/C). Both of which are expected to have different angular shapes. In addition the semi-leptonic background contribution is not present in the upper mass sideband, since the decays contributing to this background are missing particles. Therefore, a sample has to be found that includes both background contributions.
The candidate sample that can be used to model semi-leptonic and combinatorial background is $B^0 \to K^{*0}e^+\mu^-$ data. Due to lepton flavor conservation, this decay is forbidden in the SM. When reconstructing $B^0 \to K^{*0}e^+\mu^-$ candidates the $e^+\mu^-$ has to be formed from at least one random track, therefore being of combinatorial nature. In addition this data would contain the semi-leptonic background where the leptons are of different flavor in the cascading decays, if the same mass window as for the signal is kept.
The usage of $B^0 \to K^{*0}e^+\mu^-$ data as proxy for combinatorial and semi-leptonic background is validated by comparing it to $B^0 \to K^{*0}e^+e^-$ combinatorial and semi-leptonic background in the corner of phase-space where it is possible to separate this contribution from signal. The detailed studies can be found in Ref. [2].
It is important that the selection of $B^0 \to K^{*0}e^+\mu^-$ data is as close to the selection of $B^0 \to K^{*0}e^+e^-$ data as possible. The problem is that the resulting $B^0 \to K^{*0}e^+\mu^-$ data sample does not contain enough events to model the

angular shape properly. Some of the selection cuts have to be relaxed in order to assure proper modeling. Ref. [2] describes the procedure that is used to optimize these relaxations. The best trade-off of statistics versus compatibility of the parameters is found for

- modeling both runs together,
- increasing the q^2 range up to $\mathrm{m}_{\ell\ell} \in [10, 1000]$ MeV,
- increasing the mass window down to $m(K^+\pi^-\ell^+\ell^-) \in [4900, 5400]$ MeV,
- relaxing the cut on the multivariate classifier to BDT > 0.

The angular shape is modeled using Legendre polynomials up to order four for $\cos\theta_K$ and $\cos\theta_\ell$, including the odd order coefficients, and an acceptance like function for $\tilde{\phi}$. The fits to the enlarged $B^0 \to K^{*0}e^+\mu^-$ data sample are shown in Figure 7.10 for the three angles and both trigger categories. The obtained parameters define the shape of the combinatorial and semi-leptonic background components in the angular fit (SL/C).

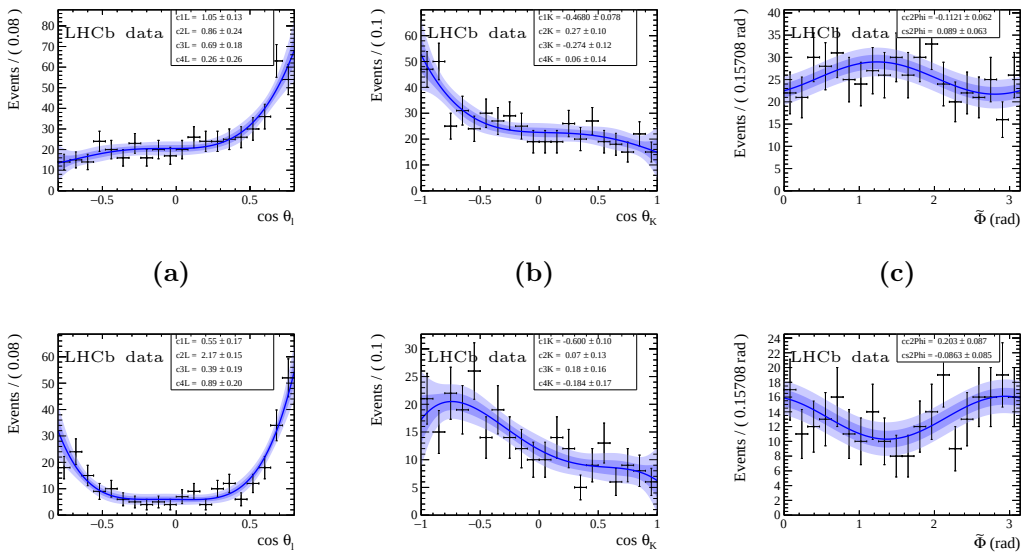

Figure 7.10: Angular fits for the combinatorial background (SL/C) to the enlarged data set of $B^0 \to K^{*0}e^+\mu^-$ decays, for the trigger category L0I (top, **a** to **c**) and L0L (bottom, **d** to **f**).

8 Fit validation

There are several measures taken in order to validate the fit procedure and analysis strategy.
These are developed and studied as part of the official LHCb analysis [1,2]. The author of this thesis contributed to the angular fit to $B^0 \to K^{*0}e^+e^-$ simulation, the angular modeling of background components in the fit to the control channel as well as implementing the full angular fit in the pseudo-experiments.

8.1 Angular fit to $B^0 \to K^{*0}e^+e^-$ simulation

The first fit validation consists of an angular fit to the $B^0 \to K^{*0}e^+e^-$ MC simulation. The full angular signal PDF (see Equation 2.9) is used including the angular acceptance, in order to extract the four observables F_{L}, $A_{\mathrm{T}}^{(2)}$, A_T^{Re} and A_T^{Im}. The fit projections onto the three angles $\cos\theta_K$, $\cos\theta_\ell$ and ϕ are shown in Figure 8.1.
The obtained values for the angular observables can then be compared to the values that were used to generate the MC simulation.
These latter values are extracted from a fit to a second, independent, $B^0 \to K^{*0}e^+e^-$ MC simulation at generator level, where no cuts at all are applied (see Figure 8.2). This generator level MC sample simulates the kinematics and angular distributions of the decay $B^0 \to K^{*0}e^+e^-$ but does not simulate the interaction of the particles with the LHCb detector. It also does not contain any

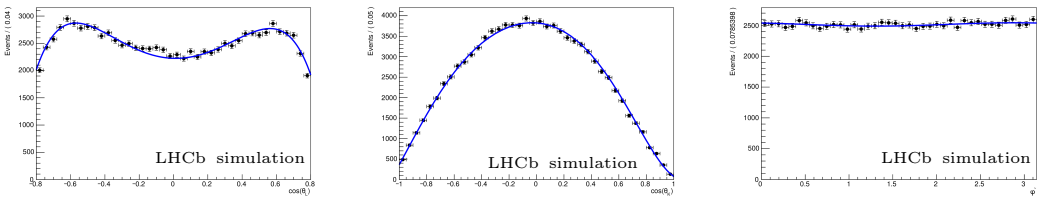

(a) **(b)** **(c)**

Figure 8.1: Fits of the full angular signal PDF to the reconstructed fully selected $B^0 \to K^{*0}e^+e^-$ MC sample for all years (Run 1 + Run 2) and all trigger categories (L0L + L0I) combined.

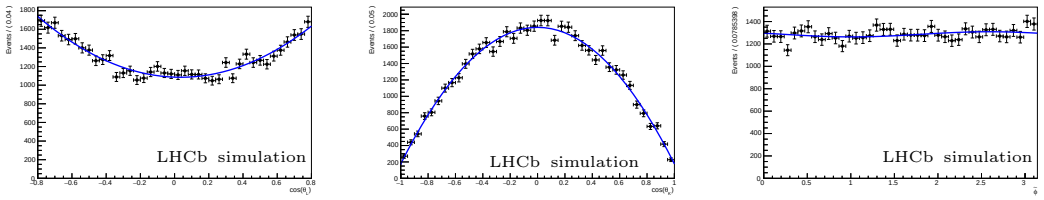

(a) **(b)** **(c)**

Figure 8.2: Fits of the full angular signal PDF to the generator level $B^0 \to K^{*0}e^+e^-$ MC sample without any selection applied.

geometric cuts that would force the final state particles to be within the LHCb detector acceptance. The fit to this generator level MC simulation therefore does not include the acceptance function but only the full angular signal PDF. In addition, the MC corrections discussed in Section 5.2 are not applied for this crosscheck.
The comparison between the two fit results therefore validates the angular acceptance modeling in the fit procedure.
One important difference between the generator level MC simulation without any cuts and the fully selected $B^0 \to K^{*0}e^+e^-$ MC simulation is the q^2 distribution, however. The generator level MC sample is simulated over the full phase space, while the selected MC sample is restricted to the very-low q^2-bin. But the q^2 distribution affects the angular distributions, since the angular observables, especially the longitudinal polarization F_{L}, are q^2 dependent. In order to be able to compare the angular observables from the two MC samples, the generator level MC sample is therefore weighted such that its m_{ee}^{true}distribution[1] matches that of the reconstructed MC sample after the full selection has been applied. The two q^2 distributions are shown in Figure 8.3.
Both fit results are compared in Table 8.1. All four angular observables are compatible within less than two σ. This validates the angular fit procedure and especially the modeling of the angular acceptance.

[1]The variable $m_{ee}^{\mathrm{true}}$is the true dielectron invariant mass in the MC simulation. There are no reconstructed variables for the generator level MC simulation.

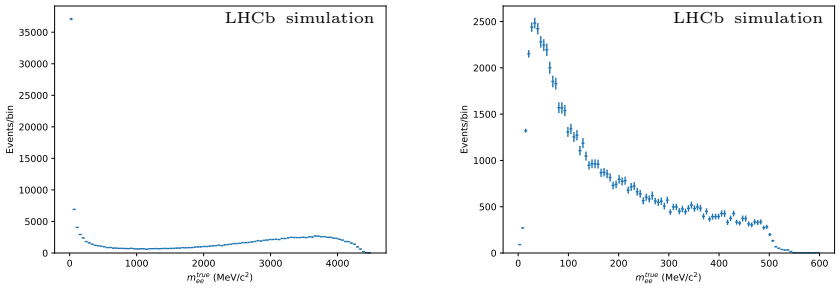

(a) (b)

Figure 8.3: Distribution of the true dielectron invariant mass of the generator level $B^0 \to K^{*0}e^+e^-$ MC simulation before (left) and after (right) weighting to match the distribution of the reconstructed and fully selected $B^0 \to K^{*0}e^+e^-$ MC simulation.

Table 8.1: Comparison of the fit parameters extracted from the fit to generator level and fully reconstructed and selected $B^0 \to K^{*0}e^+e^-$ MC simulation.

	$\mathbf{F_L}$	$\mathbf{A_T^{Re}}$	$\mathbf{A_T^{(2)}}$	$\mathbf{A_T^{Im}}$
gen	$(3.55 \pm 0.24)\%$	-0.032 ± 0.009	0.012 ± 0.014	-0.026 ± 0.014
reco	$(3.95 \pm 0.14)\%$	-0.019 ± 0.005	-0.003 ± 0.006	-0.022 ± 0.006

8.2 Angular Fit to $B^0 \to K^{*0}\gamma(\to e^+e^-)$ data

An additional important validation of the angular fit strategy is performed on the $B^0 \to K^{*0}\gamma(\to e^+e^-)$ control channel in MC simulation and data. For the $B^0 \to K^{*0}\gamma(\to e^+e^-)$ decay, the $\cos\theta_\ell$ and $\tilde{\phi}$ distributions are not related to the physics of the $B^0 \to K^{*0}\gamma$ decay, since the dielectron pair is only present due to the interaction of the photon with the detector material. An angular fit on $B^0 \to K^{*0}\gamma(\to e^+e^-)$ decays is therefore only performed on the $\cos\theta_K$ distribution.
The full angular signal PDF integrated over $\cos\theta_\ell$ and $\tilde{\phi}$ is used as fit model, as already introduced in Section 7.3.2. This PDF takes into account the acceptance function and is only sensitive to the longitudinal polarization F_L. Due to very low statistics in the gamma q^2-bin of the $B^0 \to K^{*0}e^+e^-$ MC simulation, the same acceptance as in the very-low q^2-bin is used.
The fit to the $\cos\theta_K$ distribution of $B^0 \to K^{*0}\gamma(\to e^+e^-)$ MC simulation is shown in Figure 7.6b. The fitted value of F_L is found to be $0.32 \pm 0.33\%$, which

is compatible with zero. This is the expected value, since the K^{*0} meson has to be completely transversely polarized due to the presence of the real photon. This fit can also be repeated on data. In order to do that, the angular analysis is performed in the gamma q^2-bin, which is dominated by $B^0 \to K^{*0}\gamma(\to e^+e^-)$ candidates. Since this is a fit to data, the angular shapes of background components that are present have to be modeled. They are composed of

- $B^0 \to K^{*0}e^+e^-$ decays. In the gamma q^2-bin, they now represent a background component, since $B^0 \to K^{*0}\gamma(\to e^+e^-)$ decays are considered as signal. The angular shape is extracted from a fit to $B^0 \to K^{*0}e^+e^-$ MC simulation in the gamma q^2-bin, with the full angular signal PDF integrated over the angles $\cos\theta_\ell$ and $\tilde{\phi}$.

- $B^0 \to K^{*0}\pi^0(\to \gamma(\to e^+e^-)\gamma)$ and $B^0 \to K^{*0}\eta(\to \gamma(\to e^+e^-)\gamma)$ decays. The same polynomial model as for the Dalitz decays (see Section 7.3.3) is used as fit model. The angular shapes are determined from fits to the respective $B^0 \to K^{*0}\pi^0(\to \gamma(\to e^+e^-)\gamma)$ and $B^0 \to K^{*0}\eta(\to \gamma(\to e^+e^-)\gamma)$ MC samples. As mentioned in the determination of their mass shape (see Section 6.2.1), the statistics of these samples are very small, so that the fit is not split into categories.

- Partially reconstructed decays. The F_L dependent part of the full angular signal PDF (as for the $B^0 \to K^{*0}\gamma(\to e^+e^-)$ signal and $B^0 \to K^{*0}e^+e^-$ background) is used as fit model. The angular shape of the partially reconstructed background is determined from a fit to $B^+ \to K_1(1270)(\to K^+\pi^-X)e^+e^-$ MC sample in the gamma q^2-bin.

- Combinatorial contributions. They are modeled using $B^0 \to K^{*0}e^+\mu^-$ data as done for the very-low q^2-bin (see Section 7.3.4). The exact same angular shape for the $\cos\theta_K$ distribution as in the very-low q^2-bin is used due to the very small amount of $B^0 \to K^{*0}e^+\mu^-$ events with $m_{ee} < 10\,\mathrm{MeV}$ and the observation that the $\cos\theta_K$ distribution does not vary much with m_{ee} [2].

Up to the difference that the full angular signal PDF is integrated over $\cos\theta_\ell$ and $\tilde{\phi}$, the complete angular analysis is performed in the gamma q^2-bin. This means that a two dimensional fit to the $m(K^+\pi^-e^+e^-)$ invariant mass and the angle $\cos\theta_K$ is performed in the narrow mass range $m(K^+\pi^-e^+e^-) \in [5000, 5400]\,\mathrm{MeV}$, where the fractions of signal and background components are Gaussian constrained to their values obtained from the mass fit in the wide range. The mass and angular fits are shown in Figure 8.4. The result of the fit yields a longitudinal polarization fraction of the K^{*0} meson of $F_\mathrm{L} = 0.0^{+0.7}_{-0.0}\,\%$.

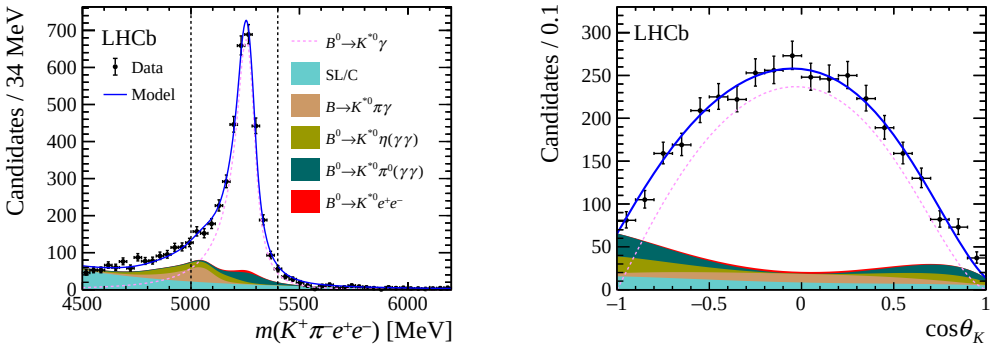

(a) **(b)**

Figure 8.4: Distributions of the (left) $K^+\pi^-e^+e^-$ invariant mass and (right) $\cos\theta_K$ angle of $B^0 \to K^{*0}\gamma(\to e^+e^-)$ candidates in the control channel. The angular fit including the background components is shown for all years (Run 1 + Run 2) and trigger categories (L0L + L0I) combined. The dashed vertical lines indicate the narrow mass range used in the angular fit.

This value is compatible with the expected complete transverse polarization of the K^{*0} meson. This angular fit to the $B^0 \to K^{*0}\gamma(\to e^+e^-)$ control channel is therefore an excellent crosscheck of the angular analysis, as the fit procedure matches the strategy that is employed for the $B^0 \to K^{*0}e^+e^-$ signal channel.

8.3 Usage of pseudo-experiments

One important toolkit for testing the stability of the fit and compute systematic uncertainties is the usage of pseudo-experiments. These pseudo-experiments rely on the generation of so called toy datasets or short toys, that include signal and background components on which the angular analysis can be performed. One pseudo-experiment contains the following steps:

1. **Generation**
   - Specify values for the angular observables so that the angular shape of the signal is given.
   - Get the mass shape of the signal from a fit to MC simulation with a given mass model.
   - Get the mass and angular shapes of background components from fits to the respective MC simulations with specified models.

- Get the acceptance function from a fit to MC simulation with a given acceptance model.
- Specify the amount of events that should be generated in the gamma and very-low q^2-bin, respectively.
- Generate two four dimensional datasets based on the mass and angular shapes of signal and background contributions for the signal and control channel. The fractions associated to each component is taken from the mass fit to (real) data.

2. Fitting

- Get the mass shape of the signal from a fit to MC simulation with a given mass model.
- Get the mass shape of background components from fits to the respective MC simulation with specified (potentially different) models.
- Perform the simultaneous mass fit in the wide mass window to the generated data in the signal and control channel and extract the fractions associated to each fit component.
- Get the angular shape of background components from fits to the respective MC simulation with specified (potentially different) models.
- Get the acceptance function from a fit to MC simulation with a given (potentially different) acceptance model.
- Perform the four dimensional fit in the narrow mass window to the generated data in the signal channel and extract the angular observables. The fractions associated to each fit component are Gaussian constrained to the values obtained from the mass fit in the wide mass window.
- Save the best fit value and uncertainty estimation of the four angular observables.

This procedure is then repeated for a large number of toy datasets and the resulting distributions of the best fit values of the angular observables are used to infer knowledge about the fit strategy, since this procedure simulates the experiment.
It is possible to specify different models that are used for generation and fitting of these toy datasets, so that systematic effects can be studied.
Figure 8.5 shows the distributions of the fitted value, uncertainty and pull[2] for

10000 toys fitted with a Gaussian function. Each toy is generated with the values obtained from the fit to data for the angular observables, the nominal shapes for the background components during generation and fitting and realistic number of events of 873 for the very-low q^2-bin and 6129 for the gamma q^2-bin.
No large biases are observed for the angular observables and the width of the pull distributions are compatible with unity, which implies a correct coverage of uncertainties. Only the observable F_{L} shows a small bias of 0.003. This is due to the proximity to the unphysical region with $F_{\mathrm{L}} < 0$, where the fit becomes unstable. The fitted value of F_{L} in data is therefore corrected for the bias on F_{L} and the correction is assigned as a systematic uncertainty.
Besides checking for potential biases in the fit, the pseudo-experiments can be used to asses the size of potential systematic uncertainties. In this analysis, mainly two potential sources of systematic uncertainties are considered. There are uncertainties related to the statistics of the samples used to model mass and angular shapes as well as the acceptance. And there are uncertainties related to the choice of the model itself.
The uncertainties related to the limited size of the data and simulation samples are addressed with a bootstrapping technique [85]. This technique relies on re-sampling the corresponding dataset and repeating the full fit several times to get the pull distributions, which are sensitive to the systematic uncertainty. In order to avoid any fluctuations related to the available statistics in data, the 1000 toys for the bootstrapping are generated with 10 times more events than in data.
The uncertainties related to the various modeling choices used in the fits are evaluated by using toy datasets that are generated with alternative models and fitted with the nominal models used in the fit to data. The systematic uncertainties are then extracted from deviations in the resulting distributions of the angular observables compared to the nominal ones.
The different systematic uncertainties that are considered are summarized in Table 8.2. The total systematic uncertainty, obtained by adding all individual sources in quadrature, is smaller than the statistical uncertainty for all observables. A detailed description of all individual sources of systematic uncertainty and the assessment of their size can be found in Ref. [2].

[2]The pull is defined as the difference between fitted and generated value divided by fitted uncertainty of the value.

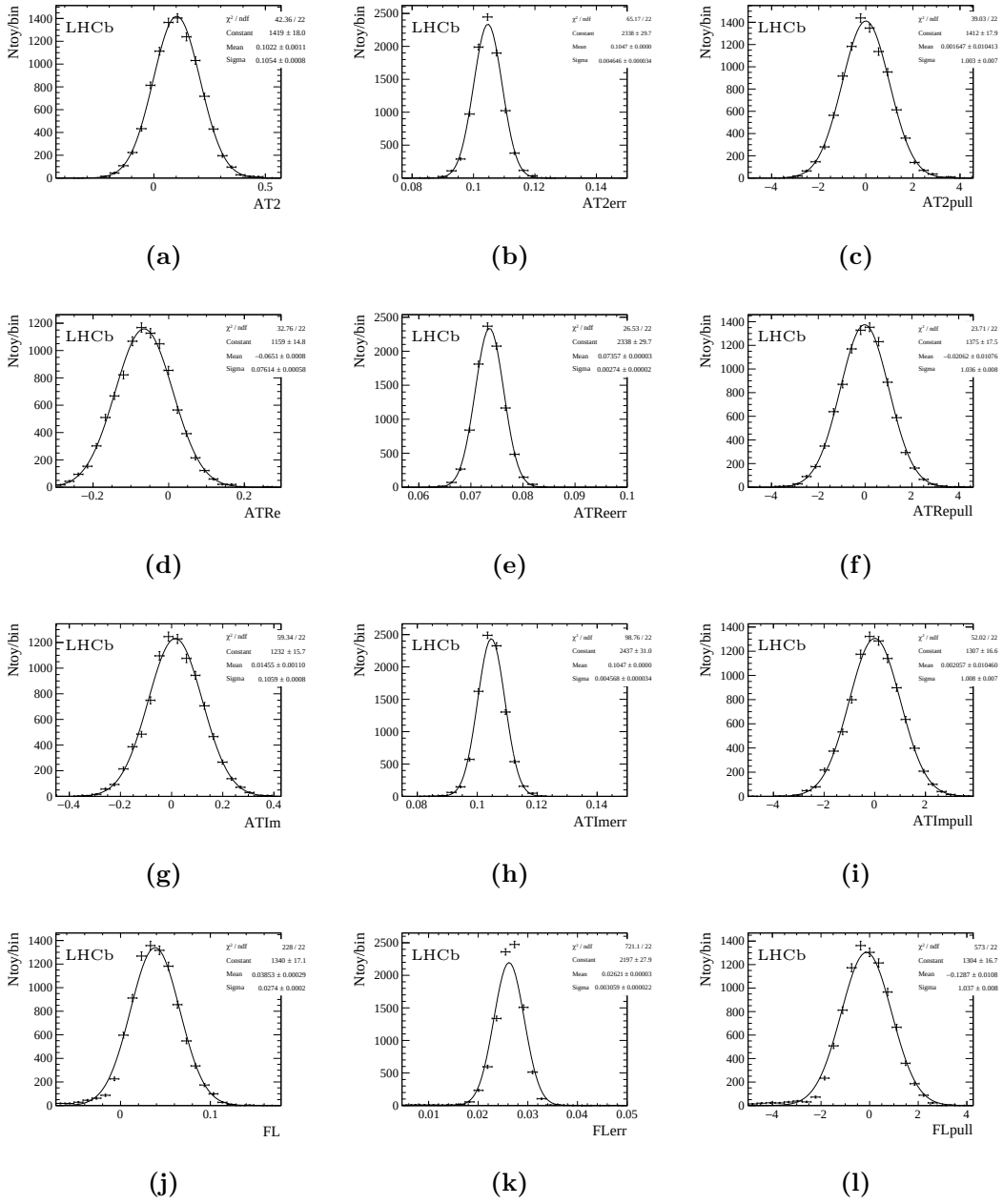

Figure 8.5: Distributions of the fitted values (left), uncertainties (middle) and pulls (right) of 10000 toy datasets for the four angular observable $A_T^{(2)}$, A_T^{Re}, A_T^{Im} and $F_{\rm L}$ (from top to bottom). The angular observables were generated with the central values of the fit to data.

Table 8.2: Summary of systematic uncertainties on the four angular observables. The total systematic uncertainty is the sum in quadrature of all the contributions. For comparison, the statistical uncertainties are shown in the last row of the table.

Source of systematic	$\boldsymbol{A_T^{(2)}}$	$\boldsymbol{A_T^{Im}}$	$\boldsymbol{A_T^{Re}}$	$\boldsymbol{F_L}$
Simulation sample size for acceptance	0.007	0.007	0.007	0.003
Acceptance function modeling	0.004	0.001	0.008	0.001
$B^0 \to K^{*0} e^+ \mu^-$ sample size for SL/C	0.007	0.007	0.007	0.003
SL/C angular modeling	0.012	0.005	0.006	0.005
PR model other than $K_1(1270)$	0.001	0.003	0.002	0.001
η or π^0 angular modeling	< 0.001	< 0.001	0.002	0.010
Corrections to simulation	0.003	0.001	0.003	0.007
Signal mass shape	0.002	0.002	0.004	0.001
Total systematic uncertainty	0.017	0.012	0.015	0.014
Statistical uncertainty	0.103	0.102	0.077	0.026

9 Results

9.1 Angular observables

An angular analysis of the $B^0 \to K^{*0}e^+e^-$ decay is performed in the effective q^2 range from 0.0008 to 0.257 GeV^2 [1, 2]. The four angular observables $F_{\rm L}$,$A_T^{(2)}$,A_T^{Re} and A_T^{Im} are extracted from a four dimensional fit to the invariant mass $m(K^+\pi^-e^+e^-)$ in the range 5000 to 5400 MeV and the three angles $\cos\theta_K$, $\cos\theta_\ell$ and $\tilde{\phi}$. The invariant mass distribution and the angular distributions together with the PDF projections resulting from the fit are shown in Figure 9.1. The four $B^0 \to K^{*0}e^+e^-$ angular observables measured in the effective q^2 range from 0.0008 to 0.257 GeV^2 are found to be

$$\begin{aligned} F_{\rm L} &= 0.044 \pm 0.026 \pm 0.014, \\ A_T^{Re} &= -0.064 \pm 0.077 \pm 0.015, \\ A_T^{(2)} &= +0.106 \pm 0.103 \pm 0.017, \\ A_T^{Im} &= +0.015 \pm 0.102 \pm 0.012, \end{aligned}$$

where the first contribution to the uncertainty is statistical and the second systematic. Correlations between the observables are measured to be

	$F_{\rm L}$	A_T^{Re}	$A_T^{(2)}$	A_T^{Im}
$F_{\rm L}$	1.00	−0.02	−0.01	0.02
A_T^{Re}		1.00	0.05	0.02
$A_T^{(2)}$			1.00	0.10
A_T^{Im}				1.00

These results supersede the previous angular analysis of $B^0 \to K^{*0}e^+e^-$ decays at LHCb from Ref. [45].
The SM predictions of the four angular observables are computed with the FLAVIO [43] software package (see Equation 2.11). All four angular observables are compatible with their SM prediction within one σ.

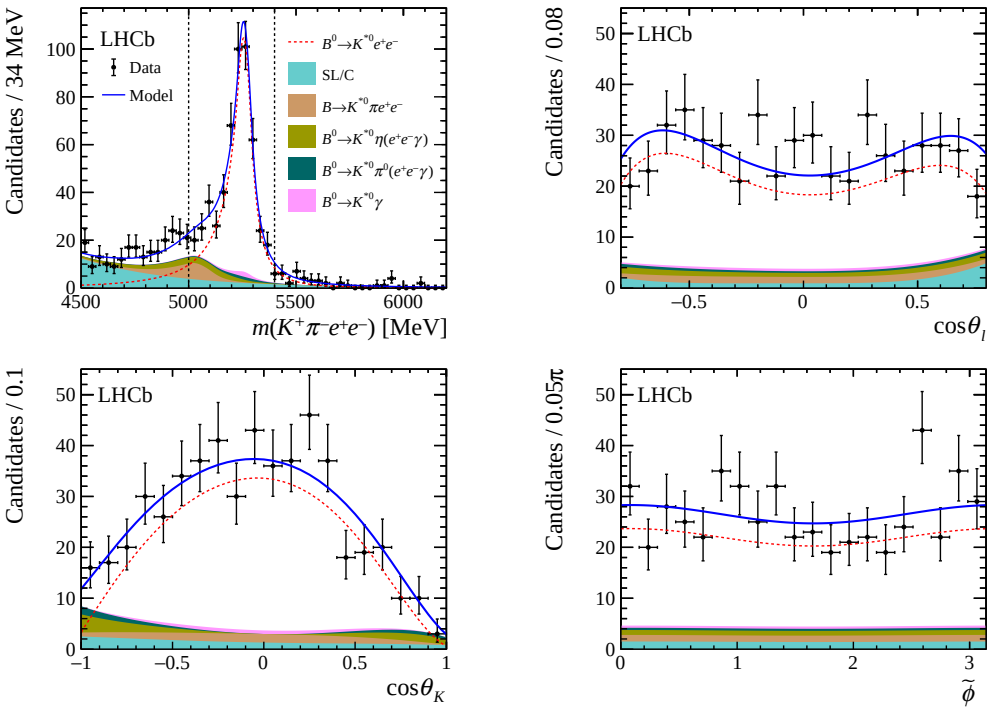

Figure 9.1: Distributions of the (top left) $K^+\pi^-e^+e^-$ invariant mass, (top right) $\cos\theta_\ell$, (bottom left) $\cos\theta_K$ and (bottom right) $\tilde{\phi}$ variables of $B^0 \to K^{*0}e^+e^-$ candidates in the very-low q^2-bin. The angular fit including the background components is shown for all years (Run 1 + Run 2) and trigger categories (L0L + L0I) combined. The dashed vertical lines indicate the narrow mass range used in the angular fit.

9.2 Photon polarization in $b \to s\gamma$ transitions

Using Equation 2.10, the measured values of the $A_T^{(2)}$ and A_T^{Im} observables can be used to determine the photon polarization in $B^0 \to K^{*0}\gamma$ decays

$$\begin{aligned} \mathrm{Re}\,(A_\mathrm{R}/A_\mathrm{L}) &= 0.05 \pm 0.05 \\ \mathrm{Im}\,(A_\mathrm{R}/A_\mathrm{L}) &= 0.01 \pm 0.05. \end{aligned}$$

Then, the FLAVIO software package can be used to translate these measurements into the photon polarization of the $b \to s\gamma$ transition, which can be expressed as the ratio of right- and left-handed $\mathcal{C}_7^{(\prime)}$ Wilson coefficients. The details about the calculation of hadronic contributions can be found in Ref. [44]. The obtained constraints are presented in Figure 9.2, where they are compared to the constraints from previous measurements by the Belle, BaBar and LHCb experiments [30–34, 37–39]. For these calculations, the $\mathcal{C}_7^{(\prime)}$ regularization-scheme independent effective coefficents are evaluated at a scale $\mu = 4.8\,\mathrm{GeV}$ [44]. In addition, the value of the left-handed $\mathcal{C}_7$ Wilson coefficient is fixed to its SM value, $\mathcal{C}_7^{\mathrm{SM}} = -0.2915$. The theoretical uncertainties related to predictions of the experimental observables are taken into account in the constrained areas. The results of this analysis provide the world's best constraint on the $b \to s\gamma$ photon polarization.

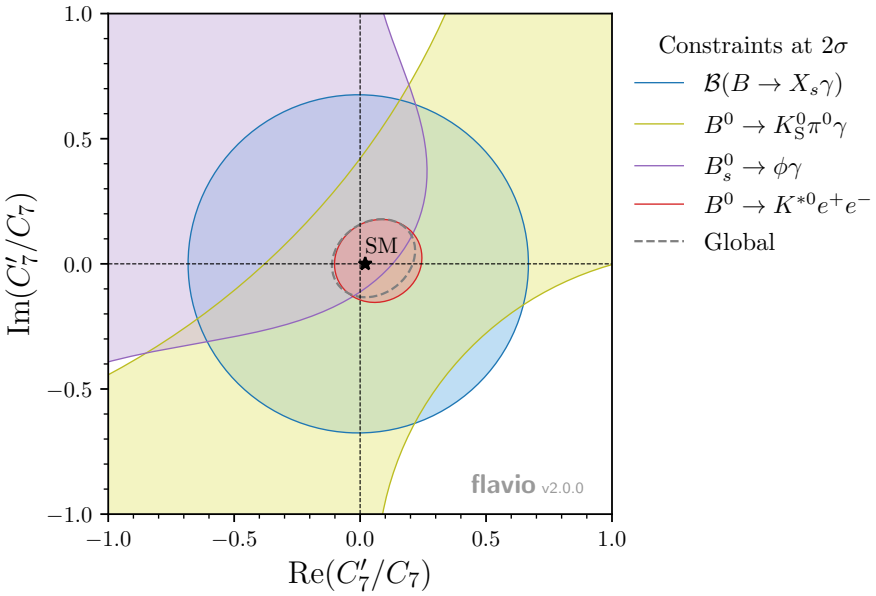

Figure 9.2: Constraints at 2σ level on the real and imaginary parts of the ratio of right- and left-handed Wilson coefficients, C_7' and C_7. The measurements of the inclusive branching fraction, $\mathcal{B}(B \to X_s\gamma)$, and the $B^0 \to K^0_S\pi^0\gamma$ mixing-induced CP asymmetry by the Belle and BaBar experiments [30–34, 37, 38] are shown in blue and yellow, respectively, the $B^0_s \to \phi\gamma$ measurements at LHCb [39] in purple and the measurement presented in this thesis in red. The global fit is shown in dashed lines and the SM prediction is represented by a black star and corresponds to the ratio of s- and b-quark masses.

9.3 Branching fraction of the $B^0 \to K^{*0}e^+e^-$ decay

A branching ratio measurement of the $B^0 \to K^{*0}e^+e^-$ decay in the effective q^2 range from 0.0008 to 0.257 GeV^2 with respect to the $B^0 \to K^{*0}J/\psi(\to e^+e^-)$ reference decay is performed. The branching ratio is extracted from a fit to the invariant mass $m(K^+\pi^-e^+e^-)$ in the range 4500 to 6200 MeV in the signal channel, where the yield of $B^0 \to K^{*0}J/\psi(\to e^+e^-)$ decays is constraint to the value obtained from a fit to the invariant mass $m(K^+\pi^-e^+e^-)$ in the range 4700 to 6200 MeV in the reference channel.
The branching ratio measured in the effective q^2 range from 0.0008 to 0.257 GeV^2 is found to be

$$R(\mathcal{B}) = \frac{\mathcal{B}(B^0 \to K^{*0}e^+e^-)}{\mathcal{B}(B^0 \to (K^+\pi^-)J/\psi(\to e^+e^-))} = (2.49 \pm 0.12) \times 10^{-3},$$

where the contribution to the uncertainty is statistical only.
This can be translated into to branching fraction of the $B^0 \to K^{*0} e^+ e^-$ decay, by taking the branching fraction of the $B^0 \to K^{*0} J/\psi\,(\to e^+ e^-)$ decay from the PDG [69],

$$\mathcal{B}(B^0 \to K^{*0} J/\psi)_{PDG} = (1.27 \pm 0.05) \times 10^{-3}$$
$$\mathcal{B}(J/\psi \to e^+ e^-)_{PDG} = (5.971 \pm 0.032) \times 10^{-2}.$$

The branching fraction from the PDG, however, only includes the P-wave contribution of the K^{*0} decay. In the measurement, the region $|m(K\pi) - m^{PDG}_{K^{*0}}| < 100\,\text{MeV}$ is selected, which also contains the S-wave contribution. This contribution has to be accounted for by using the fraction of $K^+\pi^-$ pairs in an S-wave configuration in the selected mass range to the $B^0 \to K^{*0} J/\psi$ decay [86],

$$F_{\text{S}}^{J/\psi} = 0.084 \pm 0.010$$
$$\mathcal{B}(B^0 \to (K^+\pi^-) J/\psi) = \frac{\mathcal{B}(B^0 \to K^{*0} J/\psi)}{1 - F_{\text{S}}^{J/\psi}}$$

With that, the branching fraction of the decay $B^0 \to K^{*0} e^+ e^-$ in the effective q^2 range from 0.0008 to 0.257 GeV^2 is measured to be

$$\mathcal{B}(B^0 \to K^{*0} e^+ e^-)_{exp} = (2.06 \pm 0.10 \pm 0.08) \times 10^{-7},$$

where the first contribution to the uncertainty is statistical and the second due to the uncertainty of the external inputs.

Theory prediction of the branching fraction

The FLAVIO [43] software package can be used again to obtain a SM prediction for the branching fraction of the $B^0 \to K^{*0} e^+ e^-$ decay in the effective q^2 region from 0.0008 to 0.257 GeV^2. The SM prediction is computed to be

$$\mathcal{B}(B^0 \to K^{*0} e^+ e^-)_{th} = (2.0 \pm 0.4) \times 10^{-7},$$

with a relatively large relative uncertainty of 20% due to hadronic uncertainties. The measured branching fraction is compatible with the SM prediction within one σ.
As a crosscheck, one can compare the experimental ratio of branching fractions of the $B^0 \to K^{*0} e^+ e^-$ decay over the $B^0 \to K^{*0} \gamma$ decay to a theory prediction of this ratio. At very low q^2, the predictions for both branching fractions are very correlated, since the underlying physics is very similar. Therefore, hadronic uncertainties that dominate the theoretical uncertainty should cancel in the

ratio of both branching fractions to a large extend. Hence, the prediction for the resulting ratio should have much better precision.
The FLAVIO software package can be used to obtain sets of randomly re-sampled theory parameters. For each set of theory parameters the $B^0 \to K^{*0} e^+ e^-$ and $B^0 \to K^{*0}\gamma$ branching fraction is predicted. Then the ratio is calculated as the mean of the set of predicited ratios with an uncertainty corresponding to the standard deviation of the set of ratios,

$$\left[\frac{\mathcal{B}(B^0 \to K^{*0} e^+ e^-)}{\mathcal{B}(B^0 \to K^{*0}\gamma)}\right]_{\text{FLAVIO}} = (4.77 \pm 0.07) \times 10^{-3}.$$

This prediction only comes with a relative uncertainty of about 1%. The experimental ratio can be calculated using the nominal value of the branching fraction of the $B^0 \to K^{*0}\gamma$ decay from the PDG [69]

$$\mathcal{B}(B^0 \to K^{*0}\gamma)_{PDG} = (4.18 \pm 0.25) \times 10^{-5}.$$

With this, one can calculate the ratio of branching fractions of the $B^0 \to K^{*0} e^+ e^-$ decay over the $B^0 \to K^{*0}\gamma$ decay in the effective q^2 range from 0.0008 to 0.257 GeV^2

$$\frac{\mathcal{B}(B^0 \to K^{*0} e^+ e^-)_{exp}}{\mathcal{B}(B^0 \to K^{*0}\gamma)_{PDG}} = (4.93 \pm 0.24 \pm 0.36) \times 10^{-3},$$

where the first contribution to the uncertainty is statistical and the second due to the uncertainty on the external inputs. The experimental value of the ratio of branching fractions is compatible with the SM theory prediction from FLAVIO within one σ.

10 Conclusion

An angular analysis and branching fraction measurement of the $B^0 \to K^{*0} e^+ e^-$ decay is performed using proton-proton collision data, corresponding to an integrated luminosity of 9 fb^{-1}, collected by the LHCb experiment between 2011 and 2018 [1, 2]. The angular observables and branching fraction are measured for the first time in the q^2 range from 0.0008 to 0.257 GeV^2.

The aim of this thesis was to constrain the photon polarization in the $b \to s\gamma$ transition that mediates the $B^0 \to K^{*0} e^+ e^-$ decay in the selected very low q^2 region. This decay is suppressed in the SM and thus sensitive to BSM physics contributions. Any sign of a significant right-handed polarization would be an unambiguous indication of BSM physics.

The analysis presented here supersedes previous measurements by the LHCb collaboration [45]. It exploits an improved data selection and fit strategy as well as a larger dataset. A pure sample of $B^0 \to K^{*0} e^+ e^-$ decays is obtained with only about 20% background contributions. All these background components are well studied and modeled in the invariant mass and angular fits. This results in small systematic uncertainties and statistically dominated uncertainties of the angular observables. Systematic uncertainties were not determined for the branching ratio measurement due to the time constraints for this master thesis.

All results of this thesis are compatible with SM predictions and the angular observables are used to measure both the real and imaginary parts of the $B^0 \to K^{*0}\gamma$ photon polarization with a precision of 5%. In addition, these results are used to constrain the photon polarization in $b \to s\gamma$ transitions with significantly better precision than the combination of previous measurements.

The angular analysis and branching fraction measurement, however, will improve in the future with more data collected by the LHCb experiment, as the detector is currently undergoing major upgrades to be ready for the higher luminosity that will be provided by the upgrade of the LHC accelerator. In addition, this analysis at the very low end of the q^2 spectrum yields important insights and understanding of background contributions that are relevant to analysis of the $B^0 \to K^{*0} e^+ e^-$ decay over the full q^2 range, which are interesting in the light of hints of lepton flavor non-universality in $b \to s\ell^+\ell^-$ transitions and the so-called B flavor anomalies [59, 87, 88].

A Appendix

A.1 Angular observables in terms of transversity amplitudes

The four angular observables of the angular analysis (see Equation 2.8 and Equation 2.9) can be expressed as functions of the transversity amplitudes as follows [49, 50]

$$
\begin{aligned}
F_{\mathrm{L}} &= \frac{|A_0|^2}{|A_0|^2 + \left|A_\parallel\right|^2 + |A_\perp|^2}, \\
A_T^{(2)} &= \frac{|A_\perp|^2 - \left|A_\parallel\right|^2}{|A_\perp|^2 + \left|A_\parallel\right|^2}, \\
A_T^{Re} &= \frac{2\mathcal{R}e\left(A_\parallel^L A_\perp^{L*} + A_\parallel^R A_\perp^{R*}\right)}{|A_\perp|^2 + \left|A_\parallel\right|^2}, \\
A_T^{Im} &= \frac{2\mathcal{I}m\left(A_\parallel^L A_\perp^{L*} + A_\parallel^R A_\perp^{R*}\right)}{|A_\perp|^2 + \left|A_\parallel\right|^2}.
\end{aligned}
\tag{A.1}
$$

The transversity amplitudes themselves are defined in Ref. [47] as

$$
\begin{aligned}
A_{\perp}^{L,R}\left(q^2\right) &= N\left(q^2\right)\sqrt{2\lambda\left(q^2\right)}\left\{\frac{2m_b}{q2}\left(\mathcal{C}_7+\mathcal{C}_7'\right)T_1\left(q^2\right)\right. \\
&\left.+\left[\left(\mathcal{C}_9+\mathcal{C}_9'\right)\mp\left(\mathcal{C}_{10}+\mathcal{C}_{10}'\right)\right]\frac{V\left(q^2\right)}{m_B+m_{K^{*0}}}\right\}, \\
A_{\parallel}^{L,R}\left(q^2\right) &= -N\left(q^2\right)\sqrt{2}\left(m_B^2-m_{K^{*0}}^2\right)\left\{\frac{2m_b}{q^2}\left(\mathcal{C}_7-\mathcal{C}_7'\right)T_2\left(q^2\right)\right. \\
&\left.+\left[\left(\mathcal{C}_9-\mathcal{C}_9'\right)\mp\left(\mathcal{C}_{10}-\mathcal{C}_{10}'\right)\right]\frac{A_1\left(q^2\right)}{m_B-m_{K^{*0}}}\right\}, \\
A_0^{L,R}\left(q^2\right) &= -\frac{N\left(q^2\right)}{2m_{K^{*0}}\sqrt{q^2}}\left\{\left[\left(\mathcal{C}_9-\mathcal{C}_9'\right)\mp\left(\mathcal{C}_{10}-\mathcal{C}_{10}'\right)\right]\right. \\
&\times\left[\left(m_B^2-m_{K^{*0}}^2-q^2\right)\left(m_B+m_{K^{*0}}\right)A_1\left(q^2\right)-\lambda\left(q^2\right)\frac{A_2\left(q^2\right)}{m_B^2-m_{K^{*0}}^2}\right] \\
&\left.+2m_b\left(\mathcal{C}_7-\mathcal{C}_7'\right)\left[\left(m_B^2+3m_{K^{*0}}^2-q^2\right)T_2\left(q^2\right)-\frac{\lambda\left(q^2\right)}{m_B^2-m_{K^{*0}}^2}T_3\left(q^2\right)\right]\right\}
\end{aligned}
\tag{A.2}
$$

where

$$
\begin{aligned}
N\left(q^2\right) &= V_{tb}V_{ts}^*\left[\frac{G_F^2\alpha^2}{2^{10}\pi^5 m_B^3}\frac{\beta_e\left(q^2\right)}{3}q^2\sqrt{\lambda\left(q^2\right)}\right]^{1/2}, \\
\beta_l\left(q^2\right) &= \sqrt{1-\frac{4m_e^2}{q^2}}, \\
\lambda\left(q^2\right) &= \left[q^2-\left(m_B+m_{K^{*0}}\right)^2\right]\left[q^2-\left(m_B-m_{K^{*0}}\right)^2\right]
\end{aligned}
\tag{A.3}
$$

and $V(q^2)$, $A_{1,2}(q^2)$ and $T_{1,2,3}(q^2)$ are hadronic form factors.

B Lists

B.1 List of Figures

2.1 Elementary particles of the Standard Model 6
2.2 Feynman diagram of the $b \to s\gamma$ transition 8
2.3 Spectrum in q^2 of the $B^0 \to K^{*0}e^+e^-$ decay 10
2.4 Feynman diagram of the $B^0 \to K^{*0}e^+e^-$ decay 11
2.5 Angular basis definition 13

3.1 CERN accelerator complex 18
3.2 LHCb detector overview 19
3.3 VELO detector 20
3.4 RICH detectors 22
3.5 Calorimeter system and Bremsstrahlung recovery 23

4.1 Effective q^2 range definition 29

5.1 VELO photon conversion map 37
5.2 HOP mechanism 39

6.1 Mass fit to $B^0 \to K^{*0}J/\psi(\to e^+e^-)$ simulation 51
6.2 Mass fit to $\Lambda_b^0 \to pK^-J/\psi(\to e^+e^-)$ simulation 52
6.3 Mass fit to $B^0 \to K^{*0}J/\psi(\to e^+e^-)$ data 54
6.4 Mass fit to $B^0 \to K^{*0}\gamma(\to e^+e^-)$ simulation 56
6.5 Mass fit to $B^0 \to K^{*0}e^+e^-$ simulation 57
6.6 Mass fit to $B^+ \to K_1(1270)(\to K^+\pi^-X)e^+e^-$ simulation, gamma q^2-bin 59
6.7 Mass fit to $B^+ \to K_1(1270)(\to K^+\pi^-X)e^+e^-$ simulation, very-low q^2-bin 60
6.8 Mass fit to $B^0 \to K^{*0}\pi^0/\eta$ simulation, gamma q^2-bin 61
6.9 Mass fit to $B^0 \to K^{*0}\pi^0(\to \gamma e^+e^-)$ simulation 62
6.10 Mass fit to $B^0 \to K^{*0}\eta(\to \gamma e^+e^-)$ simulation 63
6.11 Mass fit to $B^0 \to K^{*0}e^+e^-$ data, gamma q^2-bin 68
6.12 Mass fit to $B^0 \to K^{*0}e^+e^-$ data, very-low q^2-bin 69

7.1 Angular acceptance for $\cos\theta_\ell$ 76
7.2 Angular acceptance for $\cos\theta_K$ 77

7.3 Angular acceptance for $\tilde{\phi}$ 78
7.4 Angular modeling of PR background 80
7.5 Angular mis-modeling of $B^0 \to K^{*0}\gamma$ 81
7.6 Angular modeling of $B^0 \to K^{*0}\gamma$ 81
7.7 Factorization check for $B^0 \to K^{*0}\gamma$ 82
7.8 Angular mis-modeling of Dalitz background 83
7.9 Angular modeling of Dalitz background 84
7.10 Angular modeling of SL/C background 85

8.1 Angular fit to reconstructed and selected $B^0 \to K^{*0}e^+e^-$ simulation 87
8.2 Angular fit to generator level $B^0 \to K^{*0}e^+e^-$ simulation 88
8.3 Distribution in q^2 of generator level $B^0 \to K^{*0}e^+e^-$ simulation . 89
8.4 Mass and angular fit to $B^0 \to K^{*0}\gamma(\to e^+e^-)$ data 91
8.5 Distribution of angular observables from pseudoexperiments . . 94

9.1 Mass and angular fit to $B^0 \to K^{*0}e^+e^-$ data 98
9.2 Constraints on photon polarization 100

B.2 List of Tables

4.1 Summary of data samples 28

5.1 Training variables of multivariate classifier 41
5.2 Summary of selection efficiencies 44
5.3 Stripping requirements 45
5.4 Selection requirements 46
5.5 Selection efficiency $B^0 \to K^{*0}e^+e^-$ 47
5.6 Selection efficiency $B^0 \to K^{*0}J/\psi\,(\to e^+e^-)$ 47
5.7 Ratio of selection efficiencies 47

6.1 Reference channel signal yields 53
6.2 Mass fit fractions, gamma q^2-bin 67
6.3 Mass fit fraction, very-low q^2-bin 67

7.1 Parameters of the $B^+ \to K_1(1270)(\to K^+\pi^-X)e^+e^-$ simulation 79

8.1 Parameter of the $B^0 \to K^{*0}e^+e^-$ simulation 89
8.2 Systematic uncertainties 95

C Bibliography

[1] R. Aaij *et al.*, "Strong constraints on the $b \to s\gamma$ photon polarisation from $B^0 \to K^{*0}e^+e^-$ decays," *JHEP*, vol. 12, p. 081, 2020.

[2] F. Desse, *Angular analysis of $B^0 \to K^{*0}e^+e^-$ decays with the LHCb detector and upgrade of the electronics of the calorimeters*. PhD thesis, 2020. Presented 22 Jul 2020.

[3] R. Aaij *et al.*, "Observation of a narrow $P_c(4312)^+$ state, and of two-peak structure of the $P_c(4450)^+$," *Phys. Rev. Lett.*, vol. 122, p. 222001, 2019.

[4] S. Chatrchyan *et al.*, "Observation of a New Boson at a Mass of 125 GeV with the CMS Experiment at the LHC," *Phys. Lett. B*, vol. 716, pp. 30–61, 2012.

[5] G. Aad *et al.*, "Observation of a new particle in the search for the Standard Model Higgs boson with the ATLAS detector at the LHC," *Phys. Lett. B*, vol. 716, pp. 1–29, 2012.

[6] W. Commons, "File:standard model of elementary particles.svg — wikimedia commons, the free media repository," 2021. [Online; accessed 22-February-2021].

[7] R. Aaij *et al.*, "Measurement of $|V_{cb}|$ with $B_s^0 \to D_s^{(*)-}\mu^+\nu$ decays," *Phys. Rev.*, vol. D100, p. 072004, 2020.

[8] Y. Fukuda *et al.*, "Evidence for oscillation of atmospheric neutrinos," *Phys. Rev. Lett.*, vol. 81, pp. 1562–1567, 1998.

[9] N. Aghanim *et al.*, "Planck 2018 results. I. Overview and the cosmological legacy of Planck," *Astron. Astrophys.*, vol. 641, p. A1, 2020.

[10] L. Canetti, M. Drewes, and M. Shaposhnikov, "Matter and Antimatter in the Universe," *New J. Phys.*, vol. 14, p. 095012, 2012.

[11] "LHC Machine," *JINST*, vol. 3, p. S08001, 2008.

[12] G. Aad *et al.*, "The ATLAS Experiment at the CERN Large Hadron Collider," *JINST*, vol. 3, p. S08003, 2008.

[13] S. Chatrchyan *et al.*, "The CMS Experiment at the CERN LHC," *JINST*, vol. 3, p. S08004, 2008.

[14] G. Aad *et al.*, "Search for new phenomena in events with two opposite-charge leptons, jets and missing transverse momentum in *pp* collisions at $\sqrt{s} = 13$ TeV with the ATLAS detector," 2 2021.

[15] A. M. Sirunyan *et al.*, "Search for supersymmetry in final states with two oppositely charged same-flavor leptons and missing transverse momentum in proton-proton collisions at $\sqrt{s} = 13$ TeV," 12 2020.

[16] J. H. Christenson, J. W. Cronin, V. L. Fitch, and R. Turlay, "Evidence for the 2π Decay of the K_2^0 Meson," *Phys. Rev. Lett.*, vol. 13, pp. 138–140, 1964.

[17] M. Kobayashi and T. Maskawa, "*CP*-violation in the renormalizable theory of weak interaction," *Prog. Theor. Phys.*, vol. 49, pp. 652–657, 1973.

[18] M. L. Perl *et al.*, "Evidence for Anomalous Lepton Production in e+ - e- Annihilation," *Phys. Rev. Lett.*, vol. 35, pp. 1489–1492, 1975.

[19] S. W. Herb *et al.*, "Observation of a Dimuon Resonance at 9.5-GeV in 400-GeV Proton-Nucleus Collisions," *Phys. Rev. Lett.*, vol. 39, pp. 252–255, 1977.

[20] D. Buttazzo, A. Greljo, G. Isidori, and D. Marzocca, "B-physics anomalies: a guide to combined explanations," *JHEP*, vol. 11, p. 044, 2017.

[21] R. Aaij *et al.*, "Search for hidden-sector bosons in $B^0 \to K^{*0}\mu^+\mu^-$ decays," *Phys. Rev. Lett.*, vol. 115, p. 161802, 2015.

[22] K. G. Wilson, "Nonlagrangian models of current algebra," *Phys. Rev.*, vol. 179, pp. 1499–1512, 1969.

[23] S. Bifani, S. Descotes-Genon, A. Romero Vidal, and M.-H. Schune, "Review of Lepton Universality tests in B decays," *J. Phys. G*, vol. 46, no. 2, p. 023001, 2019.

[24] D. Bećirević, E. Kou, A. Le Yaouanc, and A. Tayduganov, "Future prospects for the determination of the Wilson coefficient $C'_{7\gamma}$," *JHEP*, vol. 08, p. 090, 2012.

[25] L. L. Everett, G. L. Kane, S. Rigolin, L.-T. Wang, and T. T. Wang, "Alternative approach to $b \to s\gamma$ in the uMSSM," *JHEP*, vol. 01, p. 022, 2002.

[26] J. Foster, K.-i. Okumura, and L. Roszkowski, "New constraints on SUSY flavour mixing in light of recent measurements at the Tevatron," *Phys.Lett.*, vol. B641, pp. 452–460, 2006.

[27] E. Lunghi and J. Matias, "Huge right-handed current effects in $B \to K^{*0}(K\pi)\ell^+\ell^-$ in supersymmetry," *JHEP*, vol. 04, p. 058, 2007.

[28] T. Goto, Y. Okada, T. Shindou, and M. Tanaka, "Patterns of flavor signals in supersymmetric models," *Phys.Rev.*, vol. D77, p. 095010, 2008.

[29] E. Kou, C.-D. Lü, and F.-S. Yu, "Photon polarization in the $b \to s\gamma$ processes in the Left-Right Symmetric Model," *JHEP*, vol. 12, p. 102, 2013.

[30] B. Aubert *et al.*, "Measurement of the $B \to X_s\gamma$ branching fraction and photon energy spectrum using the recoil method," *Phys. Rev.*, vol. D77, p. 051103, 2008.

[31] J. Lees *et al.*, "Precision measurement of the $B \to X_s\gamma$ photon energy spectrum, branching fraction, and direct CP asymmetry $A_{CP}(B \to X_{s+d}\gamma)$," *Phys. Rev. Lett.*, vol. 109, p. 191801, 2012.

[32] J. Lees *et al.*, "Exclusive Measurements of $b \to s\gamma$ Transition Rate and Photon Energy Spectrum," *Phys. Rev.*, vol. D86, p. 052012, 2012.

[33] T. Saito *et al.*, "Measurement of the $\bar{B} \to X_s\gamma$ branching fraction with a sum of exclusive decays," *Phys. Rev.*, vol. D91, no. 5, p. 052004, 2015.

[34] A. Abdesselam *et al.*, "Measurement of the inclusive $B \to X_{s+d}\gamma$ branching fraction, photon energy spectrum and HQE parameters," in *38th International Conference on High Energy Physics*, 8 2016.

[35] Y. S. Amhis *et al.*, "Averages of b-hadron, c-hadron, and τ-lepton properties as of 2018," 9 2019.

[36] M. Misiak *et al.*, "Updated NNLO QCD predictions for the weak radiative B-meson decays," *Phys. Rev. Lett.*, vol. 114, no. 22, p. 221801, 2015.

[37] Y. Ushiroda *et al.*, "Time-dependent CP asymmetries in $B^0 \to K^0_S\pi^0\gamma$ transitions," *Phys. Rev.*, vol. D74, p. 111104, 2006.

[38] B. Aubert *et al.*, "Measurement of Time-Dependent CP Asymmetry in $B^0 \to K^0_S\pi^0\gamma$ Decays," *Phys. Rev.*, vol. D78, p. 071102, 2008.

[39] R. Aaij *et al.*, "Measurement of *CP*-violating and mixing-induced observables in $B_s^0 \to \phi\gamma$ decays," *Phys. Rev. Lett.*, vol. 123, p. 081802, 2019.

[40] M. Borsato, *Study of the $B^0 \to K^{*0}e^+e^-$ decay with the LHCb detector and development of a novel concept of PID detector: the Focusing DIRC.* PhD thesis, 2015. Presented 08 Sep 2015.

[41] Y. Grossman and D. Pirjol, "Extracting and using photon polarization information in radiative B decays," *JHEP*, vol. 06, p. 029, 2000.

[42] S. Jäger and J. M. Camalich, "On $B \to V\ell\ell$ at small dilepton invariant mass, power corrections, and new physics," *JHEP*, vol. 05, p. 043, 2013.

[43] D. M. Straub, "flavio: a Python package for flavour and precision phenomenology in the Standard Model and beyond," 10 2018.

[44] A. Paul and D. M. Straub, "Constraints on new physics from radiative B decays," *JHEP*, vol. 04, p. 027, 2017.

[45] R. Aaij *et al.*, "Angular analysis of the $B^0 \to K^*e^+e^-$ decay in the low-q^2 region," *JHEP*, vol. 04, p. 064, 2015.

[46] R. Aaij *et al.*, "Differential branching fraction and angular analysis of the decay $B^0 \to K^{*0}\mu^+\mu^-$," *JHEP*, vol. 08, p. 131, 2013.

[47] W. Altmannshofer, P. Ball, A. Bharucha, A. J. Buras, D. M. Straub, and M. Wick, "Symmetries and Asymmetries of $B \to K^*\mu^+\mu^-$ Decays in the Standard Model and Beyond," *JHEP*, vol. 01, p. 019, 2009.

[48] J. Lefrançois and M. H. Schune, "Measuring the photon polarization in $b \to s\gamma$ using the $B \to K^*e^+e^-$ decay channel," Tech. Rep. LHCb-PUB-2009-008. CERN-LHCb-PUB-2009-008. LHCb-INT-2009-007, CERN, Geneva, Jun 2009.

[49] F. Krüger and J. Matias, "Probing new physics via the transverse amplitudes of $B^0 \to K^{*0}(\to K^-\pi^+)l^+l^-$ at large recoil," *Phys. Rev.*, vol. D71, p. 094009, 2005.

[50] D. Bećirević and E. Schneider, "On transverse asymmetries in $B \to K^*\ell^+\ell^-$," *Nucl.Phys.*, vol. B854, pp. 321–339, 2012.

[51] C. Bobeth, G. Hiller, and G. Piranishvili, "CP asymmetries in $\bar{B} \to \bar{K}^*(\to \bar{K}\pi)\bar{\ell}\ell$ and untagged $\bar{B}_s$, $B_s \to \phi(\to K^+K^-)\bar{\ell}\ell$ decays at NLO," *JHEP*, vol. 07, p. 106, 2008.

[52] K. Aamodt *et al.*, "The ALICE experiment at the CERN LHC," *JINST*, vol. 3, p. S08002, 2008.

[53] A. A. Alves Jr. *et al.*, "The LHCb detector at the LHC," *JINST*, vol. 3, no. LHCb-DP-2008-001, p. S08005, 2008.

[54] R. Aaij *et al.*, "LHCb detector performance," *Int. J. Mod. Phys.*, vol. A30, p. 1530022, 2015.

[55] R. Aaij *et al.*, "Performance of the LHCb Vertex Locator," *JINST*, vol. 9, p. P09007, 2014.

[56] P. d'Argent *et al.*, "Improved performance of the LHCb Outer Tracker in LHC Run 2," *JINST*, vol. 12, p. P11016, 2017.

[57] M. Adinolfi *et al.*, "Performance of the LHCb RICH detector at the LHC," *Eur. Phys. J.*, vol. C73, p. 2431, 2013.

[58] A. A. Alves Jr. *et al.*, "Performance of the LHCb muon system," *JINST*, vol. 8, p. P02022, 2013.

[59] R. Aaij *et al.*, "Test of lepton universality with $B^0 \to K^{*0}\ell^+\ell^-$ decays," *JHEP*, vol. 08, p. 055, 2017.

[60] R. Aaij *et al.*, "The LHCb trigger and its performance in 2011," *JINST*, vol. 8, p. P04022, 2013.

[61] T. Sjöstrand, S. Mrenna, and P. Skands, "PYTHIA 6.4 physics and manual," *JHEP*, vol. 05, p. 026, 2006.

[62] T. Sjöstrand, S. Mrenna, and P. Skands, "A brief introduction to PYTHIA 8.1," *Comput. Phys. Commun.*, vol. 178, pp. 852–867, 2008.

[63] I. Belyaev *et al.*, "Handling of the generation of primary events in Gauss, the LHCb simulation framework," *J. Phys. Conf. Ser.*, vol. 331, p. 032047, 2011.

[64] D. J. Lange, "The EvtGen particle decay simulation package," *Nucl. Instrum. Meth.*, vol. A462, pp. 152–155, 2001.

[65] P. Golonka and Z. Was, "PHOTOS Monte Carlo: A precision tool for QED corrections in Z and W decays," *Eur. Phys. J.*, vol. C45, pp. 97–107, 2006.

[66] J. Allison, K. Amako, J. Apostolakis, H. Araujo, P. Dubois, *et al.*, "Geant4 developments and applications," *IEEE Trans.Nucl.Sci.*, vol. 53, p. 270, 2006.

[67] S. Agostinelli *et al.*, "Geant4: A simulation toolkit," *Nucl. Instrum. Meth.*, vol. A506, p. 250, 2003.

[68] M. Clemencic *et al.*, "The LHCb simulation application, Gauss: Design, evolution and experience," *J. Phys. Conf. Ser.*, vol. 331, p. 032023, 2011.

[69] P. A. Zyla *et al.*, "Review of particle physics," *Prog. Theor. Exp. Phys.*, vol. 2020, no. 8, p. 083C01, 2020.

[70] L. Lista, *Statistical Methods for Data Analysis in Particle Physics*. No. ARRAY(0x55b0c77f7ab0) in Lecture notes in physics, Cham: Springer, 2nd ed. 2017 ed., 2017.

[71] W. Verkerke and D. Kirkby, "The RooFit toolkit for data modeling," *arXiv e-prints*, p. physics/0306116, June 2003.

[72] R. Brun and F. Rademakers, "ROOT: An object oriented data analysis framework," *Nucl. Instrum. Meth. A*, vol. 389, pp. 81–86, 1997.

[73] I. Antcheva *et al.*, "ROOT: A C++ framework for petabyte data storage, statistical analysis and visualization," *Comput. Phys. Commun.*, vol. 182, pp. 1384–1385, 2011.

[74] D. Derkach, M. Hushchyn, T. Likhomanenko, A. Rogozhnikov, N. Kazeev, V. Chekalina, R. Neychev, S. Kirillov, and F. Ratnikov, "Machine-Learning-based global particle-identification algorithms at the LHCb experiment," *J. Phys. Conf. Ser.*, vol. 1085, no. 4, p. 042038, 2018.

[75] M. De Cian, S. Farry, P. Seyfert, and S. Stahl, "Fast neural-net based fake track rejection in the LHCb reconstruction," Tech. Rep. LHCb-PUB-2017-011. CERN-LHCb-PUB-2017-011, CERN, Geneva, Mar 2017.

[76] L. Anderlini, A. Contu, C. R. Jones, S. S. Malde, D. Muller, S. Ogilvy, J. M. Otalora Goicochea, A. Pearce, I. Polyakov, W. Qian, B. Sciascia, R. Vazquez Gomez, and Y. Zhang, "The PIDCalib package," 2016.

[77] M. Alexander *et al.*, "Mapping the material in the LHCb vertex locator using secondary hadronic interactions," *JINST*, vol. 13, p. P06008, 2018.

[78] R. H. Dalitz, "On an alternative decay process for the neutral pi-meson, Letters to the Editor," *Proc. Phys. Soc. A*, vol. 64, pp. 667–669, 1951.

[79] M.-H. Schune, F. Polci, and M. Borsato, "HOP an additional tool for decays involving electrons," Tech. Rep. LHCb-INT-2015-037. CERN-LHCb-INT-2015-037, CERN, Geneva, Nov 2015.

[80] F. Pedregosa *et al.*, "Scikit-learn: Machine learning in Python," *J. Machine Learning Res.*, vol. 12, p. 2825, 2011. and online at http://scikit-learn.org/stable/.

[81] K. S. Cranmer, "Kernel estimation in high-energy physics," *Comput.Phys.Commun.*, vol. 136, pp. 198–207, 2001.

[82] R. Aaij *et al.*, "Observation of $J/\psi p$ resonances consistent with pentaquark states in $\Lambda_b^0 \to J/\psi p K^-$ decays," *Phys. Rev. Lett.*, vol. 115, p. 072001, 2015.

[83] R. Aaij *et al.*, "Measurement of b hadron production fractions in 7 TeVpp collisions," *Phys. Rev.*, vol. D85, p. 032008, 2012.

[84] R. Aaij *et al.*, "Measurement of b-hadron fractions in 13 TeV pp collisions," *Phys. Rev.*, vol. D100, p. 031102(R), 2019.

[85] B. Efron, "Bootstrap methods: Another look at the jackknife," *Ann. Statist.*, vol. 7, pp. 1–26, 01 1979.

[86] S. Cunliffe, M. Patel, K. Petridis, and A. Shires, "Measurement of the differential branching fraction of $B^0 \to K^*(892)^0 \mu^+ \mu^-$ and S-wave fraction of $B^0 \to K^+ \pi^- \mu^+ \mu^-$ decays using 3fb^{-1} of integrated luminosity," Jun 2016.

[87] R. Aaij *et al.*, "Measurement of *CP*-averaged observables in the $B^0 \to K^{*0} \mu^+ \mu^-$ decay," *Phys. Rev. Lett.*, vol. 125, p. 011802, 2020.

[88] R. Aaij *et al.*, "Angular analysis of the $B^+ \to K^{*+} \mu^+ \mu^-$ decay," 2020.

Acknowledgments

There are a lot of people that supported me during my year of working on this master thesis in a variety of ways. And I would like to thank all of them, because without their help I probably wouldn't have been able to finish my work.
I want to thank Fabrice Desse, Dr. Martino Borsato and Prof. Marie-Helene Schune for the possibility to work with you on this fascinating angular analysis. Thank you Fabrice for always be willing to help me with my various questions about the analysis and their software implementations. I really enjoyed the time when I could visit you and Marie-Helene in Orsay all the way at the beginning of my thesis's work.
Thank you Martino for supervising my work on the analysis and always helping me with my questions. I appreciate that I could always talk to you about the analysis but also physics in general and anything else.
I would like to express my gratitude to Prof. Stephanie Hansmann-Menzemer for giving me the opportunity to work on this exciting topic within your group and for supervising my work on the thesis.
I also want to thank Prof. Klaus Reygers for agreeing to be my second referee, as you already did for my bachelor thesis.
Furthermore I want to thank everyone in the LHCb group of Heidelberg. Whenever we had the opportunity to meet and talk, I felt welcome and the discussions were very interesting. Sadly, a lot of these interactions were cut short during the last year.
Then, last but not least, I want to thank my family and friends. Thank you for supporting me during this time and being there for me. I really appreciate this and I am very grateful for that.

Erklärung:

Ich versichere, dass ich diese Arbeit selbstständig verfasst habe und keine anderen als die angegebenen Quellen und Hilfsmittel benutzt habe.

Heidelberg, den (Datum) .....